Alma Mater Studiorum · Università di Bologna

Scuola di Scienze
Corso di Laurea Magistrale in Fisica

Ab-initio determination of X-ray absorption near edge structure (XANES) spectra in an Ultrasoft and Norm Conserving pseudopotentials scheme

Relatore:
Prof. Federico BOSCHERINI

Correlatore:
Dott. Cristian Degli Esposti Boschi

Presentata da:
Emiliano Burresi

Sessione II
Anno Accademico 2012/2013

Ringraziamenti

Desidero ringraziare il mio correlatore di tesi Dott. Cristian Degli Esposti Boschi per la dedizione e l' interesse mostrati nell'impostare e nel seguire questo progetto di tesi, oltre che nella stesura del manoscritto dove sono stati diversi i suggerimenti che ho seguito e che hanno reso il lavoro finale più efficace e completo.
Desidero ringraziare inoltre il mio relatore di tesi Prof. Federico Boscherini per avermi dato la possibilità di approfondire una tematica estremamente interessante quale la fisica dei raggi X e i fenomeni legati all'interazione della materia con la radiazione.
Sono debitore inoltre verso il consiglio di corso di Laurea per avermi dato la possibilità di accedere alla laurea magistrale e in particolare alla Prof.ssa Elisa Ercolessi per avermi aiutato nel compimento di questo percorso formativo.
Un ultimo ringraziamento allo staff del centro di calcolo CINECA per il supporto e l'aiuto mostrato durante il periodo in cui siamo stati vincitori del progetto AbIXS che ci ha dato la possibilità di accedere alle infrastrutture di calcolo ad alte prestazioni presso il consorzio CINECA.

Abstract

X-ray absorption spectroscopy (XAS) is a powerful means of investigation of structural and electronic properties in condensed -matter physics. Analysis of the near edge part of the XAS spectrum, the so – called X-ray Absorption Near Edge Structure (XANES), can typically provide the following information on the photoexcited atom:

- Oxidation state and coordination environment.
- Speciation of transition metal compounds.
- Conduction band DOS projected on the excited atomic species (PDOS).

Analysis of XANES spectra is greatly aided by simulations; in the most common scheme the multiple scattering framework is used with the muffin tin approximation for the scattering potential and the spectral simulation is based on a hypothetical, reference structure. This approach has the advantage of requiring relatively little computing power but in many cases the assumed structure is quite different from the actual system measured and the muffin tin approximation is not adequate for low symmetry structures or highly directional bonds. It is therefore very interesting and justified to develop alternative methods. In one approach, the spectral simulation is based on atomic coordinates obtained from a DFT (Density Functional Theory) optimized structure.

In another approach, which is the object of this thesis, the XANES spectrum is calculated directly based on an ab – initio DFT calculation of the atomic and electronic structure. This method takes full advantage of the real many-electron final wavefunction that can be computed with DFT algorithms that include a core-hole in the absorbing atom to compute the final cross section. To calculate the many-electron final wavefunction the Projector Augmented Wave method (PAW) is used. In this scheme, the absorption cross section is written in function of several contributions as the many-electrons function of the finale state; it is calculated starting from pseudo-wavefunction and performing a reconstruction of the real-wavefunction by using a transform operator which contains some parameters, called partial waves and projector waves.

The aim of my thesis is to apply and test the PAW methodology to the calculation of the XANES cross section. I have focused on iron and silicon structures and on some biological molecules target (myoglobin and cytochrome c). The main arguments showed in this thesis are divided in four chapters :

1. Overview of the XANES spectroscopy.
2. Introduction to the Projector Augmented Wave (PAW) formalism.
3. Plane wave pseudopotentials approach to resolve Kohn-Sham equations in DFT framework.
4. Results and discussions about ab-initio determination of the XANES cross section for iron,silicon, myoglobin and cytochrome c.

The topic of this thesis has been awarded of 500000 core processor hours on the CINECA HCP resources, on the basis of a peer-review procedure. In our case these core processor hours was allocated on an IBM BG/Q named FERMI (Project IsC09/AbIXS).

Finally other inorganic and biological systems could be taken into account for future applications of this methodology, which could become an important improvement with respect to the multiscattering approach.

Contents

Chapter 1

The X-ray absorption spectroscopy

1.1 Photoelectric absorption and X-radiation

It is indicated as X-radiation (X-rays) the region of electromagnetic spectrum corresponding to wavelenght raging 1-0.01 nm nearby gamma ray from side of shorter wavelenght, and vacuum ultraviolet region from side of longer wavelenght. The X-rays with short wavelenght (around 0.01-0.1 nm) are called hard X-rays and the X-rays with long wavelenght (up to 1 nm) are called soft X-rays.
These values are comparable with interatomic distances in condensated matter, so as it is possible to use ondulatory properties of X-rays to investigate the crystallographic structure of the matter by means of diffraction analysis.
The interaction between electromagnetic radiation and matter can produce two physical effects, scattering or absorption. In the first case, the incident X-ray photon is diffused by atoms and, after collision, its energy is conserved (Thomson's scattering) or not (Compton's scattering) with respect to the energy of the incident beam. In the second event, the X-ray photon is absorbed by matter and an electron could be expelled by means of photoelectric effect. Therefore an electronic reorganization of the absorbing atom occurs and a *photoelectron* can be produced.
Currently, elastic scattering is used as investigation method to obtain informations on the crystalline structure of the matter, if the spacing is in solid phase and in crystalline form. This method, called X-ray Diffraction, is not taken in account in this thesis and is reported just to complete the overview about X-ray investigation methods. In this chapter we will describe the behaviour of the X-ray radiation in the photoelectric absorption.
The absorption and emission of the electromagnetic radiation by matter occurs by means of well defined quantum energy (the photons) $E = h\nu$ and involves the atomic energy level of the absorbing atom, in accordance with Bohr law [1]:

$$\Delta E = h\nu \tag{1.1}$$

where h is the Planck constant and ν is the photon frequencies.
The energy corrisponding to the soft X-Ray and hard X-Ray is around 1keV and 10 keV respectively. In this range, the electrons interacting with X-ray photons

occupy the inner shell of the atoms, called shell K or shell L. Once the photon is absorbed in K shell, an electron can be expelled from the atom (with production of *photoelectron*) and the formation of a hole occurs. Subsequently, the hole can be filled by means of two distinct processes: if an electron from upper shell drops in K-shell and the atom relaxes to its ground state, fluorescence effect happens. On the contrary, the atom relaxes emitting electrons from upper shell, called Auger electrons. In the first case, the energy of X-ray photon corresponds to the energy difference between two electronic level which are involed in the relaxing process; K_α emission lines results when an electron transitions to the innermost "K" shell from shell L, whereas K_β emission lines is resulting from the transiton $M \rightarrow K$.

In order to understand the photoelectric asborption, the absorption cross section

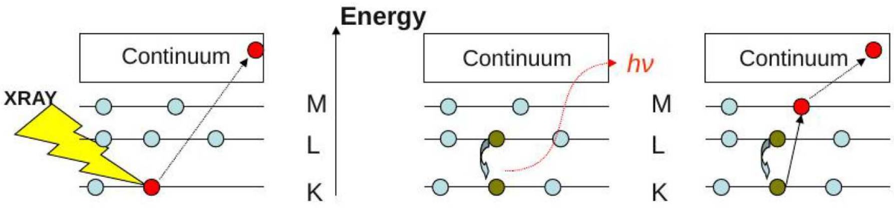

Figure 1.1: Mechanism of production of a *photoelectron* by means of X-ray photon absorption and subsequent relaxing through fluorescence and Auger effects

have to be introduced.

Let us to consider an electromagnetic wave consisting of N photons with energy $h\nu$, wave vector $\overrightarrow{k}$ and intensity

$$I_0 = Nh\nu \tag{1.2}$$

The intensity I follows an exponential decay law

$$\frac{I}{I_0} = e^{-\mu d} \tag{1.3}$$

where μ is the absorption coefficient and d is thickness of the sample. The energy flux through the sample area A per second is:

$$\Phi_0 = \frac{N}{A} h\nu = \frac{I_0}{A} \tag{1.4}$$

The density of the atoms in spacing crossed by flow Φ_0 is defined as n_b. Then, the number of scattered X-ray photons per second is

$$I_{sc} = \Phi_0 N_b \sigma \tag{1.5}$$

with $N_b = n_b A d$ and σ, called geometric cross section.

Let us to define $W_{4\pi}$ the number of absorbed photons per second in 4π stereoradiant. Then the previous equation can be rewritten as

$$W_{4\pi} = \Phi_0 N_b \sigma_a \tag{1.6}$$

where σ_a is called absorption cross section. In last equation the flow of the incident photons Φ_0 is included because the incident beam is larger than the

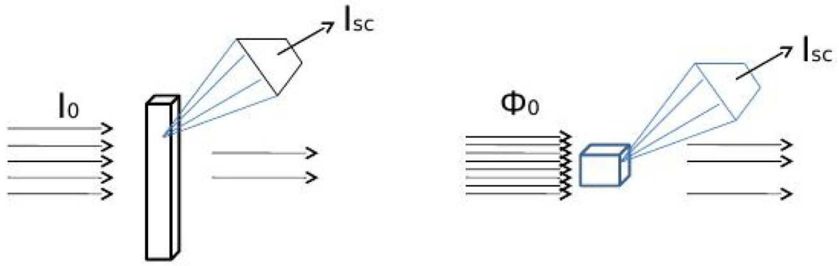

Figure 1.2: Incident radiation beam on a sample either with a larger (on the left) and smaller (on the right) cross section area

sample; on the contrary, we could consider the incident beam smaller than sample by replacing the flow Φ_0 by intensity I_0. The physical meaning of the cross section is the area corrisponding to each diffusion center (for example an absorbing atom). It is defined as

$$\sigma_a = \frac{W_{4\pi}}{\Phi_0 N_b} \tag{1.7}$$

Ragarding the diffusion process, we consider the number of scattered X-ray per second into a detector subtended the solid angle $\Delta\Omega$ by introducing into equation (1.6) the differential cross section $(\frac{d\sigma}{d\Omega})$

$$I_{sc} = I_0 N_b \Delta\Omega (\frac{d\sigma}{d\Omega}) \tag{1.8}$$

Usually, the differential cross section is introduced to study scattering process where X-ray photons are scattered in a region into the solid angle $\Delta\Omega$, subtended by detector of area $\Delta\Omega = \frac{A_D}{r^2}$; from mathematical point of view, it means to perform an integration over the $\boldsymbol{k}_f$ values into the solid angle $\Delta\Omega$. For absorption process they any direction into 4π radians is possible.
The absorption coefficient μ is strictly connected with absorption cross section σ_a, by equation:

$$\mu = \rho_a \sigma_a = (\frac{\rho_m N_A}{A})\sigma_a \tag{1.9}$$

by means of which the absorption cross section becomes experimentally measurable by means of absorption X-ray spectroscopy experiment. In equation (1.9) N_a corrisponds to the Avogadro number, ρ_a to atomic density, ρ_m is the mass density and A is atomic mass number.
In general, the absorption cross section σ_a is dependent on atomic number Z and on photon energy E. This dependence becomes evident when it is plotted in function of the energy of incident photon.
This function suffers a discontinuity corresponding to well-defined energies of incident photon, which are typical for each chemical element. The discontinuities determine the absorption threshold and in qualitative terms, they can be explained easily. Let us to consider an electron into shell K of iron atom,with

binding energy value of 7.112 keV. In presence of incident photons with energy greater than 7.112 keV, the electron into K-shell can be expelled by photon. In case of incident photon with energy smaller than 7.112 eV, the electron can not be expelled from K-shell, but a photoelectron can be produced from shell L_I,L_{II} ed L_{III}. The corresponding energy value from shell K is called K-edge. Therefore the value reported above of 7.112 keV corresponds to the Fe K-edge. For silicon the K-edge value is 1.839 keV.
In addition we want to show that the K-edge energy has a well-defined value for each atom, while the L-edge has a more complex structure, corresponding to the atomic *fine* structure. Rougly speaking, in figure (1.3) we show the absorption process by X-ray photon which involves the atomic energy levels of the absorbing atom;the cross section is reported in function of the energy of incident photon. Figure indicates how the cross section relative to the excitation process from L shell is characterized by *fine* structure due to the 2s and 2p orbitals (belonging to L-shell) which are splitted towards different energy values. The 2s orbital is found at low energy, whereas the p orbitals are splitted in $p_{1/2}$ and $p_{3/2}$ due to the spin-orbit coupling. This splitting of $2s$ e $2p$ obitals generates the *fine* structure of the L-edge. Regarding the K-edge no fine structure is detected because the photoelectric process involves just the $1s$ orbital.

In order to describe the radiation-matter interaction a complete quantum-mechanical approach should be used, where both the radiation and the atom are treated as quantum object. Analogue results can be achieved using a semiclassical theory, by means of which the radiation is treated as classical electromagnetic wave and the matter is treated quantum-mechanically.

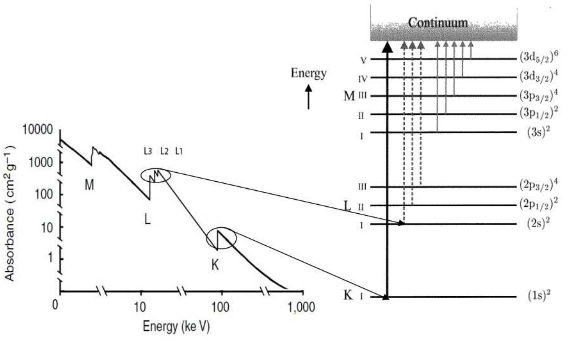

Figure 1.3: In figure the meaning of *fine* structure in absorption cross section is showed[2]

In semiclassical theory the radiation-matter interaction is described through a perturbative theory time-dependent, where the radiation it is considered as a periodic perturbation acting on absorbing atom. In this way the Hamiltonian $\widehat{H}$ is a sum of two terms: $\widehat{H}_I = \widehat{V}$ which is a small perturbation time-dependent, whereas with H_0 it is indicated the unperturbed hamiltonian. Finally we found that $\widehat{H} = \widehat{H}_I + \widehat{H}_0$.[3]
The hamiltonian H_I is cause of transition between two atomic states; the initial state corresponds to the atomic state with energy E_i of the unperturbed atom, while the atomic final state corresponds to the state whose energy value is found in a band around the value $E_i + h\nu$.
Let us to indicate the intial state, by using Dirac notation, as $|i\rangle$ and the final one with $|f\rangle$. The number of transitions per second between $|i\rangle$ and $|f\rangle$ is calculated by Fermi golden rule at first perturbation order

$$W = \frac{2\pi}{\hbar}|M_{if}|^2\rho(E_f) \tag{1.10}$$

where the matrix transition element is $M_{if} = \langle i|H_I|f\rangle$ and $\rho(E_f)$ is the density of final state of the photoelectron. The pertubation term H_I will be explained in section 4 in detail.
In order to calculate the absorption cross section, it is necessary to perform an integration over the entire solid angle 4π, considering that the absorption process is no longer elastic and the electron is expelled from the orbital with binding energy E_b. Obviously the difference between photon energy $h\nu$ and the orbital binding energy E_b is equal to the photoelectron energy. The number of the events $W_{4\pi}$, i.e. the number of photons absorbed per second is

$$W_{4\pi} = \int \frac{2\pi}{\hbar}|M_{if}|^2 E_f^2 \delta(E_{pe} - (E - E_b))\rho(E_{pe})dE_{pe} \tag{1.11}$$

The matrix element $|M_{if}|$ is calculated in dipole approximation as $M_{if} = \langle f \,|\, \widehat{\boldsymbol{\epsilon}} \cdot \overrightarrow{\boldsymbol{r}} \,|\, i \rangle$ and transition in which the angular momentum change as $\Delta l = \pm 1$

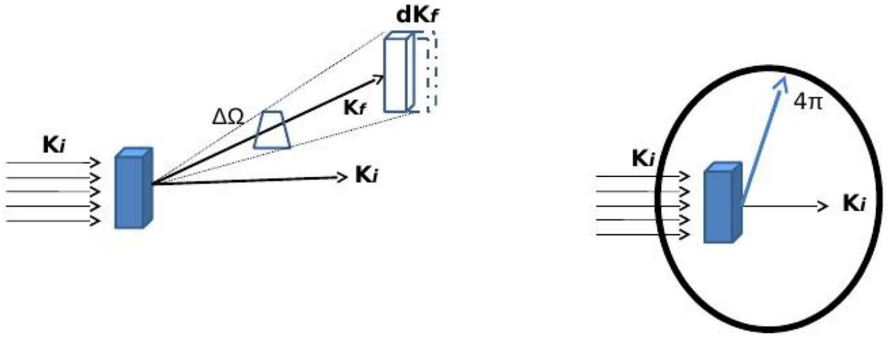

Figure 1.4: To calculate the differential cross section an integrazion over k_f value behind the solid angle subtended by detector is needed (on the right). Regarding the absorption cross section it is necessary perform an integration over all directions of the photoelectron

occurs.The absorption cross section is given by equation

$$\sigma_a = \frac{W_{4\pi}}{\Phi_0} \tag{1.12}$$

Next sections the teoretical and experimental tools to perform an *XAS (X-Ray Absorption Spectroscopy)* experiment will be illustrated. In particular, it will be illustrated the *XANES (X-Ray Absorption Near-Edge Structure)* technique which has been the object of the study in this thesis.

1.2 XANES e X-rays source

In this section typical experimental apparatus to perform X-ray absorption experiment are described.In particular the source of X-rays will be illustrated and the synchrotron radiation will be explained in detail[2].
The X-ray absorption spectra can be recorder in a trasmission geometry by using an experimental apparatus whose schematic layout is reported in figure below (1.5).
The trasmission factor defined as $T = \frac{I}{I_0}$ is related to absorption coefficient in function of the energy of incident photons ε, following the equation $T = \exp(-\mu(\varepsilon))d$ where d is the thickness of the sample.
It is also possible to measure the XAS signal by measuring the fluorescence yield, where the dector is placed at 90° to the incident beam in a horizontal plane, so as the unwanted contribution from elastic or anelastic scattering processes is minimized or eliminated.

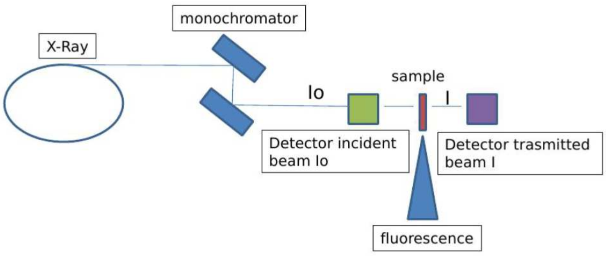

Figure 1.5: In figure it is reported the scheme of experimental apparatus to acquire *XAS* signal in trasmission and fluorescence geometry

Generally,in *XAS* experiment a source X-rays (X-ray tube,rotating anode, synchrotron radiation ...), optical components like monochromator and focalizing devices, detector to record the incident and transmitted beam radiation will be employed.
The employment of synchrotron radiation requires the usage of a coherent source X-ray with large continue energy band and higher brillance. All these requirements are taken in account in synchrotron radiation. The figure-of-merit for the source is defined as

$$Brillance = \frac{photons/sec}{(mmrad)^2 mm^2 0.1\% bandwidth} \tag{1.13}$$

where the intensity (number of photons per second) and the collimation of the beam are introduced. Usually the collimation of the beam is given in milli-radian, either for the horizontal and for vertical direction. It may be of importance to know the size of the source and in equation (1.42) it is reported in mm^2. Moreover, in order to define the photon energy range to compare different X-ray source, it has been fixed a relative bandwidth, choosen to be 0.1%. In this way, the brillance is a quantity which allows one to compare the quality of X-ray beam from different sources. The maximum brillance from third generation is about $10^{20} photon/mrad^2/mm^2$, around 10 orders of magnitude higher than that from a rotating anode.

The technological limits regarding the X-ray production from standard fluorescence tubes are both low radiation intensity(depending by cooling efficiency) and discrete nature of the emitting radiation; in a X-ray experiment like XANES or EXAFS it is necessary using a continue energy spectrum. The rotating anode tube improves the intensity beam because has a higher cooling efficiency; however it is not employed in XAS spectroscopy for his discrete fluorescence lines of the radiation. Indeed the spectrum from X-ray tube has also a continue bremsstralung component due to the deceleration of the electrons forced by metallic anode. The maximum intensity value of this radiation depends by the applied voltage between anode and cathode; however its intensity is much lower than discrete fluorescence lines K_α e K_β.

The synchrotron radiation is produced from charged particles travelling at relativistic speed, forced to travel along curved paths by means of magnetic field. The emitting radiation from charged particles is confined to a narrow cone with an opening angle of $\gamma^{-1} = \frac{mc^2}{\varepsilon_e}$ with $\gamma = \frac{\varepsilon_e}{mc^2}$ is the electron relativistic energy in mc^2 unit (figure 1.6).

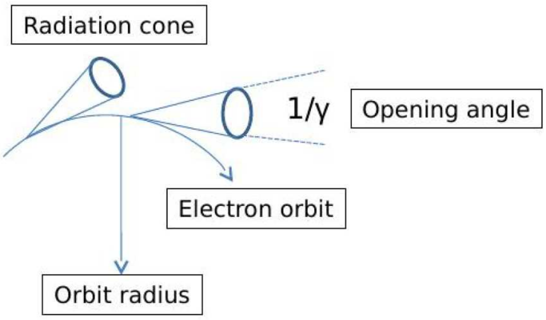

Figure 1.6: In a accumulation ring, the electrons are forced to go through circular paths due to the application of constant magnetic field, emitting a beam radiation with opening angle $1/\gamma$ around 0.1-1 mrad, extremely collimated

The frequency of the electrons in a storage ring is 10^6 sec^{-1}. In order to produce X-ray, higher frequencies are needed, around 10^{18}. This value is obtained if the electrons are forced to achieve relativistic condition. Typical values of the electron energies in a storage ring are around 5 GeV with $\gamma = 10^4$. The opening angle of the radiation cone is about 0.1-1 mmrad.

The orbital radius of the circulating electron beam are calculated from Lorentz force $L_l = qcB$ where q is the charge of the particle, B is the magnetic field and

c is the light speed. Since it is a circular motion, the Lorentz force is equal to $F_l = ma_c$ where a_c is the centripetal force. The linear momentum of relativistic electron is $p = \gamma mc$, then the radius is given by equation

$$\gamma mc = RqB \tag{1.14}$$

where q is the charge of the electron and R is the radius of the circular orbit. Typical values of radius in storage ring are 1-40 m (The radius of synchrotron in Grenoble is around 40 m) corresponding the the 0.02-2 GeV energy values. Magnetic field forcing the electron in a circular motion are around 0.8 T.

The electrons circulating in a storage ring with angular frequency ω_0 should produce photon with frequency $\frac{c}{2\pi R}$ (c light speed and R radius of the ring), corresponding to the values $10^6 - 10^7$ Hz typical values of the microwave range. In order to obtain higher frequency, the electrons are accelerated into the radiofrequency cavity. Then they move into devices which force them to have a circular trajectory. These devices are a real radiation source. The bending magnets force the electrons to travel along a circular trajectory producing photons due to costant magnetic field application.

Let us imagine some devices [4] with lenght L and the spatial distance between devices and detector is L'.

Let us to set the instant in which the electron pass through the bending magnet as $T = 0$; the first photon emitted reachs the detector at the time $T_i = \frac{L}{c} + \frac{L'}{c}$ and the last one reachs the detector at the time $T_f = \frac{L'}{c} + \frac{L}{v}$, where v is the electron speed and c is the light speed. The difference between $\Delta T = T_f - T_i$, corresponds to the photon pulse:

$$\Delta T = \frac{L}{v}\Big[1 - \frac{v}{c}\Big] \tag{1.15}$$

The photon frequency is calculated as

$$\nu = \frac{v\gamma^2}{L}\Big[1 + \frac{v}{c}\Big] \tag{1.16}$$

By fixing c $\approx$ v, $\gamma = 10^4$ c$\approx$ 10^8 m/s and L=0.1 m, we obtained $\nu \approx 10^{17} Hz$ which corresponds to the frequency of the X-ray photons. The pulse duration is characterized by short time (for example with gaussian profile) and the Fourier transofrmation produces a broad frequency and energy spectrum, as necessary in a X-ray absorption experiment *XAS*.

We have already said as the synchrotron radiation has a relativistic nature. We show briefly this behaviour by considering the electron in a storage ring along a circular path. Its velocity changes in direction everywhere, generating a centripetal acceleration. Let us define $\Delta t'$ the time that the electron spends to travel between two points A and B with velocity v, i.e. the time for the electron to travel from one bend to the next. The observer experiences a time interval of Δt between wavefronts. Due to the relativistic Doppler effect, the time interval measured by observer (in laboratory reference frame) between two wavefront emitted from A and B is

$$\Delta t = (c - v cos\alpha)\frac{\Delta t'}{c} \tag{1.17}$$

where α is the angle between electron velocity and the direction of the observer. The radiation intensity is as higher as the Doppler effect is maximal. The physical condition need to achieve the maximal contribution of Doppler effect are satisfied for smallest α angle and the direction of the electron velocity is nearly coincident with oberver direction.

We can also estimate the radiated power along the electron path as

$$P[kW] = 1.266\varepsilon^2[GeV]B^2[T]L[m]I[A] \tag{1.18}$$

where ε is the electron energy; its derivation in this section is beyond of our scope.

Other radiation sources used in a synchrotron ring are wigglers and undulators where the variable magnetic fields force the electrons to move along an ondulatory path. The wigglers are built as a series of circular arcs, turning successively to the left and to the right, forcing the electrons to oscillate both in orizontal and vertical plane. In wigglers devices the observed intensity rises due to the sum of incoerent waves, outcoming from each insertion. The increasing of intensity is around 2N value where N is the number of periods. In wigglers no constant magnetic field is used $\left\langle B_0^2 \right\rangle = \frac{B_0^2}{2}$, where B_0 is the maximum value of the field which is introduced into the wiggler radiation power equation.

In ondulators the radiation is obtained by two distinct waves which are generated by electrons in phase. An important physical quantity is the K factor which discern the radiation outcoming from wigglers and ondulators

$$K = \frac{\lambda q B_0}{2\pi mc} \tag{1.19}$$

where $K \approx$ is 20 cmT for wigglers and around 1 for the ondulators. For wiggler the horizontal and vertical opening angle of the radiation cone is K/γ and $1/\gamma$ respectively; for ondulators is $\frac{1}{\gamma}$ in both cases.

Finally coherence rate of the synchrotron radiation is obtained producing interference effects through waves generated by single electrons. In this framework, it is possible to produce radiation with both transversal and longitudinal coherence, which define the range where constructive interference occurs. By using higher values out of range, shift between radiation components occurs, producing an incoherent beam radiation with bandwidth $\Delta\lambda \setminus \lambda \neq 0$.

1.3 XANES spectroscopy

In previous sections absorption cross section was introduced and the microscopic mechanism produced by photon absorption have been illustrated. During this process, the photoelectron suffers both the electron charge distribution and the chemical enviroment. This is one of the reasons of the success of absorption X-ray spectroscopies. The matter wave associates to the photoelectron is scattered by atoms near to the absorbing atoms; then the cross section is dependent on position of the nearest neighbour atoms. The photoelectron could fill either unoccupied higher energy states or unbound states.

Usually XANES spectroscopy is defined up to 40-50 eV above the edge; in this region the kinetic energy of the photoelectron is not very high and multiple scattering events principally occurs. On the contrary in EXAFS region the

photoelectron suffers a weak scattering.
In figure (1.7) typical XAS spectra is reported;the main area of interest,pre-edge, XANES and EXAFS are indicated. Pre-edge region corresponds to the photolelectron transition probabily due to the quadrupolar contributes of the scattering matrix. Changing of the angular quantum number of $\Delta l = \pm 2$ is allowed, producing low intensity signal. Another reason is the transition to the discrete levels of the absorbing atom.
In the XANES region photoelectron multiple scattering by nearest neighbour atoms occurs, producing the oscillating part of the spectrum. The wave associated to the photoelectron propagates from source atom (the absorbing atom) as a spherical wave. The oscillations extends for several hundred eV above the edge, due to the back scattering of the outgoing spherical wave by neighbouring atom. The EXAFS oscillations [2] are produced by interference between the outgoing and back scattering waves. In EXAFS experiment the intial state Ψ_i is the wave function which describes the innermost electrons in the orbital 1s or 2s of the absorbing atom: the final state Ψ_f is that of the photoelectron which interacts with nearest neighbour ions. This interaction involves a changing of the photoelectron wave function, defined by Ψ_{bs}; the EXAFS oscillations are dependent from this modification. In fact let us to account the wave associate to the outgoing photoelectron $\frac{e^{iqr}}{r}$, where r is calculated from the centre of the absorbing atom and q is the wave vector of the photoelectron; by interaction between photoelectron and one atom placed at the distance R from absorbing atom,new spherical wave $\frac{e^{iqR}}{R}$ is produced. The amplitude of the wave produced by interference between outgoing wave from absorbing atom and backscattered wave will be proportional to the $\frac{e^{i2qR}}{R^2}$, then the quantity Ψ_{bs} at first approximation, will be proportional to $\frac{e^{i2qR}}{R^2}$. In order to complete the analytical expression of the EXAFS signal, we add the Deby-Waller factor, where the vibrations of the nearest neighbour are taken in account, a phenomenological mean-free pathlength and the scattering lenght $t(q)$ to which the amplitude of the backscattered wave is dependent. The EXAFS signal will be described by the following equation:

$$\Psi_{bs} \propto \frac{t(q) sen(2qR + \delta(q))}{qR^2} e^{-2(q\sigma)^2} e^{-2R/\Lambda}$$

By considering one shell of N nearest neighbour atoms to the distance R_j, we obtain

$$\chi(q) \propto \sum_j \frac{t_j(q) sen(2qR_j + \delta(q))}{qR_j^2} e^{-2(q\sigma_j)^2} e^{-2R_j/\Lambda}$$

with $\chi(q)$ EXAFS signal defined as

$$\chi(q) = \frac{\mu_\varepsilon - \mu_0}{\mu_0} \tag{1.20}$$

where μ_ε is the absorption coefficient of the atom of the sample and μ_0 is that isolated atom.

Usually, the scattering process of the photoelectron is described by spherical potential approximation, known as *muffin-tin approximation*[4]. In this scheme, the photoelectron suffers a potential V, sum of single contributions; each single

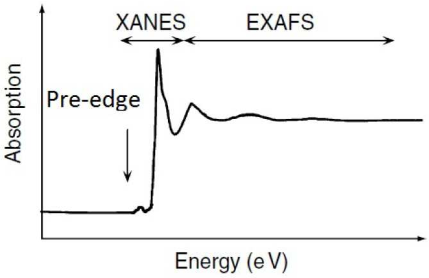

Figure 1.7: In this figure typical X-ray absorption spectra XAS are reported.In addition the main regions of interest Pre-EDGE,XANES e EXAFS are indicated

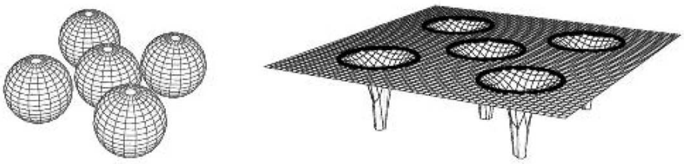

Figure 1.8: The potential muffin-tin is sum of single contribution in non-overlapping spherical region. The photoelectron outgoing from absorbing atom suffers a potential due to the nieghboring atoms

potential acts in a well-defined region of the space and, beyond of that, the potential is set to zero. Then

$$V = \sum_n \upsilon_n(\boldsymbol{r}) \tag{1.21}$$

where $\upsilon_n(\boldsymbol{r})$ is the single atom contribution to the muffin-tin potential. Then the muffin-tin potential consists of non-overlapping well-defined spherical regions (figure 1.7).

Propagation of a photoelectron in a muffin-tin potential is described by Hamiltonian

$$H = H_0 + V \tag{1.22}$$

where H_0 is the unperturbed contribution,consisting of only kinetic operator. In order to obtain eigenstates $|\Psi\rangle$ of the H Hamiltonian operator, the time-independent Schrodinger equation is resolved considering it as non homogeneous partial differential equation.

$$(E - H_0)\,|\Psi\rangle = V\,|\Psi\rangle \tag{1.23}$$

so it is possible to apply the Green function formalism. The solution of homogeneous equation (whose physical meaning is the free particle solution of Schrodinger equation) can be defined in a coordinate rappresentation as $\langle \boldsymbol{r} \mid \phi \rangle$, obtaining

$$(E - H_0)\,\langle \boldsymbol{r} \mid \phi \rangle = 0 \tag{1.24}$$

The free particle Green function G_0 and energy E $= \frac{\hbar^2 k^2}{2m}$ is defined [3]

$$\frac{\hbar^2}{2m}(\nabla^2 + k^2)G_0(\boldsymbol{r},\boldsymbol{r'};E) = \delta(\boldsymbol{r}-\boldsymbol{r'}) \tag{1.25}$$

Morover if the identity

$$\frac{\hbar^2}{2m}(\nabla^2 + k^2)\frac{e^{i\boldsymbol{k}\cdot\boldsymbol{r}}}{\boldsymbol{r}} = -4\pi\delta(\boldsymbol{r}) \tag{1.26}$$

holds, then free particle Green function G_0 takes the analytical form:

$$G_0(\boldsymbol{r},\boldsymbol{r'},E) = -\frac{m}{2\pi\hbar^2}\frac{e^{|\boldsymbol{r}-\boldsymbol{r'}|}}{|\boldsymbol{r}-\boldsymbol{r'}|} \tag{1.27}$$

It is possible to demonstrate that the solution of the inomogeneous equation is the sum of solution of homogeneous equation, adding a particular solution

$$\langle \boldsymbol{r} \mid \Psi\rangle = \langle \boldsymbol{r} \mid \phi\rangle + \int d^3r' G_0(\boldsymbol{r},\boldsymbol{r'};E)\,\langle \boldsymbol{r'} \mid V \mid \Psi\rangle \tag{1.28}$$

In order to perform this calculation, the formal solution of the equation (1.17) is obtained as

$$|\Psi\rangle = |\phi\rangle + \frac{1}{E-H_0 \pm i\eta}V\,|\Psi\rangle \tag{1.29}$$

Due to the singularity in $\frac{1}{E-H_0}$, an imaginary term $i\eta$, infinitesimally small and positive, is added in the denominator. To demonstrate the equation (1.22) we may multiply the previous equation for $\langle\boldsymbol{r}|$, obtaining

$$\Psi(\boldsymbol{r}) = \langle \boldsymbol{r} \mid \Psi\rangle = \langle \boldsymbol{r}|\phi\rangle + \langle \boldsymbol{r}|\frac{1}{E-H_0 \pm i\eta}V|\Psi\rangle \tag{1.30}$$

The first term in the right side is the solution of the homogeneous equation (1.18), i.e. it is the plane wave equation $(\frac{1}{2\pi\hbar})^{2/3}e^{i\boldsymbol{k}\cdot\boldsymbol{r}}$.
By introducing the closed relation $\int d\boldsymbol{r'}\,|\boldsymbol{r'}\rangle\,\langle\boldsymbol{r'}| = 1$ in the previous equation, we can write the equation (1.22) as

$$\Psi(\boldsymbol{r}) = \Big(\frac{1}{2\pi\hbar}\Big)^{2/3}\exp(i\boldsymbol{k}\cdot\boldsymbol{r}) + \int d\boldsymbol{r'}\,\langle\boldsymbol{r}|\frac{1}{E-H_0 \pm i\eta}|\boldsymbol{r'}\rangle\,\langle\boldsymbol{r'}|V|\Psi\rangle \tag{1.31}$$

$$= \Big(\frac{1}{2\pi\hbar}\Big)^{2/3}\exp(i\boldsymbol{k}\cdot\boldsymbol{r}) + \int d\boldsymbol{r'}\,\langle\boldsymbol{r}|\frac{1}{E-H_0 \pm i\eta}|\boldsymbol{r'}\rangle\,V(\boldsymbol{r'})\Psi(\boldsymbol{r}) \tag{1.32}$$

So by defining the Green function as

$$G_0(\boldsymbol{r},\boldsymbol{r'};E) = \langle\boldsymbol{r}|\frac{1}{E-H_0 \pm i\eta}|\boldsymbol{r'}\rangle \tag{1.33}$$

the equation (1.22) is obtained. Moreover we should take into account both the positive term and the negative term of the Green function G_0 which describe as the outgoing and incoming spherical waves respectively propagate in free space. Since we take in account just the positive term of the Green function, the sign ± will be replaced with + and the notation for G_0 further labels will not be taken into account. It is also possible obtain the formal solution of the equation (1.23) through subsequently iterations of the unperturbed solution[6]. For weak scattering potential at the first order, we have the solution $|\Psi\rangle = |\Phi\rangle$ which can be introduced in (1.23) obtaining

$$|\Psi\rangle^{(1)} = G_0 V |\Phi\rangle + |\Phi\rangle \tag{1.34}$$

In order to calculate the second order solution, we introduce the solution obtained in previous step in (1.23)

$$|\Psi\rangle^{(2)} = G_0 V (G_0 V |\Phi\rangle + |\Phi\rangle) + |\Phi\rangle = (G_0 V G_0 V + G_0 V + 1) |\Phi\rangle \tag{1.35}$$

By performing subsequently iterations we obtain

$$|\Psi\rangle = \sum_n (G_0 V)^n |\Phi\rangle = \frac{1}{\boldsymbol{I} - G_0 V} |\Phi\rangle \tag{1.36}$$

In the last equation the sum of the series is written as sum of geometrical series. The hypothesis that it is a geometrical series must be verified, but this check is beyond of our scope. Subsequently we consider to introduce the operator T=$V |\Psi\rangle$ acting on unperturbed solution $|\Phi\rangle$

$$V |\Psi\rangle = T |\phi\rangle \tag{1.37}$$

By comparing this last equation with (1.29), the series expansion (Dyson's expansion) as

$$T = V + V G_0 V + V G_0 V G_0 V + \dots \tag{1.38}$$

By defining the Green function G for the perturbed solution

$$G(E) = \frac{1}{E - H + i\nu} = \left(\frac{1}{G_0^{-1} - V}\right) \tag{1.39}$$

it is possbile calculate

$$G = G_0 + G_0 V G = G_0 + G_0 T G_0, \tag{1.40}$$

and from equation (1.30) or (1.29)

$$T = V + V G_0 T + \dots \tag{1.41}$$

We started this section considering the muffin-tin potential as sum of single spherical potentials, each acting in a well-defined non-overlapping region of the space. Then it is reasonable to write the operator T as sum of terms, each is associate to the single atom

$$t_n = \upsilon_n + \upsilon_n G_0 t_n \tag{1.42}$$

Introducing the single values of t_n in (1.34) and performing the sum over all contributions to the potential V

$$G = G_0 + \sum_n G_0 \upsilon_n G_0 + \sum_{nn'} G_0 \upsilon_n G_0 \upsilon_{n'} G_0 + \dots \tag{1.43}$$

First term corresponds to the no scattered wave, the second one the scattered wave from the nth atom due to the potential υ_n, and third one describes double scattering of the wavematter associate to the photoelectron by nth and n' atoms by means of the potentials υ_n e $\upsilon_{n'}$.
Finally, it is useful to rewrite the Fermi golden rule by means of Green function formalism. Let us to write it as in Brouder's paper [7]

$$W = \frac{2\pi}{\hbar} \sum_f |M_{if}|^2 \delta(E_f - E_i - \hbar\omega) \tag{1.44}$$

The cross section will be

$$\sigma = 4\pi^2 \alpha \hbar\omega \sum_f |M_{if}|^2 \delta(E_f - E_i - \hbar\omega) \tag{1.45}$$

with α fine structure constant. The initial state is well described using an atomic orbital in a inner shell (like 1s) while the final states are calculated in presence of specific hole due to the expulsion of the photoelectron.
From $ImG = \frac{1}{2i}(G^+ - G^-)$ and

$$-\frac{1}{\pi} ImG(r, r', E) = \sum_f |f\rangle\, \delta(E_f - E_i - \hbar\omega)\, \langle f| \tag{1.46}$$

we obtain

$$W = -4\pi\alpha_0 \hbar\omega Im \langle i|\, \widehat{\boldsymbol{\epsilon}} \cdot \overrightarrow{\boldsymbol{r}} G(r, r, E) \widehat{\boldsymbol{\epsilon}} \cdot \overrightarrow{\boldsymbol{r}}\, |i\rangle\, \Theta(E_i + \hbar\omega - E_{Fermi}) \tag{1.47}$$

where the function $\Theta(E_i + h\nu - E_{Fermi})$ is added to take into account the lifetime of the core-hole. The function named W corresponds to the event probability, so it is bound to the equation $\frac{I_{sc}}{I_0}$. In logarithmic scale the previous expression is equal to μd; with equation (1.46) the absorption coefficient is approximated by W as reported by [8].
The multiscattering theory in muffin-tin approximation with Green function approach is the theoretical formalism underlying in some computational package like FEFF, widely used in literature. To evaluate the equation (1.47), it is necessary to calculate the perturbed Green function G, evaluating through the Dyson expansion of the free particle Green functions. Indeed the formalism of equation (1.47) is more complex since the terms showing in this equation are written using the spherical armonics as basis to develop it.
Finally the muffin-tin potential is a good approximation for the EXAFS region of the *XAS* spectra, because the kinetic energy of the photoelectron is higher and multiscattering occurs due to the nucleus potential inside the non-overlapping region. In XANES part of the *XAS* spectrum, the scattering probabily occurs in region outside the action of the spherical potential.
In next section the angular dependece of the absorption cross section will be briefly illustrated, following the Boruder's paper [7]. They will be reported some specific cases of interest treated in this thesis.

1.4 Angular dependence of absorption cross section

In the present section, we reported briefly a theoretical investigation on angular dependece of the absorption cross section, in particular for cristalline system at

higher symmetry belonging to the cubic T_d and O_h puntual group [7].
We start from Hamiltonian operator which describes the interaction between an electron with charge q, mass m, gyromagnetic factor g and spin $\boldsymbol{s}$ in a atomic potential $V(\boldsymbol{r})$ and the electromagnetic field with vector and scalar potential $\boldsymbol{A(r,t)}$ and $\boldsymbol{\Phi(r,t)}$ respectively:

$$H = \frac{1}{2m}[-i\hbar\nabla - q\boldsymbol{A}]^2 + V(\boldsymbol{r}) + q\boldsymbol{\Phi} - (gq/2m)\boldsymbol{s}\cdot\boldsymbol{B} \tag{1.48}$$

Applying the Coulomb gauge $\boldsymbol{\Phi} = 0$ and $\nabla\cdot\boldsymbol{A} = 0$, considering that the term $(q^2/2m)A^2$ is negligible for X-ray source, we obtain

$$H = H_0 + (i\hbar q/m)\boldsymbol{A}\cdot\nabla - (gq/2m)\boldsymbol{s}\cdot\boldsymbol{B} \tag{1.49}$$

with $H_0 = -(\hbar^2/2m)\nabla^2 + V(\boldsymbol{r})$.The incident plane can be written as

$$\boldsymbol{A(r,t)} = A_0\widehat{\epsilon}exp[i(\boldsymbol{k}\cdot\boldsymbol{r} - \omega t)] + A_0\widehat{\epsilon}^*exp[i(\boldsymbol{k}\cdot\boldsymbol{r} - \omega t)] \tag{1.50}$$

where $\widehat{\epsilon}$ is the polarisation vector, $\boldsymbol{k}$ is the X-ray wavevector and A_0 is the vector potential amplitude. By considering a periodical perturbation $w(t) = w_0exp(-i\omega t) + w_0^*exp(i\omega t)$, the transition probability is

$$W = (2\pi/\hbar)\sum_f |\langle f|w|i\rangle|^2\delta(E_f - E_i - \hbar\omega) \tag{1.51}$$

as already reported in (1.10). In our case, where the periodic perturbation is an electromagnetic wave, since $\boldsymbol{B} = \nabla\cdot\boldsymbol{A}$

$$W = Const\cdot\sum_f |\langle f|exp(i\boldsymbol{k}\cdot\boldsymbol{r})[\hbar\widehat{\epsilon}\cdot\nabla - (g/2)\boldsymbol{s}\cdot\boldsymbol{k}\times\widehat{\epsilon}]|i\rangle|^2\times\delta(E_f - E_i - \hbar\omega) \tag{1.52}$$

where $Const = \frac{2\pi q^2|A_0|^2}{\hbar m^2}$ The absorption cross section is obtained from equation (1.51) as

$$\sigma(\omega) = Const\cdot\sum_f |\langle f|exp(i\boldsymbol{k}\cdot\boldsymbol{r})[\hbar\widehat{\epsilon}\cdot\nabla - (g/2)\boldsymbol{s}\cdot(\boldsymbol{k}\times\widehat{\epsilon})]|i\rangle|^2\times\delta(E_f - E_i - \hbar\omega) \tag{1.53}$$

with $Const = (4\pi^2\hbar\alpha/m^2\omega)$. Since the mean radius of the 1s orbital with effective atomic number Z_{eff} is a_0/Z_{eff} with a_0 the Bohr radius, we perform the series expansion of the term $exp(i\boldsymbol{k}\cdot\boldsymbol{r})$ as

$$exp(i\boldsymbol{k}\cdot\boldsymbol{r}) \approx 1 + i\boldsymbol{k}\cdot\boldsymbol{r} \tag{1.54}$$

The dipole electric transition matrix elements is

$$-\big[m\big(E_f - E_i\big)\hbar\big]\langle f|\widehat{\epsilon}\cdot\boldsymbol{r}|i\rangle \tag{1.55}$$

We note the dipolar approximation is not dependent upon wave vector $\boldsymbol{k}$; it is a good approximation for spectroscopy where a low radiation frequency (and low energy) is used, like UV and visible rays. For X-ray spectroscopy this approximation is still applied for proceeses which involve orbitals with reduced spatial extension, like 1s orbital. In dipolar approximation we found just the dependence of the cross section form polarization vector $\widehat{\epsilon}$. The cross section can be written as

$$\sigma^D(\widehat{\epsilon}) = \sigma^D(0,0) - \sqrt{8\pi/5}\sum_{m=-2}^{2} Y_2^{m*}\sigma^D(2,m) \tag{1.56}$$

where the first term is the isotropic absorption cross section,while the second term is a mesure of angular dependence between $\widehat{\epsilon}$ and $\boldsymbol{k}$. The term $\sigma^D(l,m)$ is the mth component of a spherical tensor of rank l and transform under rotation like the spherical harmonics Y_l^{m*}.
Let us to introduce the notation for $\widehat{\epsilon}$ in orthogonal spherical coordinates

$$\widehat{\epsilon} = \begin{pmatrix} \sin\theta\cos\phi \\ \sin\theta\sin\phi \\ \cos\theta \end{pmatrix} \tag{1.57}$$

with usual definiton for ϕ and θ. For systems with cubic symmetry and puntual groups O_h and T_d, like Fe-bcc and Silicon respectively, it is possible to show that in the cross section (equation 1.54) $\sigma^D(2,m) = 0$ for all m; so the absorption cross section due to the dipole transition does not show angular dependence, i.e. it is isotropic.
Regarding another crystalline system of interest, we take in account the puntual group C_1 with lowest symmetry. In this case the only symmetry element is the axes C_{360}. It is found a complicated angular dependence of cross section:

$$\begin{aligned} \sigma^D(\widehat{\epsilon}) = \sigma^D(0,0) - \sqrt{3}[\cos 2\phi\sigma^{D_r}(2,2) + \sin^2\phi\sigma^{D_i}(2,2)]+ \\ +2\sqrt{3}\cos\theta[\cos\phi\sigma^{D_r}(2,1) + \sin\phi^{D_i}(2,1) - \frac{3\cos^2\theta - 1}{\sqrt{2}}\sigma^D(2,0) \end{aligned} \tag{1.58}$$

we introduce the notation $\sigma^{D_r}(l,m)$ and $\sigma^{D_i}(l,m)$ because the dipolar cross section $\sigma^D(l,m)$ is a complex number where $\sigma^D(l,m) = \sigma^{D_r}(l,m) + \sigma^{D_i}(l,m)$ considering σ^D real. It is possible to choose six possible independent polarization vectors $\widehat{\epsilon}$ obtaining six estimates of σ_D in the left-hand side of the equation, as linear combinations of $\sigma(l,m)$.

$$\begin{pmatrix} \sigma_a \\ \sigma_b \\ \sigma_c \\ \sigma_d \\ \sigma_e \\ \sigma_f \end{pmatrix} = K \begin{pmatrix} \sigma^D(0,0) \\ \sigma^{D_r}(2,2) \\ \sigma^{D_i}(2,2) \\ \sigma^{D_r}(2,1) \\ \sigma^{D_i}(2,1) \\ \sigma^D(2,0) \end{pmatrix} \tag{1.59}$$

In order to compute the set of σ_j, we can inverte the equation (1.57) with $\det K \neq 0$. Then, each term $\sigma(l,m)$ is a linear combination of σ_j for j=a,b,c,d,e,f which are measurable. We can set the polarization vector in a restricted number of positions in order to get the isotropic part of σ^D, i.e. σ_0. These positions are used as input in *XSpectra* package, which will be illustrated in chapter 4.
By selecting $\sin\theta = 0$ and $\cos^2\theta = 1$ we are be able to isolate just the isotropic contribution $\sigma^D(0,0)$ of the dipolar cross section. Fixing the three directions of

the polarization vector as $\widehat{\epsilon}_a = (1,0,0)$,$\widehat{\epsilon}_b = (0,1,0)$ and $\widehat{\epsilon}_c = (0,0,1)$ and by inverting the previous relationship, we obtain

$$\sigma^D(0,0) = \frac{\sigma^D(1,0,0) + \sigma^D(0,1,0) + \sigma^D(0,0,1)}{3} \tag{1.60}$$

Then the isotropic cross section in general is given by the average of three cross section (each cross section is given by single *XSpectra* calculations) taking as $\widehat{\epsilon}$ the three basic unit vectors.

Chapter 2

Projector Augmented Wave method

2.1 Introduction to PAW formalism

In the recent years,first-principles methods (or *ab-initio* methods)for electronic structure calculations have been widely employed to study physical properties of the condensed matter. This enormous development is manly due to high flexibility, increasing of computing power and also due to available computational infrastructures.

Density Functional Theory (DFT) plays a primary role regarding *ab-initio* methods in several applications (from biological systems to solid state physics) due to great flexibility and reduced computational cost, comparing to Hartree-Fock methods[9].

The DFT method maps the electronic ground state of an interacting electron gas onto the ground state of noninteracting electrons, which experience an effective potential. Hohenberg and Kohn proved [9] that the ground state electronic energy E_0 is a functional of n_0 with $E_0 = E[n_0]$. In second Hohenberg and Kohn theorem every trial density function n_s of N noninteracting electron gas that fulfills $\int n_s(\boldsymbol{r})d\boldsymbol{r} = N$ and $n_s(\boldsymbol{r}) \geq 0$, the inequality $E_0 \leq E_s$ holds. E_0 and E_s are the energy functional for the ground state of interacting and noninteracting electron gas respectively. It means that the true ground state electron density minimizes the energy functional $E_0 = E[n_0]$ where n_0 is the ground state electronic density of the interacting electron gas. By Hohenberg and Kohn theorem, n_s determines an external potential u_s which in turn determines the fictitious wave function of the noninteraction electron gas, corresponding to the density n_s. In principle the DFT is an exact procedure to determine the ground state and other ground state molecular properties, but the anaytical expression of $E = E[n_0]$ is unknown. In practice to apply the DFT method it is necessary introduce a correlation-exchange functional as reported in [9].

The integro-differential Kohn-Sham equations underlie to DFT method, where the Hamiltonian operator contains the unknown exchange-correlation term. In this framework, functional built *ad-hoc* are employed , proving their accuracy by means of calculation on system of interest and comparing the results with well-known literature data. In order to resolve the Kohn-Sham equations, two

approachs can be applied; the LCAO (*Linear Combination Atomic Orbital*) and pseudopotentials methods. The LCAO method consists to perform an expansion of the Kohn-Sham single-particle wave on atomic orbitals basis, centered on each atom whereas in the second one the Kohn-Sham equations are resolved using a semplified Hamiltonian. The latter method will be widely illustrated in the next chapter while the LCAO approach will not be taken in account in this thesis.
Indeed there are other calculation schemes to resolve the Kohn-Sham equations. For example it has been developed further methods like LAPW (*Linear Wave Plane Augmented*) and the its semplified version, the LMTO (*Linear Muffin-Tin Orbital*) methods. All these approaches are APW-based scheme where APW (*Wave Plane Augmented*) is a method introduced by Slater [10] in 1937. The linear method deal with the full wave functions and treat all elements in the Periodic Table on the same footing [10].
To introduce the Projector Augmented Wave (PAW) method[11] it is useful to consider the many-body wave function of real material have very different signaturs in different regions of space: in the bonding region the wave function is smooth, whereas close to the nucleus a rapid oscillatory beahviour is experienced, due to the large attrattive potential of the nucleus. The accuracy of description of the region close the nucleus is necessarly poor respect to the bonding region. We indicate the real wave function as single particle wave function obtained by exact resolution of Kohn-Sham many body scheme (the *all electron* function) without further approximation and labeled as $|\Psi\rangle$.
The strategy of the augmented-wave methods has been to divide the wave function into parts, a partial-wave expansion within an atom-centered sphere and envelope functions outside the spheres. The envelope function is expanded into plane waves basis set. In the frontier region the envelope function and partial-wave expansion are matched with value and their derivative. The Hamiltonian operator for N electrons interacting system is defined as (in atomic unit)

$$\widehat{H} = -\frac{1}{2}\sum_{k=1}^{N}\nabla_k^2 + \sum_{k=1}^{N} u(\boldsymbol{r}_k) + \sum_{k \neq k'=1}^{N} \nu(\boldsymbol{r}_k; \boldsymbol{r}'_{k'}) \tag{2.1}$$

The pseudopotential approach works replacing the real interacting electron-nucleus potential $u(\boldsymbol{r}_k)$ in Hamiltonian operator by smoother potential, as reported in figure (2.1). In fact the strongly oscillating region of the valence wave functions is due to the interacting electron-nucleus potential $u(\boldsymbol{r}_k)$, diverging close to nucleus. The plane wave basis expansion of this wave function required an enormous dimension of the basis set, yielding impractical the calculations. By introducing pseudopotentials, we replace the true valence wave functions by pseudo wave functions which match exactly the true valence wave functions outside certain regions so-called core region but are nodeless inside.

The pseudopotential approach will be widely described in next chapter. Here we will introduce briefly their properties to illustrate the projector augmented-wave formalism. Our purpose is to build an efficient tool to modify the real wave function (the Kohn-Sham wave function) to remove the oscillations, restricted in augmented region. To pursue this aim, let us to consider the *all-electron* wave function $|\Psi\rangle$ in Hilbert space $\mathcal{H}$. We transform this wave function into a new Hilbert space,named pseudo-Hilbert space $\mathcal{H}^{\mathcal{PS}}$, spanned by smooth or pseudo wave functions $|\tilde{\Psi}\rangle$. This transformation is performed by means of transformation

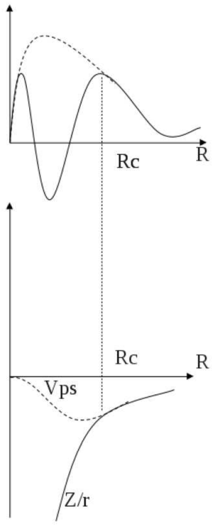

Figure 2.1: In figure electron-nucleus interaction potential Z/r is replaced by smoother function.The potential does not show divergent behaviour close to the nucleus and the corresponding wave function is smoother

operator $\widehat{T}$, so that

$$|\Psi\rangle = \widehat{\mathcal{T}}\,|\tilde{\Psi}\rangle \tag{2.2}$$

All the *pseudofunctions* will be labeled using symbol ˜ or *PS*; on the contrary the wave functions *all-electron* without any symbology. In addition we consider only valence wave functions whereas the core orbitals will be labeled using *c*.
Let us to consider an operator $\widehat{A}$ in Hilbert space $\mathcal{H}$ whose expectation value $\langle\widehat{A}\rangle = \langle\Psi|A|\Psi\rangle$ corresponding to generic physical observable A. The term $\langle\widehat{A}\rangle$ must be equal to $\langle\tilde{A}\rangle$, and the latter is

$$\langle\tilde{A}\rangle = \langle\tilde{\Psi}|\tilde{A}|\tilde{\Psi}\rangle \tag{2.3}$$

Then the operator $\widehat{A}$ transforms as

$$\tilde{A} = \mathcal{T}^{+}\widehat{A}\mathcal{T} \tag{2.4}$$

In a well-defined augmented region Ω_R, the wave function *PS* $|\tilde{\Psi}_k\rangle$ for each kth electronic state can be written as expansion in partial wave (*partial waves*) inside Ω_R

$$|\tilde{\Psi}_k\rangle = \sum_j \tilde{C}_{jk}\,|\tilde{\phi}_j^R\rangle \tag{2.5}$$

By applying the operator $\widehat{\mathcal{T}}$ to equation (2.5), we obtain

$$|\Psi_k\rangle = \sum_j C_{jk}\,|\phi_j^R\rangle \tag{2.6}$$

where $\widehat{\mathcal{T}}\,|\tilde{\Psi}_k\rangle = |\Psi_k\rangle$ e $|\phi_j^R\rangle = \widehat{\mathcal{T}}\,|\tilde{\phi}_j^R\rangle$. Moreover we consider the coefficient in (2.5) and (2.6) as equivalent, so as $\tilde{C}_{jk} = C_{jk}$.
From equation (2.6), adding a substracting $\sum_j \tilde{C}_{jk}\,|\widetilde{\phi_j^R}\rangle$, we obtain

$$|\Psi_k\rangle = |\tilde{\Psi}_k\rangle - \sum_j C_{jk}\,|\widetilde{\phi_j^R}\rangle + \sum_j C_{jk}\,|\phi_j^R\rangle \tag{2.7}$$

By indicating the projector function as $\langle\tilde{p}_i^R|$ restricted into augmented region Ω_R, the coefficients C_{jk} are the scalar product $\langle\tilde{p}_i^R|\tilde{\Psi}_k\rangle$. By using the condition

$$|\tilde{\Psi}_k\rangle = \sum_j \langle\tilde{p}_j^R|\tilde{\Psi}_k\rangle\,|\tilde{\phi}_j^R\rangle \tag{2.8}$$

$\sum_j |\tilde{\phi}_j^R\rangle\,\langle\tilde{p}_j^R| = 1$ is carried out for $|\tilde{\Psi}_k\rangle = |\tilde{\Psi}_k\rangle$.
By replacing the definition $\langle\tilde{p}_i^R|\tilde{\Psi}_k\rangle$ nella (2.7) we obtain:

$$|\Psi_k\rangle = |\tilde{\Psi}_k\rangle - \sum_j |\widetilde{\phi_j^R}\rangle\,\langle\tilde{p}_i^R|\tilde{\Psi}_k\rangle + \sum_j |\phi_j^R\rangle\,\langle\tilde{p}_i^R|\tilde{\Psi}_k\rangle$$

Collecting the term $|\tilde{\Psi}_k\rangle$, the previous equation can be written as

$$|\Psi_k\rangle = \Big[1 + \sum_j |\phi_j^R\rangle\,\langle\tilde{p}_i^R| - \sum_j |\tilde{\phi}_j^R\rangle\,\langle\tilde{p}_i^R|\Big]\,|\tilde{\Psi}_k\rangle$$

Finally, it is possible to define the transformation operator $\widehat{\mathcal{T}}$ introducing the notation $\widehat{\mathcal{T}}_R$ on each augmented region R:

$$\widehat{\mathcal{T}}_R = \sum_j \left(|\phi_j^R\rangle - |\tilde{\phi}_j^R\rangle \right) \langle \tilde{p}_j^R| \tag{2.9}$$

By remembering the equation (2.2)

$$|\Psi_k\rangle = |\tilde{\Psi}_k\rangle + \sum_R \sum_j \left(|\phi_j^R\rangle - |\tilde{\phi}_j^R\rangle \right) \langle \tilde{p}_i^R|\tilde{\Psi}_k\rangle \tag{2.10}$$

the operator $\widehat{\mathcal{T}}$ will be defined as

$$\widehat{\mathcal{T}} = 1 + \sum_R \widehat{\mathcal{T}}_R \tag{2.11}$$

To obtain the transformation operator $\widehat{\mathcal{T}}$ it is necessary to determine, in agreement to equation (2.9), three terms: the *partial waves all electron (AE)* $|\phi_j^R\rangle$ calculated integrating the Schrodinger equation for single atom; the *partial waves pseudo function* $|\tilde{\phi}_j^R\rangle$ by resolving the pseudopotential problem for single atom; the projector function $\langle \tilde{p}_j^R|$, obtained in agreement to the relation $\langle \tilde{p}_i^R|\tilde{\phi}_j^R\rangle = \delta_{ij}$. Finally, coherenting with each APW approach, outside of the augmented region the function l AE and PS must coincide, then the raltion $|\phi_j^R\rangle = |\tilde{\phi}_j^R\rangle$ holds.
It is important to stress that the operator $\widehat{\mathcal{T}}$ allows to map the single particle wave function $|\tilde{\Psi}_k\rangle$ onto all electron single particle wave function $|\Psi_k\rangle$. The former is obtained through pseudopotential approach with reduced computational cost, whereas the latter resulting the exact solution in DFT framework. In practice it allows to perform a reconstruction of the real Kohn-Sham wave function. This reconstruction is exact for infinite expansions of projector basis functions.
Next step is to calculate the expectation value of the hamiltonian operator $\langle \widehat{\mathcal{H}} \rangle = \langle \Psi|\widehat{\mathcal{H}}|\Psi\rangle$, using the previous formalism. Now we need to be able to obtain observable quantities as the expectation values of the PS wave functions. We also need to transform the real operator A into new $\tilde{A}$, in function of partial waves.

$$\tilde{A} = \widehat{A} + \sum_{ij} |\tilde{p}_j^R\rangle \left(\langle \phi_i^R|\widehat{A}|\phi_j^R\rangle - \langle \tilde{\phi}_i^R|\widehat{A}|\tilde{\phi}_j^R\rangle \right) |\tilde{p}_j^R\rangle \tag{2.12}$$

We note that there are three main contributions which characterize the $\tilde{A}$ with expectation value $\langle \tilde{\Psi}|\tilde{A}|\tilde{\Psi}\rangle$. First term is an operator that directly acts on the PS wave function $|\tilde{\Psi}\rangle$ while the remaining two parts contain the projectors and the expectation value of the operator A based on functions i $|\tilde{\phi}_j^R\rangle$ and $|\phi_j^R\rangle$. This kind of transormation which produces three different contributions will be always present in PAW formalism. In our case two important physical quantity will be transformed in agreement to equation (2.12), electronic density and total energy of the system. Each contribution acts on augmented region Ω_R.
Unitl now we have used the label R to indicate the terms defined onto augmented region; for example the partial waves and projectors $|\tilde{\phi}_j^R\rangle$, $|\phi_j^R\rangle$ and $\langle \tilde{p}_j^R|$ respectively. In order to semplify the notation, we assume that the terms acting in augmented regions Ω_R are dependent implicitly by R,without any further

notation.

In the original Blochl's paper the energy total in PAW formalism is derived explicity in DFT framework, considering the kinetic energy, the Hartree potential and the correlation-exchange functional. We will write the mono and bielectronic matrix operator elements using the operator $\mathcal{T}$ as reported in (2.9), which allows to map the wave function Ψ_k onto $\tilde{\Psi}_k$. By considering that the monoelectronic operator A is written of occupation function f_k as $\sum_k f_k \langle\Psi_k|A|\Psi_k\rangle$, total Kohn-Sham energy as

$$E = \sum_k f_k \langle\Psi_k| - \frac{1}{2}\Delta^2|\Psi_k\rangle + E_H[n + n_Z] + E_{XC}[n + n_Z] \tag{2.13}$$

where n is the total charge density and n_Z the puntual nuclear charge. The functional $E_H[n+n_Z]$ e $E_{xc}[n+n_Z]$ are Hartree energy and correlation-exchange terms.

Electronic charge density $n(\boldsymbol{r})$ is the operator monoelectronic expectation value $|\boldsymbol{r}\rangle\langle\boldsymbol{r}|$ which transforms in agreement to (2.12) onto $\tilde{n}(\boldsymbol{r}) = \sum_k f_k \langle\tilde{\Psi}_k|\boldsymbol{r}\rangle\langle\boldsymbol{r}|\tilde{\Psi}_k\rangle$, $n^1(\boldsymbol{r}) = \sum_{ij}\rho_{ij}\langle\phi_i|\boldsymbol{r}\rangle\langle\boldsymbol{r}|\phi_j\rangle$ and $\tilde{n}^1(\boldsymbol{r}) = \sum_{ij}\rho_{ij}\langle\tilde{\phi}_i|\boldsymbol{r}\rangle\langle\boldsymbol{r}|\tilde{\phi}_j\rangle$ where we define

$$\rho_{ij} = \sum_k f_k \langle\tilde{\Psi}_k|\tilde{p}_i\rangle\langle\tilde{p}_j|\tilde{\Psi}_k\rangle \tag{2.14}$$

as occupation function of each (i,j)th channel. The meaning of f_k is a function describing how many particles fill the $\boldsymbol{k}$-state. In this case the terms label with 1 are defined into augmented region.

The terms of the total energy reported subsequently are slightly different from Blochl derivation in [11] in order to stress the analogy with Vanderbilt approach in [12]. This new PAW derivation scheme has been carry out by Kress and Joubert [13]. Electronic density terms n,n^1,$\tilde{n}^1$ are defined for valence electrons whereas the core electrons are frozen (*frozen-core approximation*).

We define n_c,n_Z,$\tilde{n}_c$ e $\tilde{n}_Z$ for core electrons and nuclear charge AE e PS; outside of core regions of r_c but inside of augmented regions, the charge densities n_c AE and PS match. Furthmore by defining $n_{Zc} = n_c + n_Z$, we obtain $\int_\Omega n_{Zc}(\boldsymbol{r})d^3\boldsymbol{r} = \int_\Omega \tilde{n}_{Zc}(\boldsymbol{r})d^3\boldsymbol{r}$.

In Bochl and Kress papers [11][13] the complete derivation of the total energy expression are illustrated. We see that the all electron total electronic density n_T is written as sum of terms n, which is the electronic density of valence, and n_{Zc}; the latter corrisponding to the sum of core and nuclear density.

$$n_T = n + n_{Zc} \tag{2.15}$$

Subsenquently, by remembering that n_T transforms as $\tilde{n}_T$,$\tilde{n}^1_T$ and n^1_T in agreement to (2.12), it is found

$$n_T = \tilde{n}_T + n^1_T + \tilde{n}^1_T \tag{2.16}$$

Each term in n on the left-hand side in (2.16) is

$$\tilde{n}_T = \tilde{n} + \tilde{n}_{Zc}$$

$$n^1_T = n^1 + n_{Zc}$$

$$\tilde{n}_T^1 = \tilde{n}_{Zc} + \tilde{n}^1$$

By regarding the charge density n_T e $\tilde{n}_T$, they are different inside of augmented regions; the latter is a PS function viewed as an approximation of the the former, which is all-electron; outside of Ω_R they must match. In order to reproduce the real charge density inside of the augmented region, the term $\widehat{n}$ are added to $\tilde{n}_T$ e $\tilde{n}_T^1$, so $\tilde{n}_T$ must be reproduce the corrected multipole moments obtained from n_T^1.So

$$\tilde{n}_T = \tilde{n} + \tilde{n}_{Zc} + \widehat{n} \tag{2.17}$$

and also for $\tilde{n}_T^1$. Obviously the term $n_T^1 = n^1 + n_{Zc}$ does not suffer change. Both n_T^1 and $\tilde{n}_T$ contained in Z_c are equivalent because they produce just the monopole moment, which corresponds to the sum between nuclear charge and electrostatic core charge; higher order of the moment expansions are negligible because the charge is strongly localized in a point $\boldsymbol{r}$ of the space. In practice the term $\widehat{n}$ acts just in $\tilde{n}$ reproducing the moments of n^1. The choice of function $\widehat{n}$ is not unique but any other choice must be fulfill the previous requirement. See the reference [13]. Now we can introduce the total energy terms, by remembering that the energy is the expectation value of the Hamiltonian operator, transforming in agreement to (2.12). Each value to energy contribution must fulfill the (2.12). By according with equation (2.15) and (2.16), we obtain

$$\begin{aligned} E[n_T] &= \tilde{E}[\tilde{n}_T] + E^1[n_T^1] - \tilde{E}^1[\tilde{n}_T^1] = \\ &= \tilde{E}[\tilde{n} + \tilde{n}_{Zc} + \widehat{n}] + E^1[n^1 + n_{Zc}] - \tilde{E}^1[\tilde{n}^1 + \widehat{n} + \tilde{n}_{Zc}] \end{aligned} \tag{2.18}$$

First term $\tilde{E}[\tilde{n}_T]$ is depending from electronic density contributions $\tilde{n}.\tilde{n}_{Zc}$ and $\widehat{n}$,

$$\tilde{E} = \sum_k f_k \langle \Psi_k| - \frac{1}{2}\nabla^2 |\Psi_k\rangle + E_{XC}[\tilde{n}+\widehat{n}+\tilde{n}_c] + E_H[\tilde{n}+\widehat{n}] + \int \nu_H[\tilde{n}_{Zc}](\tilde{n}(\boldsymbol{r})+\widehat{n}(\boldsymbol{r}))d\boldsymbol{r} + U(R,Z) \tag{2.19}$$

the second in (2.18) is

$$\tilde{E}^1 = \sum_k \rho_{ij} \langle \tilde{\phi}_i| - \frac{1}{2}\nabla^2 |\tilde{\phi}_j\rangle + \overline{E_{XC}[\tilde{n}^1 + \widehat{n} + \tilde{n}_c]} + \overline{E_H[\tilde{n}^1 + \widehat{n}]} + \int \nu_H[\tilde{n}_{Zc}](\tilde{n}^1(\boldsymbol{r})+\widehat{n}(\boldsymbol{r}))d\boldsymbol{r} \tag{2.20}$$

, and third term $E^1[n_T^1]$ will be

$$E^1 = \sum_k \rho_{ij} \langle \phi_i| - \frac{1}{2}\nabla^2 |\phi_j\rangle + \overline{E_{XC}[n^1 + n_c]} + \overline{E_H[n^1]} + \int \nu_H[n_{Zc}] n^1(\boldsymbol{r}) d\boldsymbol{r} \tag{2.21}$$

For all three expressions, we indicate with E_H the coulomb electrostatic energy $E_H = \frac{1}{2}\int\int d\boldsymbol{r}d\boldsymbol{r'} \frac{n(\boldsymbol{r})n(\boldsymbol{r'})}{|\boldsymbol{r}-\boldsymbol{r'}|}$ whereas by $\nu_H[n]$ we indicate external potential included in Kohn-Sham equations $\nu_H[n(\boldsymbol{r})] = \int \frac{n(r')}{|\boldsymbol{r}-\boldsymbol{r'}|} d\boldsymbol{r'}$. The term marked with $'-'$ are valuated on integration grid inside certain radius of the augmented region; on the contrary the other terms are calculated by using plane wave expansion. Finally we mention that the contribution $\tilde{E}$ is much similar to the functional energy of the Ultrasoft (US) Venderbilt method, when th density $\tilde{n}$ in PAW formalism corresponds to the pseudo-density derived in US derivation.

2.2 Absorption cross section in PAW scheme

In chapter 1 we introduced briefly the X-ray absorption mechanism, underlying to the XANES and EXAFS spectroscopy. The absorption cross section was introduced as

$$\sigma_a = 4\pi^2 \alpha\hbar\omega \sum_f |M_{if}|^2 \delta(E_f - E_i - \hbar\omega) \tag{2.22}$$

where the matrix element M_{if} in dipolar approximation is written as $\hat{\epsilon} \cdot \overrightarrow{\boldsymbol{r}}$. By generalizing the expression for absorption cross section, beyond the dipolar approximation, we found

$$\sigma_a = 4\pi^2 \alpha_0 \hbar\omega \sum_f |\langle \Psi_f | \hat{\epsilon} \cdot \overrightarrow{\boldsymbol{r}} + \frac{i}{2}(\hat{\epsilon} \cdot \overrightarrow{\boldsymbol{r}})(\overrightarrow{\boldsymbol{k}} \cdot \overrightarrow{\boldsymbol{r}}) | \Psi_i \rangle|^2 \delta(E_f - E_i - h\nu) \tag{2.23}$$

The all-electron function $|\Psi_k\rangle$ in PAW formalism is written as $|\Psi_k\rangle = \hat{\mathcal{T}}\,|\tilde{\Psi}_k\rangle$ where $|\tilde{\Psi}_k\rangle$ we indicate the PS wave.
The matrix element $\langle \Psi_f | \mathcal{D} | \Psi_i \rangle$ is the expectation value of the operator $\mathcal{D} = \hat{\epsilon} \cdot \overrightarrow{\boldsymbol{r}} + \frac{i}{2}(\hat{\epsilon} \cdot \overrightarrow{\boldsymbol{r}})(\overrightarrow{\boldsymbol{k}} \cdot \overrightarrow{\boldsymbol{r}})$ which transforms as (2.12).
By writing the operator $\mathcal{T}$ as in (1.11), it is found that

$$\hat{\mathcal{T}} = 1 + \sum_R \sum_j \left(|\phi_j^R\rangle - |\tilde{\phi}_j^R\rangle \right) \langle \tilde{p}_j^R | \tag{2.24}$$

This transformation applied to $|\tilde{\Psi}_k\rangle$ produces, as already illustrated previously, three different terms. In case of transition matrix, the transformation (2.12) is applied to the wave function which describes the final state of the system after collision with X-ray photon. So from *all electron* $|\Psi_f\rangle$ function, we obtain the PS function $|\tilde{\Psi}_f\rangle$. The latter is calculated by traditional pseudoptentials approach, eventually with core-hole effect. In addition the intial state is well known as orbitals 1s or 2s where the *photoelectron* is extracted and no transformation is performed.
The matrix element is written as

$$M_{if} = \langle \tilde{\Psi}_f | D | \Psi_i \rangle + \sum_{Rj} \langle \phi_j^R | D | \Psi_i \rangle \langle \tilde{\Psi}_f | \tilde{p}_j^R \rangle - \sum_{Rj} \langle \tilde{\phi}_j^R | D | \Psi_i \rangle \langle \tilde{\Psi}_f | \tilde{p}_j^R \rangle \tag{2.25}$$

By considering the absorption process which involes just one atomic site,named R_0, the summatory $\sum_R$ runs over the single term R_0 and a semplified version of transition matrix is obtained

$$M_{if} = \sum_j \langle \tilde{\Psi}_f | \tilde{p}_j^{R_0} \rangle \langle \phi_j^{R_0} | D | \Psi_i \rangle \tag{2.26}$$

where the first and the last term are negligible for closing relation $\sum_j |\tilde{\phi}_j^{R_0}\rangle \langle \tilde{p}_j^{R_0}| = 1$ applied to third term of equation (2.25). Finally, we rewrite the expression of the cross section, introducing the equation (2.26) into (2.22)

$$\sigma = 4\pi^2 \alpha_0 \hbar\omega \sum_f \left| \sum_j \langle \tilde{\Psi}_f | \tilde{p}_j^{R_0} \rangle \langle \phi_j^{R_0} | D | \Psi_i \rangle \right|^2 \delta(E_f - E_i - \hbar\omega) \tag{2.27}$$

The ingredients to determine the cross section by means of *ab initio* method in DFT-PAW scheme[14][15] are the partial functions $|\phi_j^{R_0}\rangle$, the projectors $\langle\tilde{p}_j^{R_0}|$ and the wave functions of final state PS $|\tilde{\Psi}_f\rangle$.
In the next chapter, it will introduce the psudopotentials formalism, here it has been done a brief mention, stressing the Ultrasoft Vanderbilt approach. In this scheme, a powerfull calculation tools are introduced in order to perform the simulation of *ab initio* XANES cross section.

Chapter 3

The Pseudopotential Plane Wave Method

3.1 Introduction to the wave plane basis formalism

In the last chapter the *Projector Augmented Method (PAW)* as powerfull computational techniques for electronic structure calculations, has been widely illustrated. In order to introduce the PAW approach, we mentioned the Pseudoptentials (PP) techniques, currently employed in computational chemistry and computational material science to resolve complicated many-body problems. The reasons of the widely diffusion and successful of this approach are due, in particular, to the formal semplicity and reduced computational cost.
In fact, it is well-known, that the problem of strongly interacting electrons can be mapped onto a problem of single-particle, moving in an external potential genereted by electron-nucleus attraction for fixed nuclei positions (Born-Oppenheimer approximation). The hamiltonian operator for many body problem is (in atomic unit)

$$\widehat{H} = -\frac{1}{2}\sum_{k=1}^{N}\nabla_k^2 + \sum_{k=1}^{N} u(\boldsymbol{r}_k) + \sum_{k\neq k'=1}^{N} \nu(\boldsymbol{r}_k;\boldsymbol{r'}_{k'}) \tag{3.1}$$

Within density function theory framework, a *non interacting system* of N noninterecting electrons, that each suffers the same external potentials ν_s, is taken in account. The potential labeled by ν_s is generated by ground-state electron density n_s of the reference system (with n is indicated the G.S. for the real system); there is a direct correspondence between n_s and ν_s and the identity $n_S = n$ holds.
If the electronic density for the ground states $n(\boldsymbol{r}) = \sum_{k=1}^{N} |\phi_k^{KS}(\boldsymbol{r})|^2$ of the *non interecting system* is build by using N Kohn-Sham orbitals ϕ^{KS}, the corrisponding energy is given

$$E^{KS}[n] = \sum_{k=1}^{N} \langle\phi_k^{KS}(\boldsymbol{r})| -\frac{1}{2}\nabla_k^2|\phi_k^{KS}(\boldsymbol{r})\rangle + \int d\boldsymbol{r}d\boldsymbol{r'}\frac{n(\boldsymbol{r})n(\boldsymbol{r'})}{|\boldsymbol{r}-\boldsymbol{r'}|} + \int n(\boldsymbol{r})\nu(\boldsymbol{r}) + E^{XC}[n(\boldsymbol{r})]$$

or in more compact way

$$E^{KS}[n] = K[n(\boldsymbol{r})] + E^{\nu}[n(\boldsymbol{r})] + E^{ee}[n(\boldsymbol{r})] + E^{xc}[n(\boldsymbol{r})] \tag{3.2}$$

Now, the Kohn-Sham equations can be obtained by means of a functional minimization of the energy $E^{KS}[n]$; this minimization is achieved variyng the electronic density, or the Kohn-Sham orbitals. Minimizing the expression (3.2), the Kohn-Sham operator for interacting system is given

$$\widehat{H}_{KS} = -\frac{1}{2}\nabla^2 + \int d\boldsymbol{r}\frac{n(\boldsymbol{r'})}{|\boldsymbol{r}-\boldsymbol{r'}|} + \nu(\boldsymbol{r}) + V_{xc}[n(\boldsymbol{r})] \tag{3.3}$$

where $-\frac{1}{2}\nabla^2$ is the kinetic energy operator for single electron, $\int d\boldsymbol{r}\frac{n(\boldsymbol{r'})}{|\boldsymbol{r}-\boldsymbol{r'}|}$ is the electron-electron potential (called also *Hartree potential* V_H), $\nu(\boldsymbol{r})$ is the electron-nucleus potential and $V_{xc}[n(\boldsymbol{r})]$ is the exchange-correlation potential.
To resolve the resulting single-particles Kohn-Sham equations, we need to build up a pratical numerical scheme of calculations. The linear combination of Molecular Orbitals (LCAO method) is widely used in particular for chemical problems;in this case the gaussian basis-set expansion of the Kohn-Sham orbitals are used, and the Kohn-Sham equations are transformed into a set of algebraic equations. This approach is not useful to obtain informations about transport properties and generally is applied for chemical practice problems. For example insulators materials are described very well by LCAO methods but this approach fails when electronic and transport properties of the metal or semiconductor must be obtained. Generally a wave plane expansion of the wave function single-particles (or Kohn-Sham orbitals) is used to describe extended system like metal and in general for solid states systems. In addition wave plane basis set are the exact eigenfunctions of the homogeneous electron gas, therefore, they are natural choice for a basis expansion of the electron wave functions for metal and conductor materials.
The electron wave function in a periodic system suffers the interaction with a periodic potential whose periodicity is fixed by vectors lattice given by

$$\boldsymbol{T} = n_1\boldsymbol{a_1} + n_2\boldsymbol{a_2} + n_3\boldsymbol{a_3} \tag{3.4}$$

where $\{n_i\}_{i=1}^3$ are integer numbers and $\boldsymbol{\{a_i\}}_{i=1}^3$ are three vectors describing the box of atoms repeated periodically in all three spacial directions, which rappresents our system of interest. The volume of the crystallographic cell is usually defined as $V_{\omega_r} = \boldsymbol{a_1} \cdot \boldsymbol{a_2} \times \boldsymbol{a_3}$.
It is well known that the solution of a single-particle Schrodinger equation with a periodic potential $\Psi(\boldsymbol{r})_k$ for generic state k, fulfils the Bloch theorem[16]

$$\Psi_{\boldsymbol{k},j}(\boldsymbol{r}) = u_{\boldsymbol{k},j}(\boldsymbol{r})e^{i\boldsymbol{k}\cdot\boldsymbol{r}} \tag{3.5}$$

Then, we can write the Kohn-Sham equations as

$$\left(-\frac{1}{2}\nabla^2 + \int d\boldsymbol{r'}\frac{n(\boldsymbol{r'})}{|\boldsymbol{r}-\boldsymbol{r'}|} + \nu(\boldsymbol{r}) + V_{xc}[n(\boldsymbol{r})]\right)\Psi_{\boldsymbol{k},j}(\boldsymbol{r}) = E_{\boldsymbol{k},j}\Psi_{\boldsymbol{k},j}(\boldsymbol{r}) \tag{3.6}$$

The single particle Kohn Sham wave function is written as a periodic function $u_k(\boldsymbol{r})$ modulated by plane wave with wave vector $\boldsymbol{k}$ and band index j.

Since the function $u_k(\boldsymbol{r})$ is a periodic function, it can be written in a wave plane rappresentation as [17]

$$u_k(\boldsymbol{r}) = \sum_{\boldsymbol{G}} C_{\boldsymbol{G},\boldsymbol{k}} e^{i\boldsymbol{G}\cdot\boldsymbol{r}} \tag{3.7}$$

and the single-particles Kohn-Sham wave function:

$$\Psi_k(\boldsymbol{r}) = \sum_{\boldsymbol{G}} C_{\boldsymbol{G},\boldsymbol{k}} e^{i(\boldsymbol{G}+\boldsymbol{k})\cdot\boldsymbol{r}} \tag{3.8}$$

where G rappresents the vectors which form the reciprocal lattice. The reciprocal lattice is generated by three primitive vectors $\boldsymbol{b_1}$,$\boldsymbol{b_2}$,$\boldsymbol{b_3}$, so that $\boldsymbol{a}_i \cdot \boldsymbol{b}_j = 2\pi\delta_{ij}$. Let us try to apply the wave plane formalism for the electronic density and for matrix elements of the Hamiltonian operator. For electronic density $n(\boldsymbol{r}) = \sum_k f_k \Psi_k^*(\boldsymbol{r})\Psi_k(\boldsymbol{r})$ we obtained

$$n(\boldsymbol{r}) = \sum_k \sum_{\boldsymbol{G'G}} f_k C^*_{\boldsymbol{G'},\boldsymbol{k}} C_{\boldsymbol{G},\boldsymbol{k}} e^{i(\boldsymbol{G}-\boldsymbol{G'})\boldsymbol{k}} = \sum_{\boldsymbol{G'G}} \boldsymbol{D}_{\boldsymbol{G'G}} e^{i(\boldsymbol{G}-\boldsymbol{G'})\boldsymbol{k}} \tag{3.9}$$

where we defined the *density matrix* as $\boldsymbol{D}_{\boldsymbol{G'G}} = \sum_k f_k C^*_{\boldsymbol{G'}} C_{\boldsymbol{G}}$. We can also defined the overlap matrix elements as

$$S_{\boldsymbol{GG'}} = \frac{1}{V_\omega} \int_\omega d\boldsymbol{r} e^{i(\boldsymbol{G}-\boldsymbol{G'})\boldsymbol{r}} = \delta_{\boldsymbol{GG'}} \tag{3.10}$$

The generic matrix elements of the Hamiltonian can be written in a plane wave rappresentations replacing $n(\boldsymbol{r})$ (equation 3.9) in (3.2) as (in atomic unit):

$$\begin{aligned}
E_{kin} &= \frac{1}{2} \sum_{\boldsymbol{GG'}} (\boldsymbol{k}+\boldsymbol{G})^2 C^*_{\boldsymbol{G'},\boldsymbol{k}} C_{\boldsymbol{G},\boldsymbol{k}} \delta_{\boldsymbol{GG'}} \\
E^{\nu} &= \frac{1}{V_{\omega_r}} \sum_{\boldsymbol{GG'}} C^*_{\boldsymbol{G'}} C_{\boldsymbol{G}} \int_\omega d\boldsymbol{r} e^{i(\boldsymbol{G}-\boldsymbol{G'})\cdot\boldsymbol{r}} \nu(\boldsymbol{r}) \\
E^{ee} &= \frac{1}{V^2_{\omega_r}} \sum_{\boldsymbol{GG'}} \sum_{\boldsymbol{G''G'''}} D_{\boldsymbol{GG'}} D_{\boldsymbol{G''G'''}} \int_\omega d\boldsymbol{r} d\boldsymbol{r'} e^{i(\boldsymbol{G}-\boldsymbol{G'})\cdot\boldsymbol{r}} e^{i(\boldsymbol{G''}-\boldsymbol{G'''})\cdot\boldsymbol{r'}} \\
E^{xc} &= \frac{1}{V_{\omega_r}} \sum_{\boldsymbol{GG'}} C^*_{\boldsymbol{G'}} C_{\boldsymbol{G}} \int_\omega d\boldsymbol{r} e^{i(\boldsymbol{G}-\boldsymbol{G'})\cdot\boldsymbol{r}} V_{xc}(\boldsymbol{r})
\end{aligned} \tag{3.11}$$

where we have written the matrix elements of the kinetic energy,external potential energy,electron-electron energy and exchange-correlation energy respectively. For each $\boldsymbol{k}$ value, the $\boldsymbol{G}$ index runs over plane wave, labeling the sites of the reciprocal lattice; the Fourier expansion is truncated usually within some cutoff in a way that for kinetic energy is

$$\frac{1}{2}||\boldsymbol{k}+\boldsymbol{G}||^2 \leq E_{pw} \tag{3.12}$$

In atomic unit, the energy is expressed usually in Rydberg or Hartree; common value for kinetic energy cutoff is 100-150 Ry but in general it is necessary testing the convergence for the system of interest.

Moreover, from equations (3.11), we note that the Kohn-Sham operator matrix elements are written like a Fourier sum over G reciprocal lattice,defined in a reciprocal space. In the Fourier rappresentation the electronic density is written

$$n(\boldsymbol{r}) = \sum_{\boldsymbol{G}} n(\boldsymbol{G}) e^{i\boldsymbol{G}\boldsymbol{r}} \tag{3.13}$$

with

$$n(\boldsymbol{G}) = \frac{1}{V_{\omega_r}} \int_{\omega_r} d\boldsymbol{r} n(\boldsymbol{r}) e^{-i\boldsymbol{G}\boldsymbol{r}} \tag{3.14}$$

the last expression is a common Fourier transform; The conversion from real space to reciprocal space and the calculation of the Fourier coefficients $n(\boldsymbol{G})$ is realized by the algorithm Fast Fourier Transform. In reciprocal space,the electronic density is calculated usually in the first Brioullin zone (IBZ) as

$$n(\boldsymbol{r}) = \frac{V_{\omega_r}}{(2\pi)^3} \sum_j \int_{\omega_k} d\boldsymbol{k} f_k \Psi^*_{kj}(\boldsymbol{r}) \Psi_{kj}(\boldsymbol{r}) \theta(E_F - \epsilon_{\boldsymbol{k},j}) \tag{3.15}$$

where $\theta(E_F - \epsilon_{\boldsymbol{k},j})$ is the characteristic function;in this way we have considered the electrons which occupy all the orbitals with energy $\epsilon_{\boldsymbol{k},j}$ up to the Fermi level and the summatory runs over the band index j.

In order to calculate the $n(\boldsymbol{r})$ we need to truncate the infinite sums up to a cutoff value (eq. 3.12) and perform the conversion $\int_{\omega_k} \rightarrow \sum_k$, sampling the reciprocal space by means of a regular grid or special k-points. In addition the number of plane waves is a discontinue function of the cutoff kinetic energy; changing cutoff value the number of plane wave changes suddenly. To remove this discontinuity smearing factor can be introduced.

$$\int_{\omega_k} \rightarrow \sum_k \omega_k \tag{3.16}$$

where $\sum_k \omega_k$ are the weight of the integration points. A possible choice to perform this sampling is use a regular grid like Monkhorost-Pack Grid, by means of which, the reicprocal lattice is sampled with rectangular grid of points of dimension M_x X M_y X M_z spaced evenly throughout the Brillouin zone;larger is the dimension of the grid, better and more accurate will be the sampling.

Previously, we have introduced two important amounts,the wave plane cutoff and the k-sampling grid, necessary to perform a DFT calculation in wave plane approximation; these values are needed an accurate convergence test on system of interest. For insulators usually only a small number of k-points is required to get good converged results.

We already said that a periodic system can be rappresented by a unit (or primitive) cell repeated periodically in all three spacial directions. To simulate this complicated system, we can use a single cell and apply the wave plane formalism with periodic boundary condition or build up a supercell generated by more than one single cell whose periodicy is defined by lattice vectors T (eq. 3.4); also in this case the periodic bound condition will be applied but the computational cost increses with dimesnion of the supercell. The volume of the reciprocal lattice V_{ω_k}=$\boldsymbol{b_1} \cdot (\boldsymbol{b_2}x\boldsymbol{b_3})$ is given by equation

$$V_{\omega_k} = \frac{(2\pi)^3}{V_{\omega_r}} \tag{3.17}$$

For large supercell, the volume of the Brioullin zone becomes smaller and it is enough low number of k-point to achieve the convergence. For very large value of the volume of the cristalline cell V_{ω_r} very small reciprocal lattice volume is obtained; for large supercell it is warrented use just one point to sampling the reciprocal space, usually the $\boldsymbol{k} = 0$ or Γ point. For metallic system is required to use a large k-sampling grid in order to describe accurately the Fermi surface.
We have already seen in (3.11), four contributions to the DFT total energy written on the planewave basis. Finally the matrix elements of the Kohn-Sham operator are rewritten in a Fourier rappresentation.
For the kinetic energy matrix elements T_{kin} are already diagonalized by plane wave basis

$$T_{kin} = \frac{1}{2}(\boldsymbol{k} + \boldsymbol{G})^2 \delta_{\boldsymbol{G}\boldsymbol{G}'} \tag{3.18}$$

From Poisson equation

$$\nabla^2 V_H(\boldsymbol{r}) = -4\pi n(\boldsymbol{n}) \tag{3.19}$$

the Hartree potential is obtained as

$$V_H(\boldsymbol{G}) = 4\pi \frac{n(\boldsymbol{G})}{||\boldsymbol{G}||^2} \tag{3.20}$$

For external potential

$$V_{ext}(\boldsymbol{G} - \boldsymbol{G}') = \frac{1}{V_{\omega_r}} \sum_{\boldsymbol{G}} V_{ext}(\boldsymbol{G}) \int_{\omega_r} d\boldsymbol{r} e^{i(\boldsymbol{G}-\boldsymbol{G}'-\boldsymbol{G}'')\cdot\boldsymbol{r}} = \frac{1}{V_{\omega_r}} V_{ext}(\boldsymbol{G} - \boldsymbol{G}') \tag{3.21}$$

and their relative energy contribution is

$$E^{\nu} = \frac{1}{V_{\omega_r}} \sum_{\boldsymbol{G}} V_{ext}(\boldsymbol{G}) n(\boldsymbol{G}) \tag{3.22}$$

The expectation value in Fourier space is calculated as sum over G-vectors of the product between electronic density and external potential.
Finally for exchange-corrrelation potential energy, by using the FFT, the density $n(\boldsymbol{G})$ (eq. 3.14) in Fourier space is calculated;here it is evalueted the exchange-correlation potential and by means another FFT algorithm back the results in the direct space.
In the next section the nucleo-core interaction is taken in account and we will see as the PW basis set does not allow to resolve the Kohn-Sham equation in PW rappresentation except if a very large number of plane wave is used.

3.2 The Norm-conserving pseudopotentials

In the previous section, the plane wave formalism of the single-particles Kohn-Sham equations was introduced and subsenquetly reported in the Fourier Space; we noted that in the Fourier space, they have a particularly simple form. The single-particles Kohn-Sham wave functions $|\Psi_k\rangle$ are all electron function, but no difference between core orbitals and valcence orbitals has been taken in account. Core orbital are strongly localized in an atomic region around the nucleus; due to the divergence of the electron-nucleus potential for distance $\boldsymbol{r} \rightarrow 0$, their behaviour results strongly oscillating (fig 2....). This perturbation requires high value of $\boldsymbol{G}$ - cutoff, with enormous incresed of the computational cost. In principle, also the valence orbital has a nodal structure, in order to be orthogonal to the core states;to achieve the nodeless valence wave function, it is assumed that the core electrons are frozen (*Frozen Core Approximation*) and replacing the ion-core potential by a Pseupotential. In the (*Frozen Core Approximation*) the spatial form of the core orbitals can be obtained from a single calculation performed on isolated atom, assuming that it remains the same in a crystal enviroment. The physical justification is that the core orbitals do not partecipate in chemical bonding.

Therefore, the set of wave functions, which are the variational solutions the Kohn-Sham equations, regard only the valence electrons;the core are not taken in accounts. In this way, the electrons in the valcence wave functions do not feel a bare ion-electron potential but rather a potential screened by core electrons. This potential is smoother and shallow than true one and the Kohn-Sham valence orbitals risulting are nodeless. The pseudpotential have to be built, *ad-hoc* for the system of interest (different for each element of the periodic table) and generally must be transferable. For example the pseudopotential for the iron elements, calculated on the isolated system, must be equally efficient for iron in mioglobine or iron in crystalline enviroment.

The constructions of a pseudopotential typically starts with the choice of an appropriate reference electronic configurations and the relative "pseudoization radii" so that for $r \leq r_c$ the oscillating part of the valcence wave functions is replaced by nodeless pseudofunction; usually the $r \leq r_c$ value is different for each l-channels (l is the angular orbital quantum number).

Actually the pseudopotential for ideal element is obtained starting from a generical smooth *pseudofunction* inverting the radial Schrodinger equations for isolated atoms to get the pseudopotential. From (in atomic unit)

$$[-\frac{1}{2}\frac{d^2}{dr^2} + \frac{l(l+1)}{2r^2} + V_{n,l}^{PS}(r)]rR_l^{PS} = \epsilon_l r R_l^{PS}$$

to

$$V_{n,l}^{PS}(r) = \epsilon_l - \frac{l(l+1)}{2r^2} + \frac{1}{2rR_l^{PS}(r)}\frac{d^2}{dr^2}[rR_l^{PS}] \tag{3.23}$$

where R_l^{PS} is the radial part of the pseudofunction $\psi^{PS}(\boldsymbol{r})$. General rules for pseudpotential and pseudofunction can be summarized in:

1) Pseudofunction must be nodeless

2) Norm conservation. The electronic charge (or the norm) of the pseudofunction (PS) within the pseudoization radius is the same of the charge of the all electron wave function (AE).

3) Pseudofunction matches the all-electron wave function beyond the cutoff radii

4) The Pseudopotential must be transferable. In order to achieve this properties, the eingenvalues of the relative pseudofunction must be the same over a range of rasonable reference configurations.

Not always these results can be achieved simultaneously and often they are in conflict. The Norm Conserving rule is that generally adopted for a long time. In this framework the relation reported below holds for all valence pseudofunctions.

$$\int_0^{r_c} drr^2|\psi_k^{PS}(\boldsymbol{r})|^2 = \int_0^{r_c} drr^2|\Psi_k^{AE}(\boldsymbol{r})|^2 \tag{3.24}$$

In addition, in order to assure a good trasferability of the pseudopotential, it is raccomandable that the slope of the pseudofunction is equals to the slope of the all electron wave function for $|\boldsymbol{r}| = |\boldsymbol{r_c}|$.Then

$$\frac{1}{\psi_k^{PS}(\boldsymbol{r},\epsilon)}\frac{d\psi_k^{PS}(\boldsymbol{r},\epsilon)}{d\boldsymbol{r}}|_{\boldsymbol{r}=\boldsymbol{r_c}} = \frac{1}{\Psi_k^{AE}(\boldsymbol{r},\epsilon)}\frac{d\Psi_k^{AE}(\boldsymbol{r},\epsilon)}{d\boldsymbol{r}}|_{\boldsymbol{r}=\boldsymbol{r_c}} \tag{3.25}$$

Equation 3.25 is the condition on the logarithmic derivatives. In (3.23) the Schrodinger equation is resolved in spherical simmetry, hence as a product of a radial equation and a spherical armonics. For fixed potential and energy ϵ_k, the radial differential equation is a one-dimensional ordinary linear second order equations with two indipendent solutions and inside and outside the sphere is uniquely defined.
In practice to obtain pseudoptential, the all-electron wave function Ψ_k^{AE} is rapleced,inside the sphere with $\boldsymbol{r} \leq \boldsymbol{r_c}$, by an arbitrary smooth nodeless function ψ_k^{PS} with same logarithmic derivative at r_c and for certain ϵ_k energy values, eigenvalue of the all electron wave function. The required pseudpotential is obtained by inserting ψ_k^{PS} and ϵ_k in radial Schrodinger equation and subsenquetly simply inverting it, so that to obtain V^{PS} which has the required properties.
The pseudopotential obtained inverting the radial Schrodinger equation is screened, which incorporates the Hartree and exchange-correlations terms relatively to the electronic density of the pseudofunction. To obtain the pseudopotential unscreened we substract the Hartree and the exchange-correlations contribution as reported below

$$V_l^{PS,unscr}(\boldsymbol{r}) = V_l^{PS,scr}(\boldsymbol{r}) - V_l^{PS,H}(\boldsymbol{r}) - V_l^{PS,XC}(\boldsymbol{r}) \tag{3.26}$$

Moreover the logarithmic derivative properties have to be reproduced for large value of energy ϵ_k, in this the reproducebility of the pseudofunction (and the pseudopotential) is assured for several different chemical enviroment. Furthmore to guarantee large trasferibility, the pseudoptential have to be as soft as possible and the number of plane wave to expand the pseudofunction have to be as small as possible. A large value of r_c generates a pseudopotential with better trasferibility properties; the same beahviour will be obtained if small cutoff value is used. These two conditions are in competition with each other and a good compromise must be achived.
For example a possible choice for pseudofunction R_l^{PS} in (3.23) is Troullier-Martins equation [18]

$$\begin{aligned} R_l^{PS} &= r^{l+1}e^{p(r)}r \leq r_c \\ R_l^{PS} &= R_l^{AE}r \geq r_c \end{aligned} \tag{3.27}$$

where

$$p(r) = c_0 + c_2r^2 + c4r^4 + c_6r^6 + c_8r^8 + c_10r^{10} + c_12r^{12} \tag{3.28}$$

Then, the norm conservation is imposed

$$\int_{r\leq r_c} dr(R_l^{PS}(r))^2 = \int_{r\leq r_c} dr(R_l^{AE}(r))^2$$

together to the continuity conditions of the wavefunction and its derivatives

$$R_l^{PS} = R_l^{AE} r = r_c$$

$$\frac{d^n R^{PS}(r_c)}{dr^n} = \frac{d^n R^{AE}(r_c)}{dr^n}$$

In principle the r_c and the pseudopotential depend on the angular momentum l, so for each l value different pseudopotentials have to be built. As a result of these scheme is a pseudpotential which can be written as:

$$V^{PS}(\boldsymbol{r}) = V^{loc}(\boldsymbol{r}) + \sum_{l=0}^{l_{max}} V_{n,l}^{PS}(\boldsymbol{r})\widehat{P}_l \tag{3.29}$$

and $\widehat{P}_l = |l\rangle\langle l|$ The local part of $V^{loc}(\boldsymbol{r})$ is taken as the compoent V_l^{PS} with maximum value of l and

$$V_{n,l}^{PS}(\boldsymbol{r}) = V_l^{PS}(\boldsymbol{r}) - V^{loc}(\boldsymbol{r}) \tag{3.30}$$

In this way once the full pseudpotential $V_n^{PS}, l(\boldsymbol{r})$ applies on wave function, each angular momentum component of wave function feels only the relative l-component of the $V_l^{PS}(\boldsymbol{r})$ potential. This type of pseudoptential is called semilocal pseudpotential.
In planewave rappresentation the semi-local part of the pseudopotential is written

$$\frac{1}{V_{\omega r}} \int d\boldsymbol{r} e^{-i(\boldsymbol{k}+\boldsymbol{G})} V_{n,l}^{PS}(\boldsymbol{r})\widehat{P}_l e^{i(\boldsymbol{k}+\boldsymbol{G'})} \tag{3.31}$$

The projection operator $\widehat{P}_l$ acts on $e^{i(\boldsymbol{k}+\boldsymbol{G'})}$ and can be written in terms of spherical armonics $Y_{l,m}$

$$\frac{1}{V_{\omega r}} \sum_{l,m} \int d\boldsymbol{r'} d\boldsymbol{r} e^{-i(\boldsymbol{k}+\boldsymbol{G})\cdot\boldsymbol{r}} Y_{l,m}(\boldsymbol{r}) Y_{l,m}^*(\boldsymbol{r'}) e^{i(\boldsymbol{k}+\boldsymbol{G'})\cdot\boldsymbol{r'}} V_{n,l}^{PS}(\boldsymbol{r}) \tag{3.32}$$

Let us consider the expansion

$$e^{i\boldsymbol{k}\cdot\boldsymbol{r}} = e^{ikrcos\theta} = 4\pi \sum_{l=0}^{\inf} \sum_{m=-l}^{+l} i^l j_l(kr) Y_{l,m}(\boldsymbol{r}) Y_{l,m}^*(\boldsymbol{k})$$

the normalization property of the spherical armonics

$$\int_0^{2\pi}\int_0^{\pi} d\phi d\theta |Y_{l,m}(\theta,\phi)|^2 = \delta_{l,l'}\delta_{m,m'}$$

and the *addition theorem* for spherical armonics

$$P_l(cos\theta) = \frac{4\pi}{(2l+1)} \sum_{m=-l}^{+l} Y_{l,m}(\boldsymbol{k}) Y_{l,m}^*(\boldsymbol{k'}) \tag{3.33}$$

where θ is the angle between $\boldsymbol{k}$ and $\boldsymbol{k'}$, j^l are spherical Bessel functions and P_l the Legendre polynomial. Then in spherical simmetry the integral (3.30) is written

$$\frac{4\pi}{V_{\omega r}}\sum_l P_l(cos\gamma)(2l+1)\int_0^{\inf} r^2 dr j_l(r|\boldsymbol{k}+\boldsymbol{G}|)j_l(r|\boldsymbol{k}+\boldsymbol{G'}|)V_{n,l}^{PS}(\boldsymbol{r}) \quad (3.34)$$

We see that the matrix elements depend on $|\boldsymbol{k}+\boldsymbol{G}|$ and $|\boldsymbol{k}+\boldsymbol{G'}|$ necessarely correlated with each other because the angle γ is that between the vectors $\boldsymbol{k}+\boldsymbol{G}$ and $\boldsymbol{k}+\boldsymbol{G'}$. Using a planewave basis with N elements, the number of matrix elements is N(N+1)/2, value which increases rapidely.

Kleinmann and Bylander [19] proposed an alternative approach, introducing a fully non-local pseudopotential in separable form:

$$V^{KB}(\boldsymbol{r}) = V^{loc} + \sum_{l,m}\frac{|V_l^{PS}\Psi_l^{PS}\rangle\langle\Psi_l^{PS}V_l^{PS}|}{\langle\Psi_l^{PS}|V_l^{PS}|\Psi_l^{PS}\rangle} = V^{loc} + V^{nloc} \quad (3.35)$$

and the equation written below

$$V_l^{nloc}|\Psi_l^{PS}\rangle = V_l^{PS}|\Psi_l^{PS}\rangle \quad (3.36)$$

holds. In Fourier space the non local part of the Kleinmann-Bylander (K-B) pseudopotentials is written

$$\sum_{GG'}\langle\boldsymbol{k}+\boldsymbol{G}|V_l^{nloc}|\boldsymbol{k}+\boldsymbol{G'}\rangle = \sum_{j=1}^{p}\sum_{GG'}\langle\boldsymbol{k}+\boldsymbol{G}|\alpha_j\rangle\,\nu_j\,\langle\alpha_j|\boldsymbol{k}+\boldsymbol{G'}\rangle \quad (3.37)$$

where $\nu_j = \frac{1}{\langle\Psi_l^{PS}|V_l^{PS}|\Psi_l^{PS}\rangle}$ and the summatory runs over the number p of projector $|V_l^{PS}\Psi_l^{PS}\rangle\langle\Psi_l^{PS}V_l^{PS}| = |\alpha_j\rangle\langle\alpha_j|$. In K-B scheme the computational efficiency increases and non-local potential requires only Np number of plane waves because the vectors $|\boldsymbol{k}+\boldsymbol{G}|$ and $|\boldsymbol{k}+\boldsymbol{G'}|$ can be treated separately, disappearing the dependence with angle γ.

Another approach to obtain a pseudopotential was introduced by David Vanderbilt who suggested to abandon (or relaxing) the norm-conservation condition. This relaxing leads the bloch states $\Psi_{\boldsymbol{k},j}$ will be not orthonormal anymore, complicating the formalism of Kohn-Sham equations. On the contrary, by using this approach, a large cutoff radii r_c is imposed (but the spheres with these radii centered on different atoms must not overlap anywhere) generating a pseudopotential which is much softer and hence much lower planewave basis set cutoff would be necessary; generally Ultrasoft pseudoptential is less transferable than norm conserving one.

3.3 Ultrasoft Pseudopotential

To introduce the Venderbilt pseudopotential (or Ultrasoft (USPP) pseudopotential) formalism [12], let us start to lebel the all electron wavefunction as $|\Psi_{\boldsymbol{k}}\rangle$ and $|\phi_{\boldsymbol{k}}\rangle$ will be the relative pseudofunction, so that:

$$\left[\widehat{T} + \widehat{V}^{eff}(\boldsymbol{r})\right]|\psi_k\rangle = \epsilon_k|\psi_k\rangle \quad (3.38)$$

$$\left[\widehat{T} + \widehat{V}^{loc}(\boldsymbol{r}) + \widehat{V}^{nloc}(\boldsymbol{r})\right] |\phi_{\boldsymbol{k}}\rangle = \epsilon_k^{PS} |\phi_{\boldsymbol{k}}\rangle \tag{3.39}$$

where $\widehat{V}^{eff}$ is the full all electron Kohn-Sham potential, k is a composite index where $k = \epsilon_k, l, m$, $\widehat{V}^{loc}(\boldsymbol{r})$ is a potential generated by using a special algorith which apparoach to V_{eff} beyond r_c. To define the $\widehat{V}^{nloc}(\boldsymbol{r})$ and we impose the norm conservation at $r = r_c$

$$\langle \phi_{\boldsymbol{k}} | \phi_{\boldsymbol{k}} \rangle = \langle \Psi_{\boldsymbol{k}} | \Psi_{\boldsymbol{k}} \rangle \tag{3.40}$$

and $\epsilon_k^{PS} = \epsilon_k$. Moreover, if we define the eigenstate $|\chi_{\boldsymbol{k}}\rangle$ as

$$|\chi_{\boldsymbol{k}}\rangle = \left[\epsilon_k - \widehat{T} - \widehat{V}^{loc}(\boldsymbol{r})\right] |\phi_{\boldsymbol{k}}\rangle \tag{3.41}$$

and

$$\widehat{V}^{nloc}(\boldsymbol{r}) |\phi_{\boldsymbol{k}}\rangle = |\chi_{\boldsymbol{k}}\rangle \tag{3.42}$$

hence the non-local part of the pseudopotential is

$$\widehat{V}^{nloc}(\boldsymbol{r}) = \frac{|\chi_{\boldsymbol{k}}\rangle \langle \chi_{\boldsymbol{k}}|}{\langle \chi_{\boldsymbol{k}} | \phi_{\boldsymbol{k}} \rangle} \tag{3.43}$$

We note some similarity between equation (3.42) and equation (3.35) where we introduced the Kleinmann and Bylander formalism.
Now let us generalize the condition (3.40) defining the *augmentation coefficients* Q_{kj} as

$$Q_{kj} = \langle \Psi_{\boldsymbol{k}} | \Psi_{\boldsymbol{j}} \rangle - \langle \phi_{\boldsymbol{k}} | \phi_{\boldsymbol{j}} \rangle \tag{3.44}$$

obviously if $Q_{kj} = 0$ norm-conservation condition is imposed. The norm-conservation condition (3.40) is defined inside the core region r_c (the same of the NCPP pseudopotential) but we will see that the component Q_{kj} is defined in a ragion which is larger that core region, with radius $R \geq r_c$.
Furthermore we define

$$B_{kj} = \langle \phi_k | \chi_j \rangle \tag{3.45}$$

and

$$\begin{aligned} |\beta_k\rangle &= \sum_j B_{jk}^{-1} |\chi_j\rangle \\ \langle \beta_k | &= \sum_j \langle \chi_j | B_{jk}^{-1} \end{aligned} \tag{3.46}$$

so that $\langle \beta_i | \phi_k \rangle = \delta_{ik}$ with $|\beta_i\rangle$ dual of the pseudofunction $|\phi_k\rangle$);in fact

$$\langle \beta_i | \phi_k \rangle = \sum_j B_{ij}^{-1} \langle \chi_j | \phi_k \rangle = \delta_{ik} \tag{3.47}$$

The non-local part of the pseudopotential can be chosen as

$$\widehat{V}^{nloc}(\boldsymbol{r}) = \sum_{mn} B_{mn} |\beta_m\rangle \langle \beta_n| \tag{3.48}$$

To demonstrate the previously equation is enough replace it into $\widehat{V}^{nloc}(\boldsymbol{r})$

$$\widehat{V}^{nloc}(\boldsymbol{r})\left|\phi_k\right\rangle = \sum_{mn} B_{mn}\left|\beta_m\right\rangle\left\langle\beta_n|\phi_k\right\rangle \tag{3.49}$$

then from (3.46) and (3.47) we obtain

$$\widehat{V}^{nloc}(\boldsymbol{r})\left|\phi_{\boldsymbol{k}}\right\rangle = \frac{\left|\chi_{\boldsymbol{k}}\right\rangle\left\langle\chi_{\boldsymbol{k}}|\phi_{\boldsymbol{k}}\right\rangle}{\left\langle\chi_{\boldsymbol{k}}|\phi_{\boldsymbol{k}}\right\rangle} = \left|\chi_{\boldsymbol{k}}\right\rangle$$

Now we introduce a crucial ***overlap*** function

$$\widehat{\boldsymbol{S}} = \widehat{\mathbf{1}} + \sum_{mn} Q_{mn}\left|\beta_m\right\rangle\left\langle\beta_n\right| \tag{3.50}$$

Starting from (3.47) It can demonstrate that

$$\langle\phi_i|\widehat{\boldsymbol{S}}|\phi_j\rangle = \langle\phi_i|\phi_j\rangle + Q_{ij} = \langle\Psi_{\boldsymbol{i}}|\Psi_{\boldsymbol{j}}\rangle \tag{3.51}$$

and from defintion (3.48) for non-local potential that

$$\left[\widehat{T} + V_{loc} + \big(\sum_{mn} B_{mn} + \epsilon_n Q_{nm}\big)\left|\beta_m\right\rangle\left\langle\beta_n\right|\right]\left|\boldsymbol{\phi_k}\right\rangle = \epsilon_{\boldsymbol{k}}\widehat{\boldsymbol{S}}\left|\boldsymbol{\phi_k}\right\rangle \tag{3.52}$$

Hence we have written the initial equation (3.39) in practice introducing the projectors $\left|\beta_m\right\rangle\left\langle\beta_n\right|$ and $\left|\chi_i\right\rangle\left\langle\chi_j\right|$. This equation have to be resolved for each k points (one Bloch state), generating a sequence of band with index n. Then the general Bloch eingestate $\left|\Phi_{\boldsymbol{k},n}\right\rangle$ resolves the equation $\left[\widehat{H} - \epsilon_{n,\boldsymbol{k}}\widehat{\boldsymbol{S}}\right]\left|\Phi_{\boldsymbol{k}}\right\rangle = 0$.
We can build and calculate the true electronic density from definition (3.44) replacing the general Bloch eingestate $\left|\phi_{\boldsymbol{k},n}\right\rangle$ by adding over $\boldsymbol{k}$ states occupied.

$$\rho(\boldsymbol{r}) = \sum_{n.\boldsymbol{k}} \phi_{\boldsymbol{k},n}{}^*(\boldsymbol{r})\phi_{\boldsymbol{k},n}(\boldsymbol{r}) + \sum_{ij}\rho_{ij}Q_{ij}(\boldsymbol{r}) \tag{3.53}$$

with $Q_{ij} = \sum_{n.\boldsymbol{k}}\left\langle\beta_i|\phi_{\boldsymbol{k},n}\right\rangle\left\langle\phi_{\boldsymbol{k},n}|\beta_j\right\rangle$. The electronic density is splitted in two component, one smooth calculated from pseudofunction $\phi_{\boldsymbol{k},n}$ and one defined inside the augmented region R. We have already reported some important features of Ultrasoft pseudopotential. Finally we would stress that for each chanel l the Ultrasfot pseudpotential approach allows to use more than one reference energy ϵ_n whilemean in norm-conserving semi-local approach this possibility was forbidden.

3.4 Gauge-including Projector Augmented Wave Pseudopotential

In chapter 2, we described the Projector Augmented Wave methods, a novel approach by means of which the Kohn-Sham problem is resolved in a pseudo Hilbert space $\widehat{\mathcal{H}}^{PS}$ span by smooth pseudofunction $|\tilde{\Psi}_k\rangle$ and subsenquetly the reconstruction of the all-electron $|\Psi_k\rangle$, $\widehat{\mathcal{T}}$, $|\Psi\rangle = \widehat{\mathcal{T}}\,|\tilde{\Psi}\rangle$ is performed by using the operator $\widehat{\mathcal{T}}$ defined as

$$\widehat{\mathcal{T}} = 1 + \sum_R \widehat{\mathcal{T}}_R \tag{3.54}$$

and

$$|\Psi_k\rangle = |\tilde{\Psi}_k\rangle + \sum_R \sum_j \left(|\phi_j^R\rangle - |\tilde{\phi}_j^R\rangle\right) \langle \tilde{p}_i^R|\tilde{\Psi}_k\rangle \tag{3.55}$$

with

$$\widehat{\mathcal{T}}_R = \sum_j \left(|\phi_j^R\rangle - |\tilde{\phi}_j^R\rangle\right) \langle \tilde{p}_j^R| \tag{3.56}$$

where all the lebels have already been defined in chapter 2. To perform this reconstruction the partial waves $|\phi_j^R\rangle$ and the projector $\langle \tilde{p}_j^R|$ are needed, defined inside the augmented region R. Without a complete demonstration, we can note as the US-PP method is strictly equivalent to the PAW method if in the augmentation function Q_{ij} with radius R the wave function $|\phi_k\rangle$ is replaced by pseudopotential partial waves $|\tilde{\phi}_k^R\rangle$ and the function all electron $|\Psi\rangle_k$ is replaced by all electron partial wave $|\phi_k^R\rangle$

$$Q_{kj} = \langle \phi_{\boldsymbol{k}}|\phi_{\boldsymbol{j}}\rangle - \langle \tilde{\phi}_{\boldsymbol{k}}|\tilde{\phi}_{\boldsymbol{j}}\rangle \tag{3.57}$$

In addition in (3.52) the projector $|\beta_i\rangle\langle\beta_j|$ is replaced by $|\tilde{p}_i\rangle\langle\tilde{p}_j|$ where $\langle\tilde{p}_i|$ are the usual projectors of the PAW method. Then in order to resolve the Kohn-Sham problem approaching with PAW method, the projector $\langle\tilde{p}_n|$ and the partial waves $|\phi_k^R\rangle$ and $|\tilde{\phi}_k^R\rangle$ must be calculated, either to obtain a SCF-converged Kohn-Sham valence wavefunction and to perform the all electron wavefunction reconstruction.
In presence of uniformal external magnetic field $\boldsymbol{B}$ [20], the all electron Hamiltonian is (in atomic unit)

$$\boldsymbol{H} = \frac{1}{2}\left[\boldsymbol{p} + \frac{1}{2}\boldsymbol{A}(\boldsymbol{r})\right]^2 + V(\boldsymbol{r}) \tag{3.58}$$

where c is the speed of light and $\boldsymbol{B}(\boldsymbol{r}) = \nabla \times \boldsymbol{A}(\boldsymbol{r})$. The choice of gauge that we make is set the gauge origin at the atomic site of the augmentation region. In this way we would obtain that $|\boldsymbol{A}(\boldsymbol{r})|^2$ experiences the minimum value and the interaction between the valence and core states is negligibly small. So the vector potential is chosen

$$\boldsymbol{A}(\boldsymbol{r}) = \frac{1}{2}\boldsymbol{B}(\boldsymbol{r}) \times \boldsymbol{r} \tag{3.59}$$

Here we do not discuss the PAW theory in presence of uniformal magnetic field, because is beyond of our scope[20]. Let's just say that in presence of uniform magnetic field, in order to preserve the translational invariance of the all electron wave function $|\Psi_k\rangle$, a modification of the operator $\widehat{\mathcal{T}}$ must be adding. Including the gauge properties, the new operator $\widehat{\mathcal{T}}$ translational-invariant is written

$$\widehat{\mathcal{T}} = \boldsymbol{1} + \sum_R \sum_j e^{(i/2c)\boldsymbol{r}\cdot\boldsymbol{R}\times\boldsymbol{B}} \left(|\phi_j^R\rangle - |\tilde{\phi}_j^R\rangle\right) \langle\tilde{p}_i^R|\, e^{-(i/2c)\boldsymbol{r}\cdot\boldsymbol{R}\times\boldsymbol{B}} \tag{3.60}$$

This transformation defines a more general PAW approach which we call *Gauge-including Progector Augmented Wave (GIPAW)* useful to calculate the XANES cross section and the chemical shift in a NMR experiment.

We are interesting to simulate the XANES cross section by using PAW method as reported at the end of chapter two. There,we introduced the formalism of the cross section σ_a in PAW framework, that we still reporting below

$$\sigma = 4\pi^2\alpha_0\hbar\omega\sum_f\left|\sum_j\langle\tilde{\Psi}_f|\tilde{p}_j^{R_0}\rangle\,\langle\phi_j^{R_0}|D|\Psi_i\rangle\right|^2\delta(E_f - E_i - \hbar\omega) \tag{3.61}$$

Now we are able to calculate the amounts required to perform the simulation of the XANES cross section. In summary we need

- The initial single-particles Kohn-Sham wave function $|\Psi_i\rangle$ from which the photoelectron is expelled. In general is known(1s or 2s atomic obital).
- The multielectron final wave function $|\tilde{\Psi}_f\rangle$ which describe the full electron final state of our system of interest. It is the converged Kohn-Sham wavefunction obtained after SCF-DFT procedure. To perform this calculation we use a plane wave pseudopotential approach, where the pseudopotential have to be GIPAW-like pseudopotential. Due to the equivalence between US-PP and PAW-PP approach, in practice we reduce to calculate the pseudo wavefunction $|\tilde{\Psi}_f\rangle$ with US-PP approach.
- The projectors already defined $|\tilde{p}_j^{R_0}\rangle$ and the partial waves $|\phi_j^{R_0}\rangle$ used to perform the reconstruction in (1.55), which are generated into the GIPAW pseudopotential.

Next section the building of the GIPAW pseudopotential for iron element is reported in order to perform XANES cross section simulation of the iron crystalline,myoglobine and cytochrome C.

3.5 GIPAW pseudopotential generation

Now we propose to build an Ultrasoft pseudopotential for Iron atom which contains the elements required to GIPAW reconstruction of the all electron wave function. As we can seen, we have to resolve the equation (3.52) for single isolated atom. As exchange-correlation functional we will use a gradient correction such PBE. Here we do not investigate this tipe of choice which remains an important step within of the PP generation procedure.
The starting atomic state (in our case the single-particles Kohn-Sham wave function for isolated atom) is defined by the electronic configuration for iron element. From periodic table, the electronic ground state of the Iron is

$$Fe = 1s^22s^22p^63s^23p^64s^23d^6 \tag{3.62}$$

From this configuration, we can note the valence orbitals are $4s^2$ and $3d^6$ whereas the core states are $1s^22s^22p^63s^23p^6$ because the atomic levels are completely filled up to the orbital $3p^6$ (end of third row of the periodic table). To improve the transferibility of the pseudopotential sometime is necessary promote the ns and nd states into valence. Physically can be correct because ns and np are localized in the same spatial region of the nd then they could be dependent to the chemical enviroment around the iron atom.
Now, if we put the orbital ns and np into core states, we could obtain a

pseduopotential with poor transferibility. Promoting ns and np in valence states (we speak of *semilocal states* for ns and np) together nd, $(n+1)s$ and, eventually, $(n+1)p$, we should improve the transferibility. For iron element the *semilocal states* are $3s^2$ and $3p^6$, whereas the pure valence state are $4s^2$ and $3d^6$. In general it is not necessary follow and impose the exact iron configuration as reported in (3.62). To generate the pseudopotential other configurations can be used,for example an ionic configuration where some electrons are removed. The orbital $4s^2$ loses two electrons and leads the metalic Fe^0 in ionic form Fe^{2+} whose electronic configuration is,

$$Fe^{2+} = 1s^2 2s^2 2p^6 3s^2 3p^6 4s^0 3d^6 \tag{3.63}$$

physically an chemically corrected.
In addition, in order to build a GIPAW pseudopotential with core-hole in 1s orbital, the electronic configuration will be

$$(Fe^{2+})^* = 1s^1 2s^2 2p^6 3s^2 3p^6 4s^0 3d^6 \tag{3.64}$$

The presence of the core-hole is necessary when we simulate XANES spectra, as already said in chapter one and two; the xanes cross section in a PAW framework contains the final wave function of the system, after interaction with photons; the photoelectron is ejected leaving a core-hole states in 1s or 2s orbital.
Once that the electronic configuration are imposed, we have to define the cutoff radius either for core region and for augmented region. Henceforth, we will consider identical the augmented region for Vanderbilt approach and PAW approach. Moreover the cutoff values are defined for each l-channel of the semi-core and valence states resulting from electronic configurations. In addition we add the valence orbitals 4P and 4D which are involved in the $1s \rightarrow P$ or $1s \rightarrow D$ transitions. The cutoff radius values are reported in table 3.1 below To obtain the pseudopotential for iron, the Martins-Troullier approach is choosen, whose algorithm is reported in (3.27) and (3.28).Then, the pseudization of the atomic waves is performed and the radial part of the Kohn-Sham equation is resolved in spherical symmetry for each l-channel and energy. More than one such atomic waves for different energy can be pseudized for the same l;in this case more than one projector per l-channel is resulted. This procedure is correct by definition for Ultrasoft pseudopotential;on the contrary for Norm- conserving PP, is necessary follow the Kleinmann-Bylander scheme, not implemented in Quantum Espresso. Finally,it is necessary to choose the local potential which appears in equation

nl	r_c	R_{aug}
3S	1.100	1.300
4S	0.800	1.300
3P	1.000	1.300
3D	1.400	1.800
4P	1.000	1.300
4D	1.400	1.800

Table 3.1: In table 3.1 cutoff radius for r_c and R_{aug} used to build GIPAW pseudopotential are reported (in Å)

(3.29). A good choice to set this value is taken the maximum value of the orbital angulare momentum, or with $l \geq l_c$, where l_c is the maximum value of the angular momenta for core states. In our case $l_{loc} = 2$.
For next steps, we propose to calculate total density of states (DOS) and band structures for iron crystalline (bcc lattice), checking the quality of the pseudopotential comparing it with a reference pseudopotential. Other check has been performed with experimental results and reported in figures below. The pseudopotential GIPAW (GIPAW-PP) generated is Utrasoft-like pseudopotential (US or USPP);on the contrary the reference pseudopotential is Norm-Conserving (NC or NCPP). Here we do not report how the converged wavefunction is calculated remanding this calculation to the next chapter. If reconstruction are not performed then we can speak equally of GIPAW-PP or US-PP pseduopotential calculation. In this section we perform just wavefunction optimizations, whereby the GIPAW-PP and US-PP notations are identical.
First of all, the lattice constant of the bcc lattice have be reproduced to verify the good quality of GIPAW pseudopotentials. Experimental value at 300 K is 2.87 Å. Below we reported total energy of the Fe bcc single unit cell in function of lattice parameter. The calculations reported in this section have been done using 150 Ry of cutoff kinetic energy, $10 \times 10 \times 10$ Monkhorost-Pack k-points mesh and PBE exchange-correlation functional on single bcc cell.

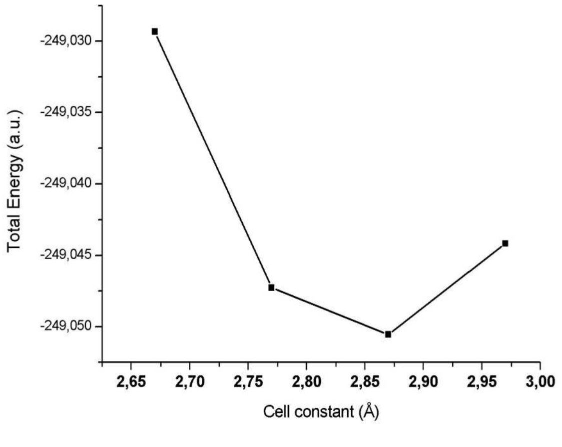

Figure 3.1: Total energy in function of lattice constant for iron unit cell in bcc symmetry was reported. The calculation was performed for pseudopotential without core-hole. It has been verified that the minimum of the curve is 2.87 Å

In figure 3.3 and 3.4 the total density of states (DOS) have been reported. DOS was calculated by this step:

- The single-particles Kohn-Sham wave functions were calculated by using GIPAW pseudopotential, setting the cutoff of the kinetic energy at 150 Ry and the lattice parameter at 2.87 Å; smearing Fermi-Dirac (FD) and Gaussian are used. The final density is converged by Self Consistent Field calculation after 18 (da verificare) scf-iterations

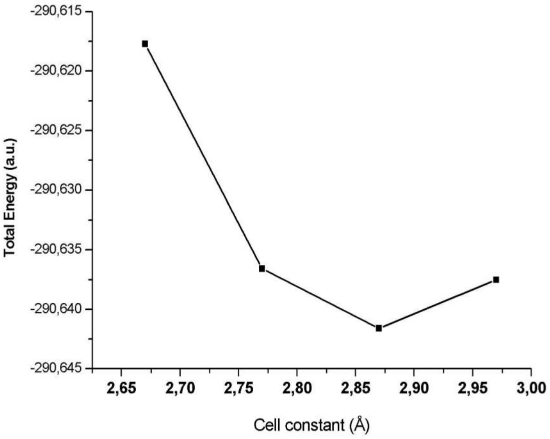

Figure 3.2: Total energy in function of lattice constant for iron unit cell in bcc symmetry was reported. The calculation was performed for pseudopotential with core-hole. It has been verified that the minimum of the curve is 2.87 Å

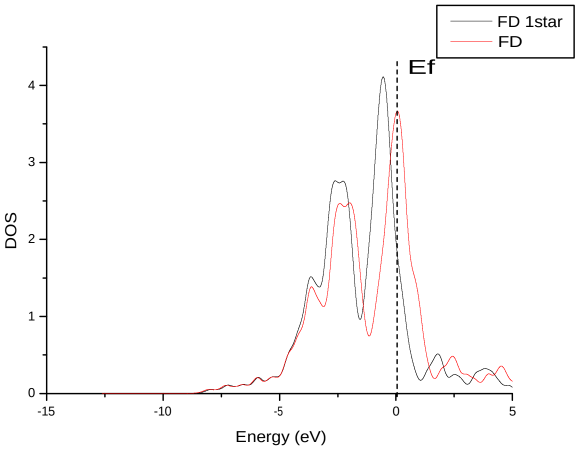

Figure 3.3: In this figure total density of states of iron crystalline are reported for pseudopotential USPP. The wavefunction was calculated using smearing Fermi-Dirac (FD) with value 0.05 Ry. The label 1star indicate the presence of core-hole and Ef is the Fermi energy

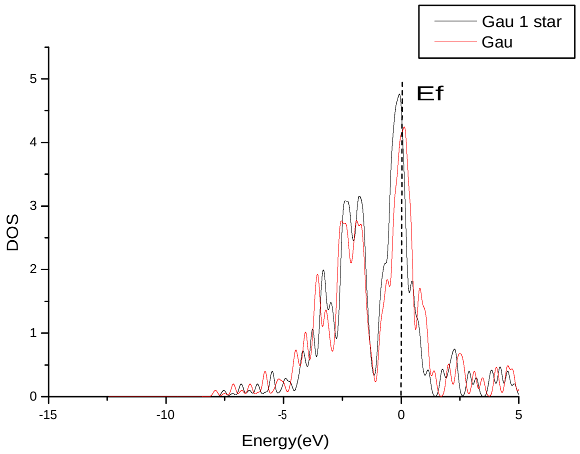

Figure 3.4: In this figure total density of states of iron crystalline are reported for pseudopotential USPP. The wavefunctions was calculated using smearing Gaussian (GAU) with value 0.001 Ry. The label 1star indicate the presence of core-hole and Ef is the Fermi energy

- DOS calculation extracted from wavefunction determinated by previous steps

Further informations and details about wavefunction calculations will be reported in chapter five. Density of states have been calculated either for pseudopotential within core-hole and without core-hole. In the last case, the Fermi energy seems to drop inside the band with greatest intesity;on the contrary, the DOS peak around the Fermi energy is contracted probably due to the screening effect of the core-hole. In addition, this behaviour increases for FD smearing, where the smearing value is set at 0.05 Ry, enormously greater than gaussian smearing one, set at 0.001 Ry. Same trend was found for traditional NCPP, where the agreement with GIPAW-PP is very high, how we can see in figure (3.4) and (3.5). In addition experimental DOS has been reported in figure (3.6) [21] in order to compare the experimental DOS and the DOS calculated in previous figures. Band structures of the iron in bcc symmetry are reported in the figures below for pseudo USPP (figure 3.7) and LSDA Norm Conserving pseudopotential approach from reference [22] (figure 3.8) Band structure was calculated using the special points at high symmetry of the FCC lattice H,Γ and P whose coordinates in $\frac{2\pi}{a}$ unit are

$$H = [-0.5; 0.5; 0.5]$$

$$\Gamma = [0; 0; 0]$$

$$P = [0.25, 0.25, 0.25] \tag{3.65}$$

with a lattice constant.
From these calculations, the agreement between USPP and NCPP approaches seems to be satisfactory,but to verify how XANES spectra are simulated, further

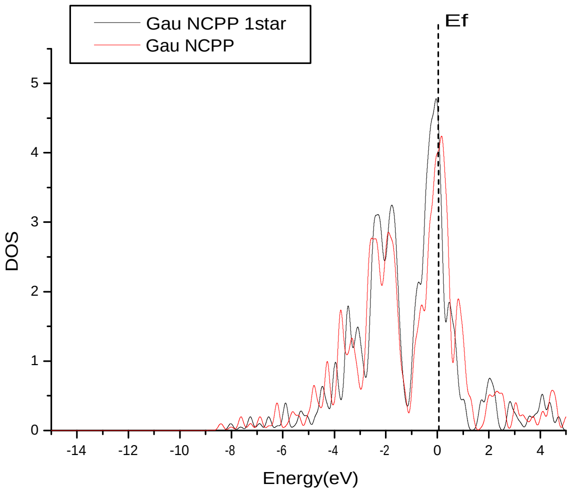

Figure 3.5: In this figure total density of states of iron crystalline are reported for pseudopotential NCPP. The wavefunctions was calculated using smearing Gaussian (GAU) with value 0.001 Ry. The label 1star indicates the presence of core-hole and Ef is the Fermi energy

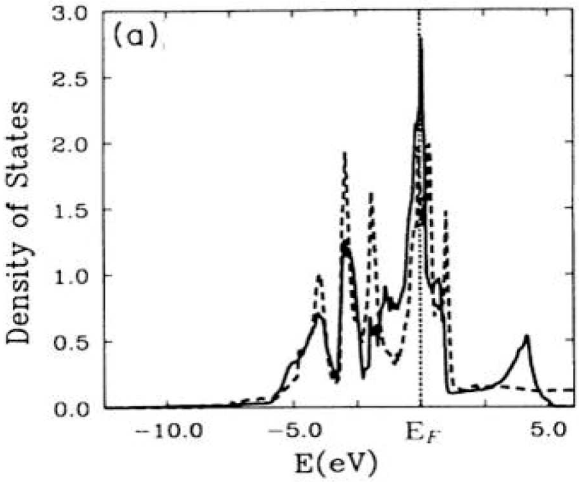

Figure 3.6: In this figure experimental total density of states of non-magnetic iron crystalline are reported for pseudopotentials from reference [21]

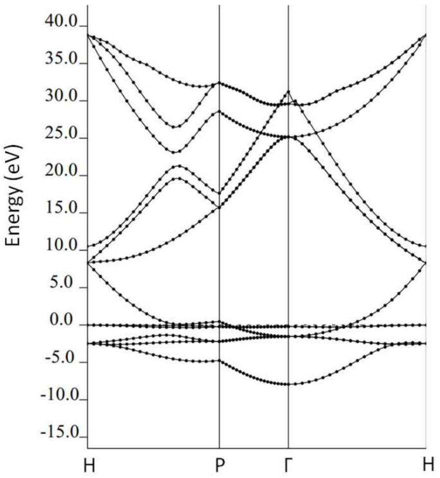

Figure 3.7: In this figure band structure for iron bcc is reported.This calculation was performed using USPP with core-hole and 0.001 Ry for gaussian smearing

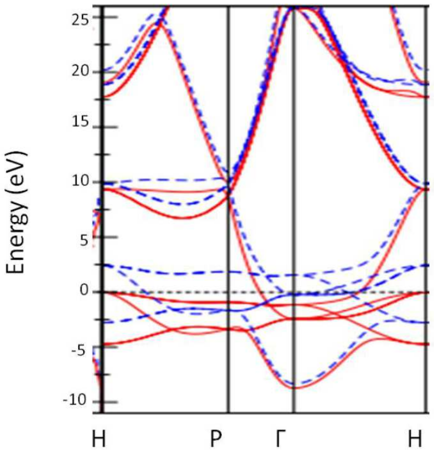

Figure 3.8: In this figure calculated band structure was reported, using Norm conserving pseudopotential and LSDA exchange-correlation funtional;more computational details can be obtain from reference [22]

investigations have been performed.Next chapter we will introduce formally the calculations of the XANES spectra using GIPAW pseudopotential approach.

Chapter 4

Determination of XANES spectra by using GIPAW-DFT approach

4.1 General aims

In the previous chapters we built a general scheme of calculation, inside the density functional theory framework, through which it is possible to calculate the all electron single-particle Kohn-Sham wave functions for many body system, starting from planewave pseudopotential approach. These functions are the wave functions all electrons, i.e. they do not suffer of further approximations. In practice, they are the real Kohn-Sham obitals which resolve the Kohn-Sham problem, inside of the Born-Oppheneimer approximation.
In order to obtain the XANES cross section for the system of interest, we need the wavefunction of the final states of the system, after the interaction with the X-ray photon.(equation 3.61).
In the past some authors have already performed ab inito calculations to generate the XANES cross section [14] [15] by using PAW and GIPAW approximation. The PAW methodology is currently implemented in the Quantum Espresso suite,an integrated suite of Open-Source computer codes for electronic-structure calculations and materials modeling at the nanoscale, based on Density functional theory, planewave and pseudopotentials[23]. To obtain XANES spectra, the *XSpectra* module of Quantum Espresso has been used together the planewave module (*PWscf*), necessary to perform the self consistent field algorithm.
Roughly speaking, the steps necessary to calculate the XANES cross section are:

- Determination of the best structural parameters for the system target. For the test cases we have considered, namely iron and silicon, it is enough to verify the best lattice parameter for cubic unit cell. Different scf calculation with pseudopotential are performed for different lattice parameter values, obtaining a curve total energy in function of the lattice constant. The point corresponding to the minimum of the curve is the best theoretical value of the lattice costant for the cubic cell. In this step planewave module of Quantum espresso was used

- Determination of the scf-converged final wavefunction $|\Psi_f\rangle$ of the system of interest after interaction with x-ray photon, calculated for the best lattice costant. This is the pseudoelectron Kohn-Sham wave function obtained using traditional USPP or NCPP calculations.The pseudopotential have to contain the informations to perform the GIPAW reconstruction. Generally the core-hole approximation have to be taken in account.As well in this case, the only planewave module of quantum espresso was used.

- *XSpectra* calculations to generate XANES spectra. The parameters used in *XSpectra* will be showed for each case of interest. Usually, the calculation of XANES spectra required to fix the coordinates of polarization vector $\widehat{\boldsymbol{episolon}}$ and $\boldsymbol{k}$ vector. For each system material of interest, these values are set in function of the simmetry class of the unit cell. For C1 puntual group and in general for system without any particular symmetry, in oder to generate XANES spectra it is possibile apply the scheme reported in (1.4).

From numerical point of view we perform the calculation of the XANES cross section in (3.62) by using a recursive method. As reported in [15], this approach permits to write the cross section as a continued fraction and only the occupied Kohn-Sham states have to be calculated. In chapter 2, we showed the expression of the cross section using Green function. In fact the cross section

$$\sigma_a = 4\pi^2\alpha\hbar\omega\sum_f\left|\sum_j\langle\tilde{\Psi}_f|\tilde{p}_j^{R_0}\rangle\,\langle\phi_j^{R_0}|D|\Psi_i\rangle\right|^2\delta(E_f - E_i - \hbar\omega) \tag{4.1}$$

by making the substitution (already reported in (1.40)), can be rewritten

$$-\frac{1}{\pi}Im\tilde{G}(\boldsymbol{r},\boldsymbol{r}',E) = \sum_f|\tilde{\Psi}_f\rangle\,\delta(E_f - E_i - \hbar\omega)\,\langle\tilde{\Psi}_f| \tag{4.2}$$

and $\tilde{G}(\boldsymbol{r},\boldsymbol{r}',E)$ is $\tilde{G}(\boldsymbol{r},\boldsymbol{r}',E) = (E - \tilde{\mathcal{H}} + i\gamma)^{-1}$ and with $\tilde{\mathcal{H}} = \mathcal{T}^{+}\mathcal{H}\mathcal{T}$. The Lanczos recursive method is used to calculate the eigenvalues of square matrix N×N starting from reduced tridiagonal form of the intial matrix. In our case the initial matrix is $\tilde{G}(\boldsymbol{r},\boldsymbol{r}',E)$ and the pseudo-hamiltonian $\tilde{\mathcal{H}}$. The tridiagonal form is obtained making a change of basis. Let us try to rewrite σ_a as,

$$|\tilde{\psi}^{R_0}\rangle = \sum_j|\tilde{p}_j^{R_0}\rangle\,\langle\phi_j^{R_0}|D|\Psi_i\rangle \tag{4.3}$$

where the index j runs over number of projectors. And

$$\sigma_a = 4\pi^2\alpha\hbar\omega Im[\langle\tilde{\phi}_j^{R_0}|(E - \tilde{\mathcal{H}} - i\gamma)|\tilde{\phi}_j^{R_0}\rangle] \tag{4.4}$$

The change of basis in the $\{|u_i\rangle\}$ vectors is achieved by means the following transformation

$$\tilde{\boldsymbol{H}}\,|u_i\rangle = a_i\,|u_i\rangle + b_{i+1}\,|u_{i+1}\rangle + b_i\,|u_{i-1}\rangle \tag{4.5}$$

where $\{|u_0\rangle\}$ is the normalized intial vectors $|u_0\rangle = \frac{|\tilde{\psi}^{R_0}\rangle}{\langle\tilde{\psi}^{R_0}|\tilde{\psi}^{R_0}\rangle}$. The vectors a_i and b_i are determinated as $a_i = \langle u_i|\tilde{\boldsymbol{H}}|u_i\rangle$ and $b_i = \langle u_i|\tilde{\boldsymbol{H}}|u_{i-1}\rangle$.

The number of Lanczos iterations N necessary to achieve the convergence must not exceed the dimension of the pseudo-Hilbert space $\tilde{\mathcal{H}}$, span by $|\tilde{\Psi}\rangle$ pseudo wave functions. This dimension is set by planewave cutoff of the kinetic energy. All the wavefunction optimization procedures (or single point SCF procedure) was done with pseudopotential approach as already described in the previous chapters, both NCPP and USPP; for exchange-correlation part, the PBE functional will ever be used.

In the sections below we will describe the procedure applied to the K-edge cross section for Fe-bcc and d-silicon (silicon in diamond symmetry);as nontrivial applications to material of biological interest this procedure is also applied to myoglobin and cytochrome c.

4.2 Application to the K edge in Iron with body cubic centered symmetry

The first application described in this section regards the theoretical investigation of the fine structure near K edge of the Fe-bcc (iron with body cubic centered symmetry).

Iron is one of the most important metals, subject of exstensive experimental and theoretical investigation for many years. Its particular properties make it one of the systems target for electronic structure calculations. Usually iron crystallizes in a periodic structure whose unit cell is in body cubic centered (bcc) symmetry but at least another symmetry, the face centered cubic shape, can be found. Some of these calculations suggest wrongly the fcc to be more stable than bcc symmetry [21]. The fcc unit cell will not be taken in account, considering the iron just in bcc symmetry.

The *PWscf* module of Quantum Espresso suite was used to determine the lattice constant for cubic cell of the Fe-bcc; for fixed value of the lattice parameter, a full self consistent field (SCF) wavefunction optimization is performed. The most important parameters needed in PWscf module are

- Cell Symmetry
- number of atoms in the unit cell
- Kinetic energy cutoff
- occupation smearing
- scf convergence threshold
- atomic species and atomic positions in the unit cell
- K point mesh
- number of bands

The initial calculations were performed using single unit cell (two atoms for cell), 150 Ry for kinetic energy cutoff, and 10×10×10 Monkhorost-Pack k-points grid. In metallic systems, 0.001 Ry of guassian spreading is an acceptable value and for number of occupied bands usually is chosen half of number electrons in the unit cell with adding 20% or greater.

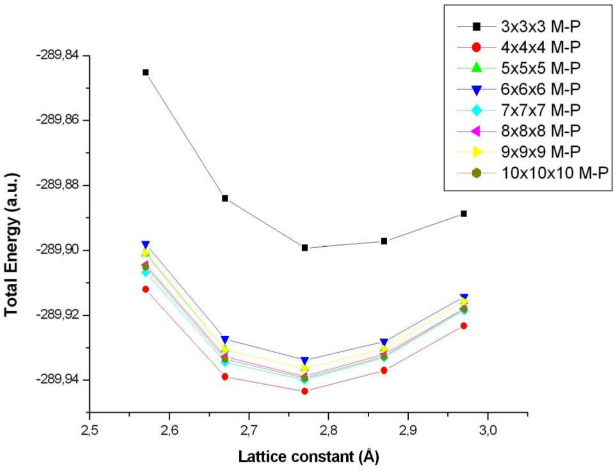

Figure 4.1: Plot of the total energy in function of the lattice constant.The minimum is found for 2.77 Å. Each curve corresponds to the Monkhorost-Pack k-points mesh (q×q×q)

In the next figure (4.1), we report the calculations to obtain the best cell parameter by using Norm-Conserving pseudopotential, generated by Quantum Espresso authors with core-hole approximation. In addition convergence study of the Monkhorost-Pack k-points grid is reported (fig 4.2). From figures (4.1), 2.77 Å is the value corrisponding to the minimum of the total energy. Calculated value of the lattice constant was found 2.76 Å[21]. From experimental point of view the lattice constant is 2.87 Åat 300 K. Using a greater smearing value with Fermi-Dirac profile, we obtained 2.87 Å as minimum value for lattice constant(fig 4.3). Subsequently, the *XSpetcra* module of Quantum Espresso has been used;we reported the most important parameters used in *XSpetcra* to obtain the K-edge spectra for Fe-bcc single cell in dipolar approximation.

- Type of approximation:dipolar or quadrupolar
- number of iterations of the Lanczos procedure
- Convergence threshold to finish the Lanczos iterations
- Fermi energy
- Coordinates of the polarization vector of the incident beam
- Coordinates of the $\boldsymbol{k}$ vector of the incident wave
- K point mesh to perform the electronic integration in the Lanczos iterations
- Core-hole linewidth (from atomic data)
- Energy range for plotting the xanes spectra

In dipolar approximation the transition matrix (see chapter 1,section 4) is not dependent by $\boldsymbol{k}$ vector. In addition the polarization vector and the $\boldsymbol{k}$ vector must

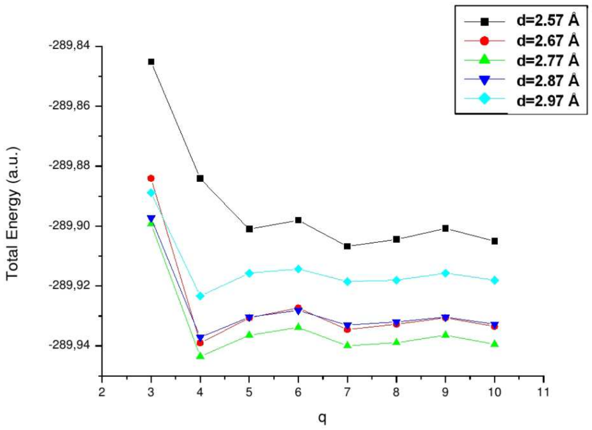

Figure 4.2: Plot of the single point SCF total energy in function of the Monkhorost-Pack k-point mesh (q×q×q) for each lattice constant values

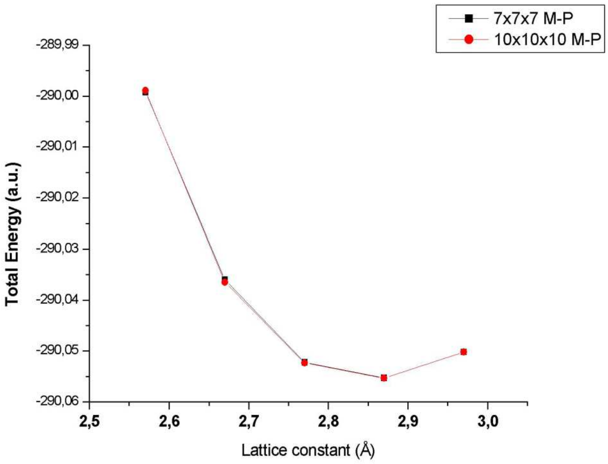

Figure 4.3: Plot of the single point SCF total energy in function of the lattice constant for Fermi-Dirac smearing (0.05 Ry).

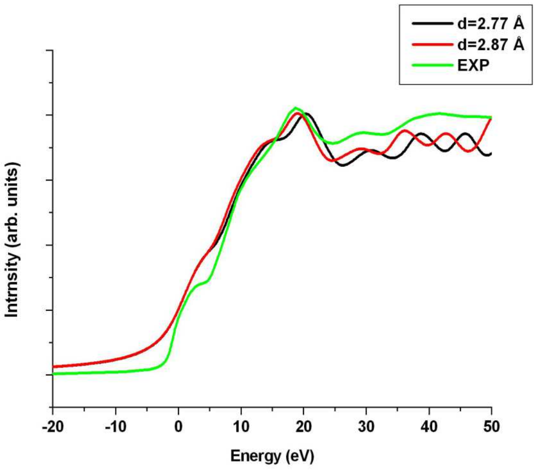

Figure 4.4: Plot of the xanes spectra for Fe-bcc with lattice costant d=2.77 Å(in black) and d=2.87 Å(in red), comparing with experimental curve (in green)

be orthogonal; then we need to set only the coordinates of $\hat{\epsilon}$ considering that for cubic cell, and in particular for point group O_h, the absorption cross section is indipendent of the position of the polarization vector. Convergence threshold is set at 0.001 eV and usually we used a 7×7×7 grid for electronic integration in Lanczos procedure; for this grid there are 7×7×7=343 k-points and for each k-point XSpectra performs the Lanczos iterations. The computational cost for single Fe-bcc unit cell is rather low, and not appreciable increase of that is detected for different parameters. For larger system, it could be necessary change these values in order do not increase the computational costs. In figure (4.4) and (4.5) Fe-bcc XANES spectra are reported, using the optimized wavefunction for the final states in the cross section, calculated previously, comparing the XANES spectra for different lattice constant. In order to appreciate the agreement between experimental and calculated spectra,the intensity of the curves are normalized by aligning the intensity of the corresponding highest peaks. For Fe-bcc single cell the agreement with experimental plot is rather low and we can note as the dependence with lattice constant is very pronounced. Certainly the spectra calculated for lattice constants reported in fig 4.4 has a better agreement with experimental result respect the curve in figure (4.5). For d=2.87Å the only agreement is for the first peak around 14 eV. In summary, we reported in table 4.1 the essential parameters used to obtain the XANES spectra for single Fe-bcc cell. However some precoutions must be taken in account to improve the calculated XANES spectra. First, it is necessary give up the single cell structure for Fe-bcc and build up a supercell system, to minimize the interaction between core-hole and its your periodic image (fig 4.6 and 4.7). In figure 4.8 we reported a 2D-plot of the electronic density for 2x2x2 supercell In a 2×2×2 supercell the distance between two core-hole is twice of the lattice constant, corresponding to the weaker interaction respect to single cell. In fact for Fe-bcc symmetry the primitve supercell contains 8 atoms and only one of these eight atoms suffers an interaction with x-ray photon. This last atom will be describe by using the pseudopotential generated with core-hole (and GIPAW

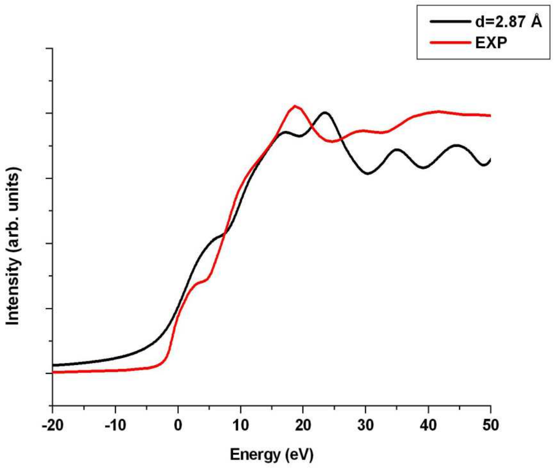

Figure 4.5: Plot of the xanes spectra for Fe-bcc with lattice costant d=2.57 Å(in black) comparing with experimental curve (in red).

Lattice constant (Å)	2.57	2.77	2.87
Planewave cutoff (Ry)	150	150	150
Approximation	dipolar	dipolar	dipolar
Coordinates $\hat{\boldsymbol{\epsilon}}$ vector	1 0 0	1 0 0	1 0 0
Coordinates $\boldsymbol{k}$ vector	0 0 1	0 0 1	0 0 1
Monkhorost-Pack k-points	10×10×10	10×10×10	10×10×10
Electronic integration grid	7×7×7	7×7×7	7×7×7
Thres. conv. (eV)	0.001	0.001	0.001
Max numb. iter.	1000	1000	1000
c-h linewidth(eV)	3	3	3
Energy range (eV)	[-20;50]	[-20;50]	[-20;50]

Table 4.1: In table 4.1 the most important parameter for *XSpectra* module are reported.Lattice parameters used are 2.57 Å, 2.77 Åand 2.87 Å. The vectors $\hat{\epsilon}$ and $\boldsymbol{k}$ are reported in crystal coordinates,i.e. in relative coordinates of the primitive lattice vectors.

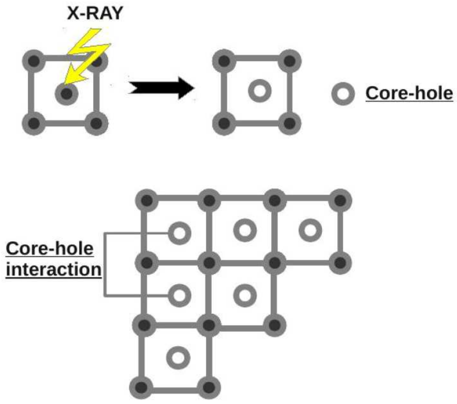

Figure 4.6: In figure a 2D picture of Fe-bcc single cell and his periodic images are reported.Distance between two core-hole is equal to the lattice constant for the bcc symmetry.

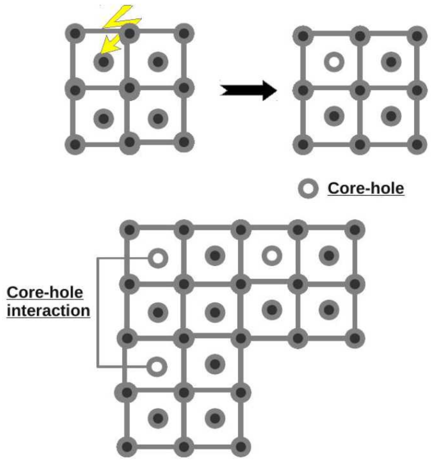

Figure 4.7: In this figure a 2D picture of 2x2x2 Fe-bcc supercell is reported together his periodic images.Distance between two core-hole is twice to the lattice constant for the bcc symmetry.

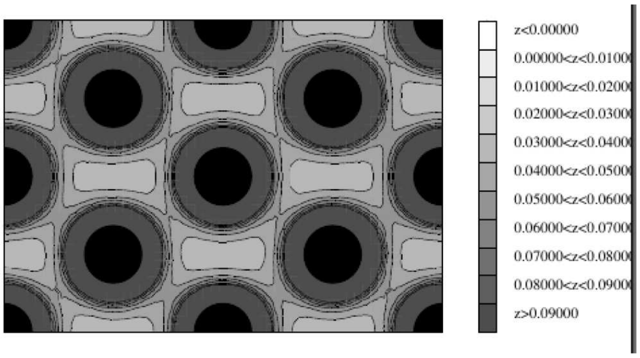

Figure 4.8: In this figure the 2D-plot of the electronic density for Fe-bcc 2x2x2 supercell is reported.The value of magnitude corrisponding to each gray scale is reported on the right of the figure

Planewave cutoff (Ry)	150
Approximation	dipolar
Coordinates of $\hat{\epsilon}$ vector	1 0 0
Coordinates of $\boldsymbol{k}$ vector	0 0 1
Monkhorost-Pack k-points	10×10×10
Electronic integration grid	7×7×7
Thres. conv.	0.001 eV
Max numb. iter.	1000
c-h linewidth (eV)	2
Energy range	[-20;50]

Table 4.2: In table 4.2 the most important parameter for *XSpectra* module used to obtain the spectra in figure (4.11) are quoted

reconstruction), whereas the other seven atoms will be described by tradition NCPP (or USPP) pseudopotential.
In the next figure (4.9) the lattice parameter for Fe supercell 2×2×2 is calculated. As already found for single cell, the minimum is achieved for 2.77 Å using a smearing gaussian (0.001 Ry). At 300 K the experimental value is 2.87 Å which is achieved by using a Fermi-Dirac smearing electronic occupation with 0.05 Ry for broadening (figure 4.10). Using 2.87 Å as value of the lattice constant and parameters in table (4.2), calculated spectra for 2×2×2 supercell with Norm-Conserving pseudopotential is reported in the figure (4.11). In our opinion, it is important to stress the improvent obtained for the theoretical spectra using a supercell respect to the Fe-bcc single cell. All the peak positions seem to be are well reproduced (except the pre-edge region of the spectrum). Some differences have been encoutered regarding the peaks intesity, where an accetable convergence between caluclated and experimental profile is not yet obtained, in particular at high energy values (upper 20 eV). Moreover, in the previous chapter, we built an Ultrasoft pseudopotential for iron element with GIPAW reconstruction, by means of which different electronic density properties and structural parameters of the Fe-bcc was calculated (total DOS and band structure). By using this tested pseudopotential, we perform the XANES calculation applying the scheme

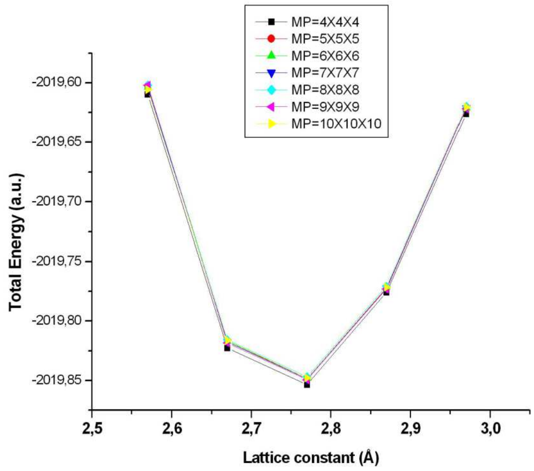

Figure 4.9: As for single Fe-bcc cell, the minimum of the total energy of the supercell 2×2×2 is found at 2.77 Å.Each curve corresponds to the Monkhorost-Pach K-points grid q×q×q

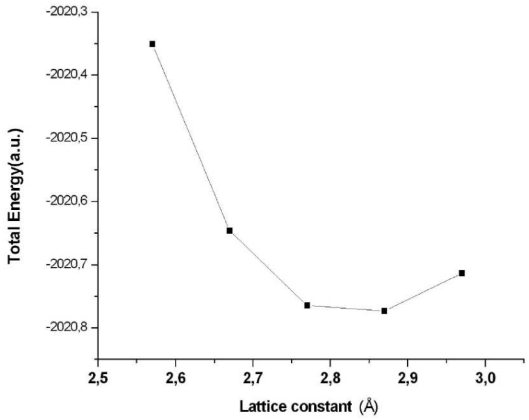

Figure 4.10: By using Fermi-Dirac spreading the minimum of the total energy of the supercell 2×2×2 is found at 2.87 Å.The K-points grid used is 10×10×10

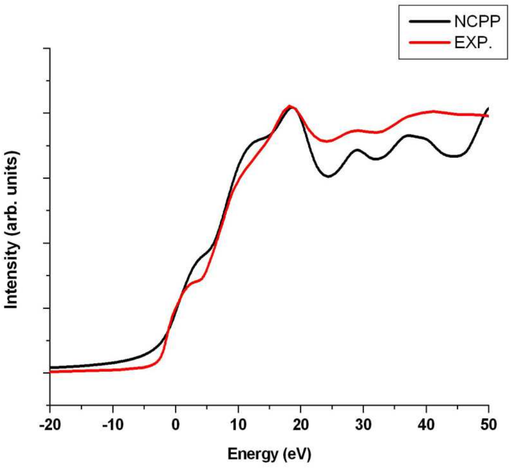

Figure 4.11: In this figure the XANES spectra for Fe-bcc 2x2x2 supercell is reported.The linewidth of the core-hole is set at 2eV

as already seen for Norm-Conserving. In *XSpectra* it will be used the parameters in table 4.2.
In the next figures we compare the Ultrasoft XANES cross section with experimental data, for linewidth of the core-hole fixed at 2 eV (figre 4.12) and 3 eV (figure 4.13). The curves seem to be in good agreement with experimental

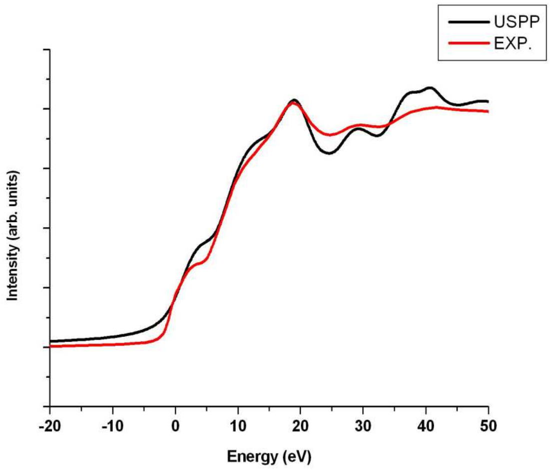

Figure 4.12: In this figure the XANES spectra for Fe-bcc 2x2x2 supercell is reported by using USPP pseudopotential.The linewidth of the core-hole is set at 2 eV

data, in particular at low energy values. In next figures with compare the USPP with NCPP approach Finally we note as both Norm-Conserving and Ultrasoft approach work in good agreement with experimental data. The former was generated by Quantum Espresso authors whereas the latter is generated by us. The Ultrasoft approach allows to use more than one l-channel in the valence

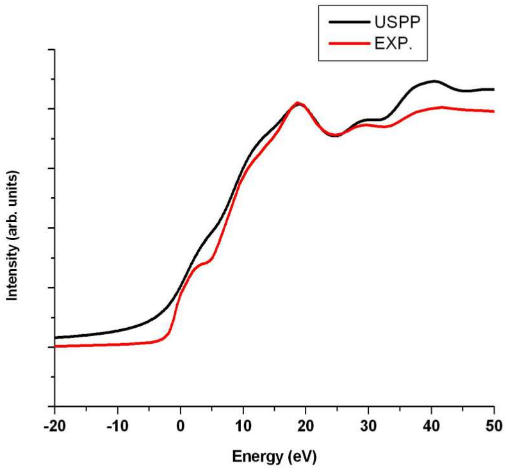

Figure 4.13: In this figure the XANES spectra for Fe-bcc 2x2x2 supercell by using USPP pseudopotential is reported.The linewidth of the core-hole is set at 3 eV

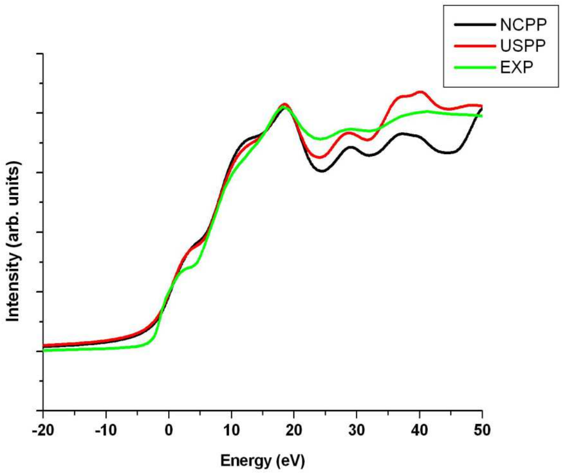

Figure 4.14: Calculated XANES spectra for Fe-bcc 2x2x2 supercell with USPP (in red)and NCPP (in black colour) approach are compared in this figure.The linewidth of the core-hole is set at 2 eV.It is also reported the experimental curve

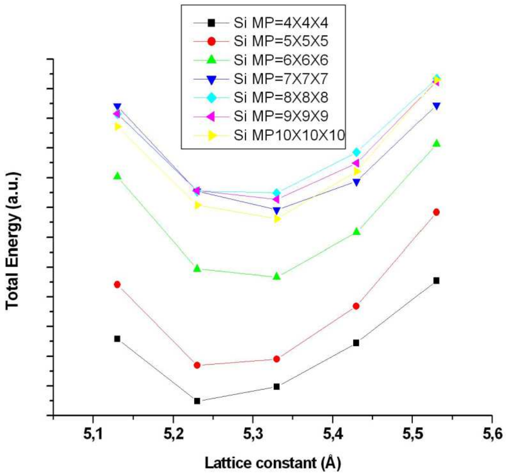

Figure 4.15: Plot of the total energy in function of the lattice costant is reported for different Monkhorost-Pack kpoints grid (M-P q×q×q)

configuration; then we can put the 3s and 4s orbitals as valence orbitals, more similar to his ground state. For norm-conserving scheme just the 3s orbital have been included in the valence configuration.

4.3 Application to the K edge in Silicon

Furthermore, another application was performed on the silicon crystalline structure. Silicon, like carbon and germanium, crystallizes in a diamond cubic crystal structure, with a lattice spacing of 5.43 Å. For silicon, we used a similar scheme already used for the Fe-bcc.First we determined the lattice costant for single cell with diamond symmetry, building up the curve total energy in function of lattice constant for different values of the latter one (fig. 4.15). For all the calculations reported in this section, we used an Ultrasoft approach. For low grid values, we obtained lattice constants which are far from experimental value, 5.23 Åup to a 4×4×4 mesh. Lattice constant values near to experimental data (5.43 Å) is achieved for finer grid. The k-points convergence of the charge density was obtained with good accuracy for k-points grid greater than 7×7×7(fig. 4.16). Moreover for d=5.33 Åand d=5.43 Åwe added further mesh values up to q=15 to assure completely the convergence of the charge density. All these values are obtained using a pseudo Ultrasoft with core-hole effect. This effect produces a lattice cell distorsion and the best value of the lattice constant is reached for 5.33 Å. By performing a wavefunction optimization with pseudopotential without core-hole, we want demonstrate that cell distorsion is mainly due to the core-hole interaction. In fact, for the same values of the lattice constant used in the previous calculation (fig 4.18), the best calculated lattice parameter value is 5.42 Å. Moreover, for lattice constant set at 5.33 Å and 5.43 Å we performed the XANES simulation (fig 4.19, 4.20) using the parameters reported in table (4.3). From figures 4.19 and 4.20 the calculated spectra for silicon single cell does not seem to be in strong agreement with experimental data;maybe only the

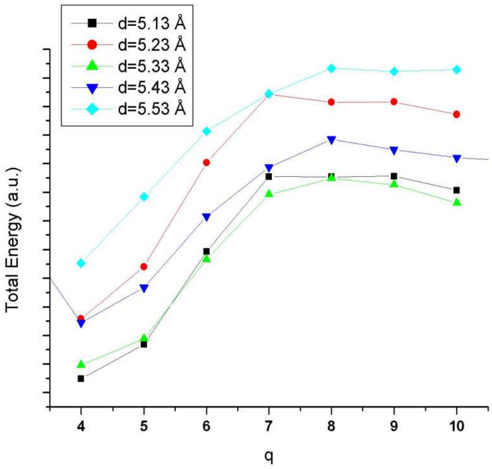

Figure 4.16: In this figure we can see the convergence of the electronic density for k-points grid higher than 7×7×7

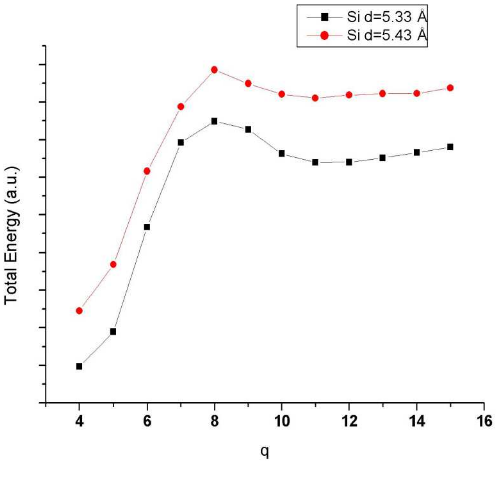

Figure 4.17: In this figure we can see the convergence of the electronic density for k-points grid up to 15×15×15

(fig. 4.17)

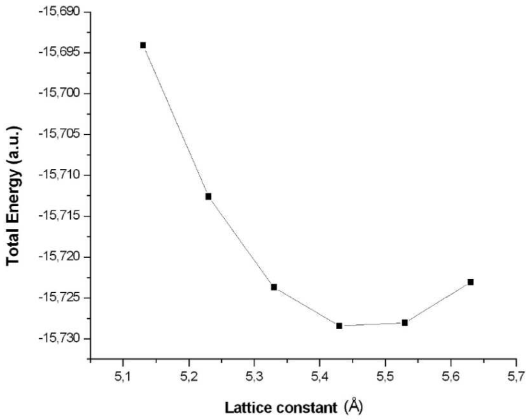

Figure 4.18: In this figure it is reported the plot total energy in function of lattice constant, showing that the best lattice value is 5.43 Å,calculated by pseudoptential without core-hole

Lattice parameter (Å)	5.33	5.43
Planewave cutoff (Ry)	150	150
Monkhorost-Pack k-points	10×10×10	10×10×10
Electronic integration grid	7×7×7	7×7×7
Coordinates of $\hat{\boldsymbol{\epsilon}}$ vector	1 0 0	1 0 0
Coordinates of $\boldsymbol{k}$ vector	0 0 1	0 0 1
Thres. conv. (eV)	0.001	0.001
Max numb. iter.	1000	1000
c-h linewidth (eV)	1;2;3	1;2;3
Energy range	[-20;50]	[-20;50]

Table 4.3: In table 4.3 the most important parameter for *XSpectra* module are reported used to obtain the spectra in figures (4.19) and (4.20)

first peak around 5 eV is slightly reproduced, but with very low intensity.

As already seen for the Fe-bcc, we have to decrease the core-hole effect introducing a supercell so that the distance between core-hole in subsequent image of the supercell increases. We built a supercell 2×2×2 which is enough to reduce this interaction;in fact from figure (4.21), we note that the minimum of the curve total energy in function of lattice constant is found again at 5.43 Å.

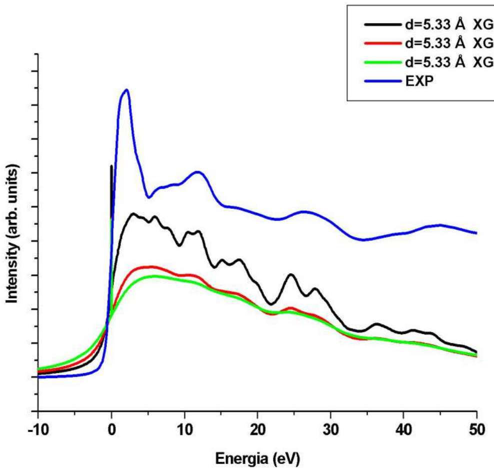

Figure 4.19: Simulated XANES spectra of silicon with diamond single cell (d=5.33 Å) for different values of core-hole line width (labeled XG in figure) and comparing with experimental spectra

Subsequently, we generate the spectra for supercell 2×2×2 (fig 4.23). We note that the calculated spectra for silicon supercell is improved and the first peak is

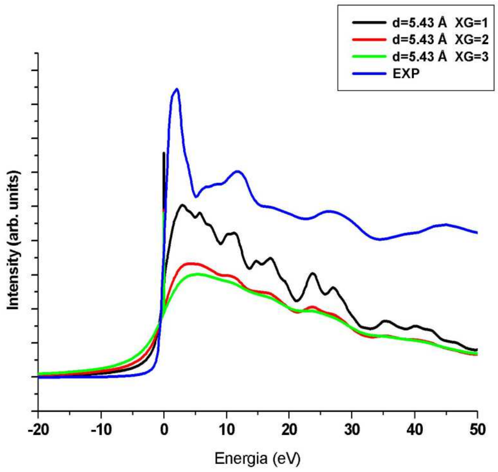

Figure 4.20: Simulated XANES spectra of silicon with diamond single cell (d=5.43 Å) for different value of core-hole linewidth (labeled XG in figure) and comparing with experimental spectra

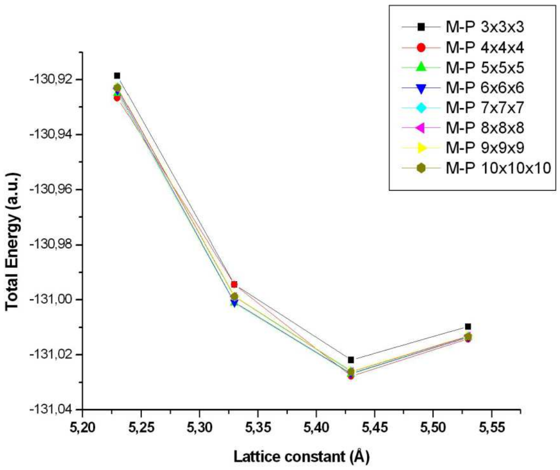

Figure 4.21: Plot total energy in function of lattice constant for 2×2×2 supercell

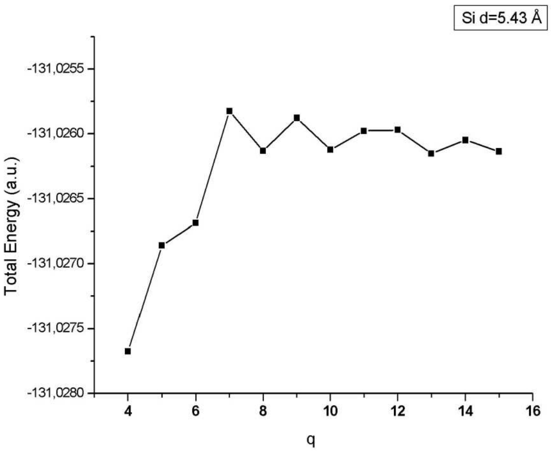

Figure 4.22: Plot total energy in function of dimension of the Monkhorost-Pack grid.

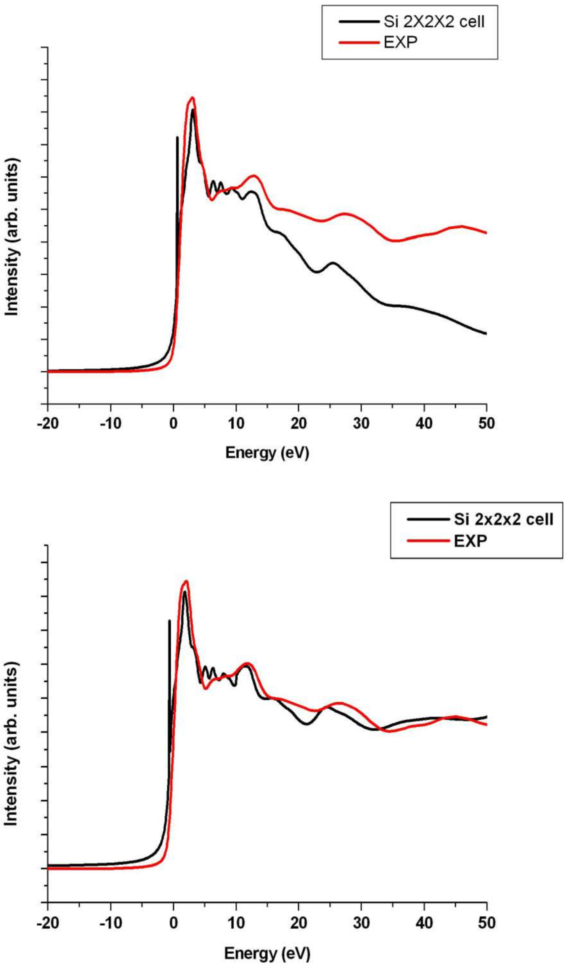

Figure 4.23: Upper figure reports calculated XANES spectra of Si supercell (black line) compared with experimental data (red line). In order to improve the comparison between profiles, the simulated curve has been rescaled by means of linear scale factor in the region above 10 eV (figure in bottom)

well reproduced. The linewidth used in this last calculation is linearly energy dependent after the first 5 eV with slope fixed at 0.075. For the first 5 eV we used costant value of 0.5 eV.

In our opinion the agreement beteween simulated and experimental spectra is not yet completely accetable, in particular for energy values upper 10 eV. Besides, the position of second peak around 15 eV from experimental curve is well-reproduced, but the intensity is probably too much low in simulated curve. In addition, we can see that the black curve suffers a strong decrease, reaching pre-edge intensity values after 50 eV. This beahviour has not been yet investigated but it is probably due to the low number of projectors used to perform the GIPAW reconstruction[24].

Next application regards metalloprotein myoglobin and cytochrome c.

4.4 Metalloproteins: Myoglobin and Cytochrome c

Metalloprotein is a generic term for a protein which contains a metal ion cofactor. A large fraction of all proteins are members of this category:for our applications,we are interested in metallo(Ferri)proteins where the iron atom is bound to the porphiryns group.Porphyrins are an group of aromatic organic compounds consisting in pyrrole units in turn connected together through chemical bonds between their carbon atoms. Iron porphyrins play a vital role in biochemical process such as oxygen transport in animal (hemoglobin, myoglobin) and redox processes such as electron transfer (cytochrome c). Iron and porphiryns group generates the prosthetic group, called heme in hemoglobyne and myoglobin. First application of the methodology, already illustared for iron and silicon crystalline, is on cytochrome c. In this biomolecule, the heme prosthetic group is centered on the Fe ion and connected to the protein matrix through the covalent bonds between the cysteine residues and two vinyl groups of the adjacent pyrrols. The axial coordination of the metal involves the nitrogen atom of hystidyne (Hys18) (labeled Nist) and the sulfur atom of the metionine (Met80) (fig 4.24). In the recent years, many papers regarding different applications of the XANES spectroscopy on the cytochrome c have been published [25][26][27]. In particular

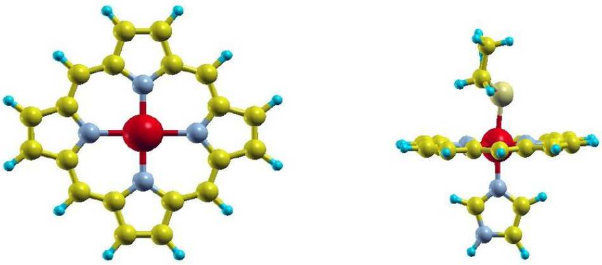

Figure 4.24: In this figure, on the right, the porphyrins group is shown (yellow and grey colours are used for carbon and nitrogen atoms respectively) with iron atom (in red colour) in center of the ring. On the left we reported the cluster used to simulate the XANES spectra for cytochrome c (sulfur atom is in yellowish colour out of the ring and the blue colour are used for hydrogen atoms)

in [25] the authors using x-ray absorption spectroscopy by synchrotron radiation to investigate the pH-dependence of the local structure of Ferricytochrome c. Xanes spectroscopy is used by the authors in [26] to study the structural and dynamical effects of the Cytochrome c in a dry trehalose matrix. In the last paper a more general solvent effect has been object of a methodological study by using XANES and EXAFS spectroscopy.
In our case we did not want to investigate a particular biological or solvent effect of the cytochrome c, but we used this isolated metalloprotein to test a possibile biological application of the GIPAW scheme.
In order to achieve our goal, we isolated the fragment of the citochrome c containing eme group and two aminoacid residues, Hys18 and Met80, in axial position respect the heme ring.Subsequently, we performed the ion optimization using two pseudopotential for iron,USPP and NCPP, already used to simulate the Fe-bcc system. The most important optimized geometrical parameters are reported in the tables below for different accuracy level.
In addition, following the scheme reported in [26] and in figure (4.25), further geometrical outcomes are showed in table (4.5).

From tables (4.4) and (4.5), we noted that the distance Fe-S calculated by using USPP* and NCPP* approach (2.64 Åand 2.76 Å) are too much large than to the other ab inito methods and EXAFS data (2.29 Å). For these reasons we have chosen to generate the XANES spectra using the geometrical structure optimized without core-hole effect. Obviously, the core-hole effect is introduced

k-points	Gamma point
Plane wave cutoff	150 Ry
Box dimension	20×20×18 (bohr)
Gaussian smearing	0.001 Ry

Table 4.4: Parameters used to perform the ions optimization for cytochrome c

Approach	Distance Fe-S	Distance Fe-Nist	Distance Fe-Np
NCPP	2.35	1.97	1.99
NCPP*	2.76	2.28	1.99
USPP	2.29	1.99	2.00
USPP*	2.64	2.28	1.99
XRD PDB	2.31	1.98	2.04
XRD PDB	2.49	2.60	1.81
NMR PDB sol	2.37	1.96	2.07
NMR PDB sol	2.36	1.94	2.08
NMR PDB sol	2.23	1.93	1.95
EXAFS	2.29	2.10	1.99

Table 4.5: Most important geometrical parameters (in Å) for cytochrome c optimized with different accuracy levels.NCPP* and USPP* corresponds to the Norm-Conserving and Ultrasoft approach with core-hole.Fe-S and Fe-Np are the distance between iron and sulfur in Met80 and nitrogen in pyrrolic unit respectively.EXAFS,XRD and NMR data are cited in [26]

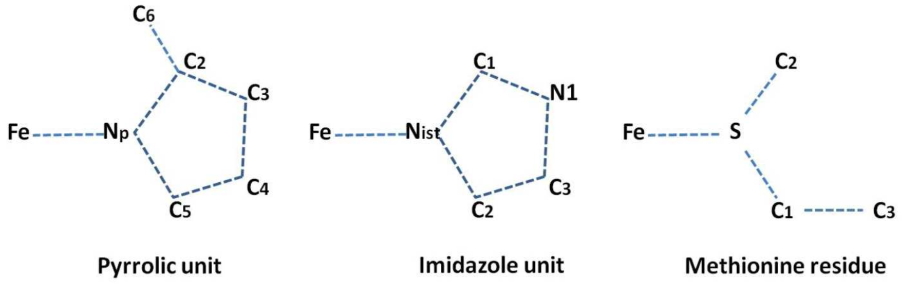

Pyrrolic unit Imidazole unit Methionine residue

Figure 4.25: Structural model for methionine,histidine residue and porphyrin group

Pyrrolic unit	Model	NCPP	USPP	USPP*	EXAFS
Fe-Np	1.99	1.99	2.00	1.99	1.99(2)
Np-C2	1.38	1.39	1.38	1.38	
C2-C3	1.44	1.44	1.44	1.44	
C3-C4	1.34	1.37	1.36	1.36	
C2-C6	1.38	1.39	1.37	1.39	
Fe-Np-C2	109°	127°	127°	127°	
Fe-Np-C3	163°	163°	163°	163°	
Np-C2-C6	125°	124°	125°	125°	
Histidine unit	Model	NCPP	USPP	USPP*	EXAFS
Fe-Nist	2.00	1.97	2.00	2.28	2.10 (5)
Nist-C1	1.32	1.34	1.33	1.32	
Nist-C1	1.37	1.39	1.38	1.38	
C1-N1	1.34	1.37	1.36	1.36	
C2-C3	1.35	1.37	1.37	1.37	
C3-N1	1.35	1.39	1.38	1.38	
Fe-Nist-C1	128°	126°	126°	125°	
Fe-Nist-C2	127°	127°	127°	128°	
Fe-Nist-N1	163°	162°	161°		
Methionine unit	Model	NCPP	USPP	USPP*	EXAFS
Fe-S	2.29	2.35	2.29	2.64	2.29 (4)
S-C1	1.81	1.87	1.81	1.81	
S-C2	1.82	1.85	1.82	1.82	
Fe-S-C1	109°	109°	111°	108°	
S-C1-C3	110°	112°	111°	114°	

Table 4.6: In table several geometrical parameters (distance in Å) for cytochrome c for different accuracy level are showed.The atoms involves in the distances reported in this table, are labeled following the scheme in figure 4.25.

k-points	Gamma point
Electronic integration grid	3×3×3
Thres. conv.	0.01 eV
Max numb. iter.	50.000
c-h linewidth	1.36 eV /0.1 (0.05) slope

Table 4.7: In table 4.7 the most important parameters for *XSpectra* module are reported.The core-hole line width is calculated as 1.36 eV and 0.05 eV in the first 5 eV of the spectrum, and linearly energy dependent above with slope 0.1

in the wavefunction optimization of the final state.
As already done for Fe-bcc and silicon, we could reduce the core-hole interaction between periodic images of the system, building a supercell, minimum 2×2×2. We did not follow this route for excessive computational cost. Increasing number of atoms, it would have been necessary reduce the kinetic energy planewave cutoff, reducing the accuracy of the calculation.
In general the absorption cross section for cristalline system with unit cell belonging to specific class of symmetry, involves strong dependence by specific coordinate space of the polarization vector; its analytical expression will be determinated by own class of symmetry.
In the previous applications, we generated XANES spectra for systems with high symmetry; Fe-bcc e d-silicon belong to point group symmetry O-h and Td respectively. For these class of symmetry, the absorption cross section did not manifest a dependence by polarization vector of the plane wave incident. In practice XANES spectra did not show any angular dependence when the the polarization and the direction of the incident x-ray beam are varied. Both calculated and experimental cross section are determined in crystalline form.
On the contrary the experimental cross sections of the biomolecules studied in this thesis are acquired in solution. In this case,in order to reproduce XANES spectra, more than one calculation are needed, because it does not exist an angular dependence of the cross section, neither the polarization vector suffers a preferred orientation. As reported in section 1.4, the isotropic XANES cross section σ_a^0 is given by the average of the three cross sections evaluated taking as polarization vector the three basic unit vectors (along x,y and z directions).

$$\sigma_a^0 = \frac{\sigma_a(1,0,0) + \sigma_a(0,1,0) + \sigma_a(0,0,1)}{3} \tag{4.6}$$

For these reasons we performed three different *XSpectra* calculations for each $\sigma(\widehat{i},\widehat{j},\widehat{k})$ absorption cross section, then we applied the equation (4.6) to obtain the isotropic absorption cross section. In table 4.7 we reported the parameter used for *XSpectra* calculations. In the following two figures (4.26 and 4.27) Norm-Conserving pseudopotentials calculations of XANES absorption cross section for cytochrome c is reported. The only difference is the broadening γ parameter used. For energy larger than 30 eV, we found an accetable agreement with experimental curve, whereas for energy ranging 0-30 eV the experimental peaks are not well reproduced by calculated data. The highest intensity peak is found around 25 eV in experimental profile, against 20 eV in theoretical curve. Moreover the experimental spectra is characterized by several areas where the function is oscillating. In our opinion this behaviour gets lost in calculated

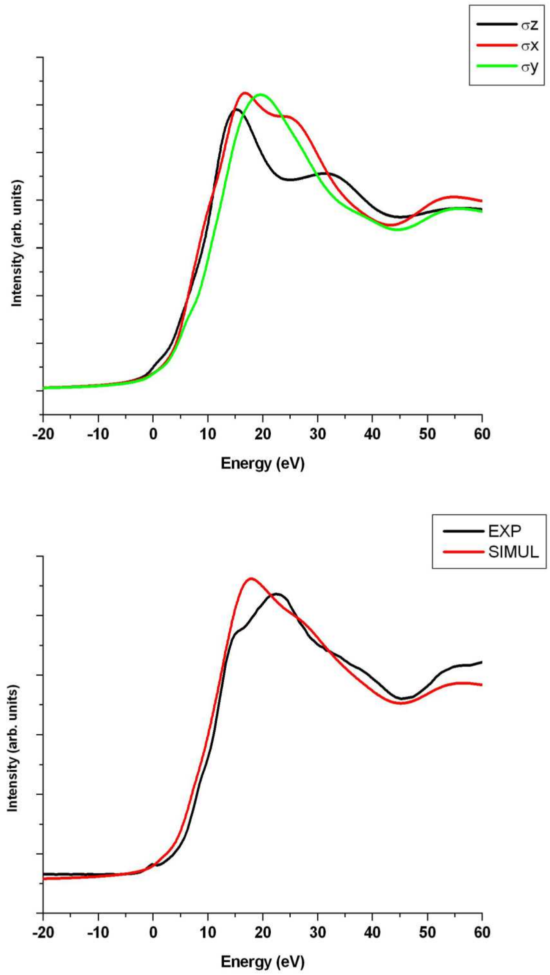

Figure 4.26: Upper figure reports three different XANES cross sections for cytochrome c determinated using Norm-Conserving approach as explained in the text.The cross sections $\sigma_a(0,0,1)$, $\sigma_a(1,0,0)$ and $\sigma_a(0,1,0)$ are labeled in figure as σ_z,σ_x and σ_y respectively. In bottom the isotropic cross section is compared with experimental data. Core-hole linewidth is set costant up to 5 eV (1.36 eV) and variable with slope 0.1 above (table 4.7)

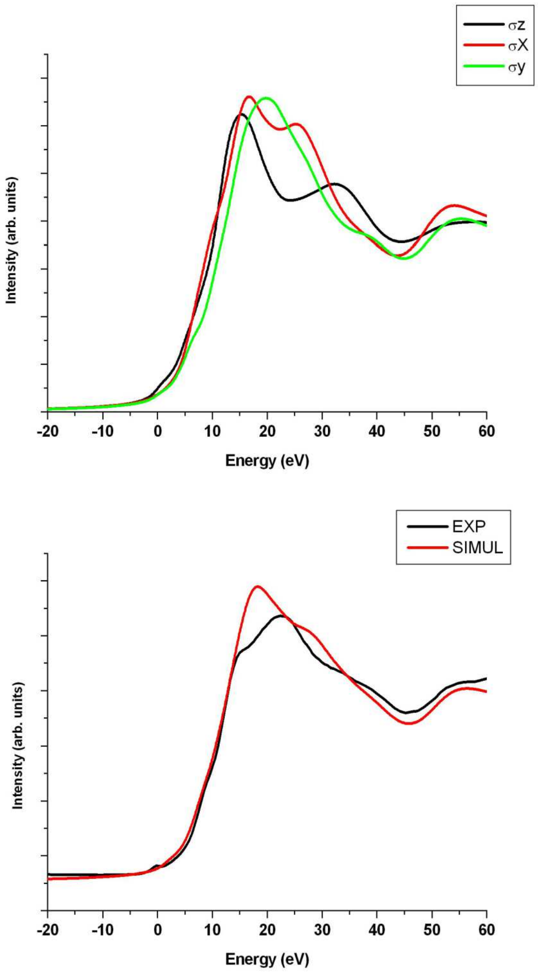

Figure 4.27: Upper figure reports three different XANES cross sections for cytochrome c determinated using Norm-Conserving approach as explain in the text. The cross sections $\sigma_a(0,0,1)$, $\sigma_a(1,0,0)$ and $\sigma_a(0,1,0)$ are labeled in figure as σ_z,σ_x and σ_y respectively. In bottom the isotropic cross section is compared with experimental data. Core-hole linewidth is set costant up to 5 eV (1.36 eV) and variable with slope 0.05 above (table 4.7)

spectra and the computational profile flattens.
In addition, the figure shows three component of the isotropic cross section. The axial component (σ_z) contributes with minor intensity to the total isotropical cross section. This fact is in agreement to [26] and the isotropic spectrum is dominated by paths involving atoms in the heme group;the higher intensity contributions of σ_x and σ_y in figure 4.27 seems to confirm this properties.
In figures (4.28) and (4.29) the same calculations are performed with Ultrasoft approach. We did not detect strong difference respect Norm-Conserving calculation, except for σ_x which shows higher intensity respect to the other contributions. Ultrasoft and Norm-Conserving spectra are compared in figure (4.30) and (4.31).

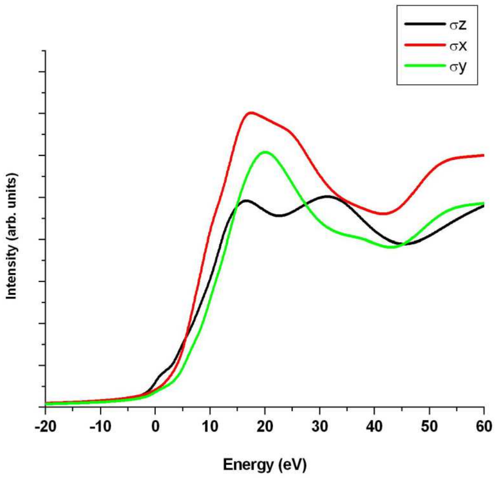

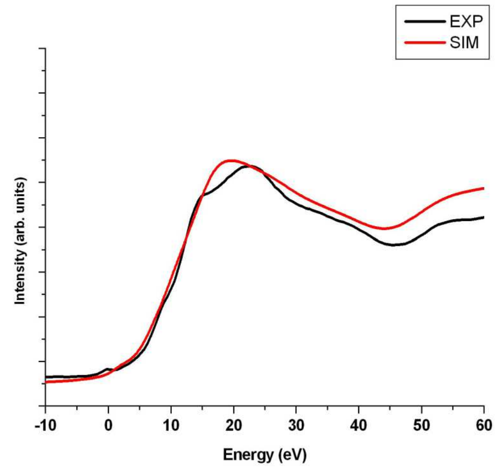

Figure 4.28: Upper figure reports three different XANES cross sections for cytochrome c determinated using Ultrasoft approach as explain in the text.The cross sections $\sigma_a(0,0,1)$, $\sigma_a(1,0,0)$ and $\sigma_a(0,1,0)$ are labeled in figure as σ_z,σ_x and σ_y respectively.In bottom the isotropic cross section is compared with experimental data.Core-hole linewidth is set costant up to 5 eV (1.36 eV) and variable with slope 0.1 above (table 4.7)

Beyond the edge, the XANES spectra generated by Ultrasoft approach remains above the experimental curve, whereas the Norm-Conserving crosses the experimental curve. In both case, the XANES region below 30 eV is not well reproduced.

Further investigations are needed to understand this trend and subsequently try to improve the simulations. Probably it is necessary to act on geometrical optimization, so as to have a more realistical geometry of the cytochrome c structure. Another effect to take in account is the solvent effect, since could determine the XANES experimental profile [26].

Finally, XANES spectra for cytochrome c are calculated using a constant γ parameter (2eV)(fig. 1.32).

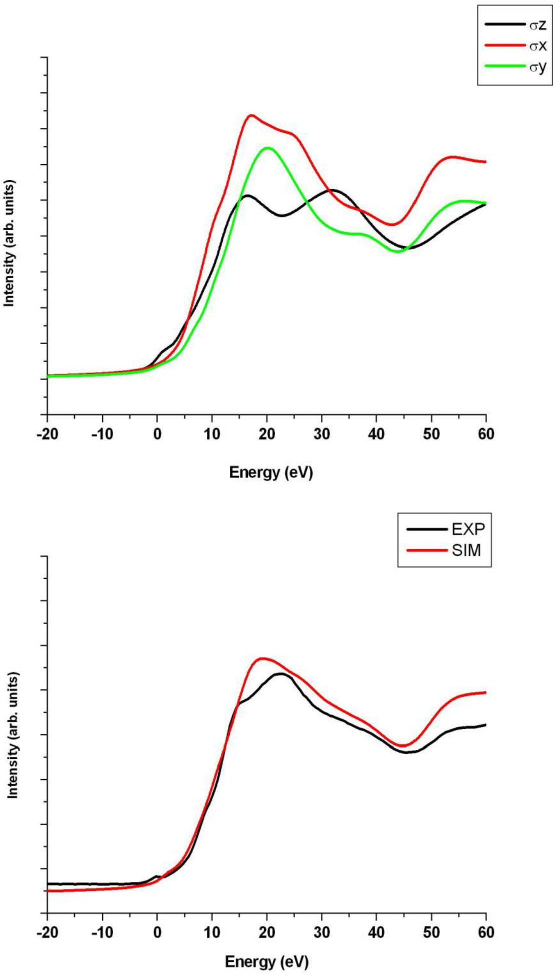

Figure 4.29: Upper figure reports three different XANES cross sections for cytrochrome c determinated using Ultrasoft approach as explained in the text. The cross sections $\sigma_a(0,0,1)$, $\sigma_a(1,0,0)$ and $\sigma_a(0,1,0)$ are labeled in figure as σ_z,σ_x and σ_y respectively. In bottom the isotropic cross section is compared with experimental data. Core-hole linewidth is set costant up to 5 eV (1.36 eV) and variable with slope 0.05 above (table 4.7)

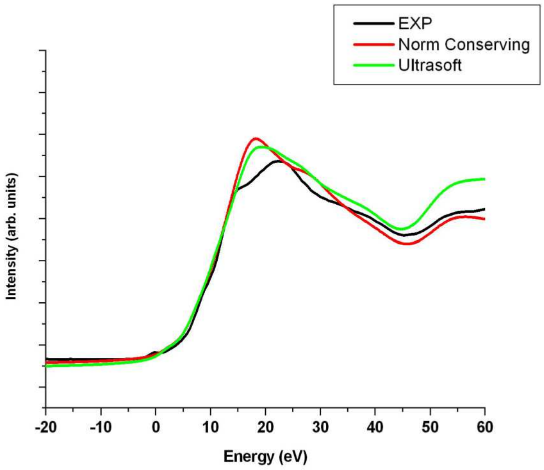

Figure 4.30: In figure the isotropic cross sections for cytochrome c obtained by USPP and NCPP are compared with experimental data.Core-hole linewidth is set costant up to 5 eV (1.36 eV) and variable with slope 0.1 above (table 4.7)

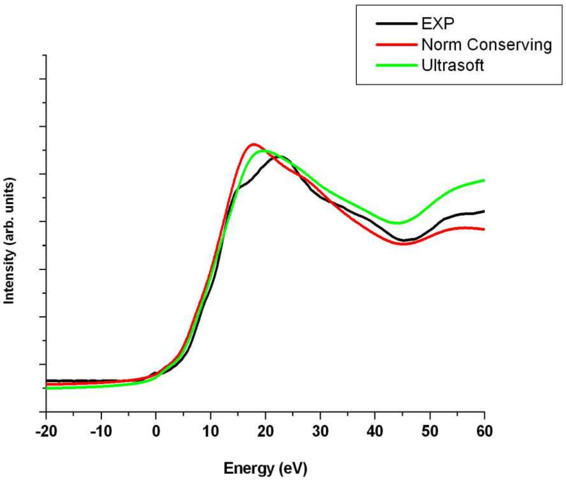

Figure 4.31: In figure the isotropic cross sections for cytochrome c obtained by USPP and NCPP are compared with experimental data. Core-hole linewidth is set costant up to 5 eV (1.36 eV) and variable with slope 0.05 above (table 4.7)

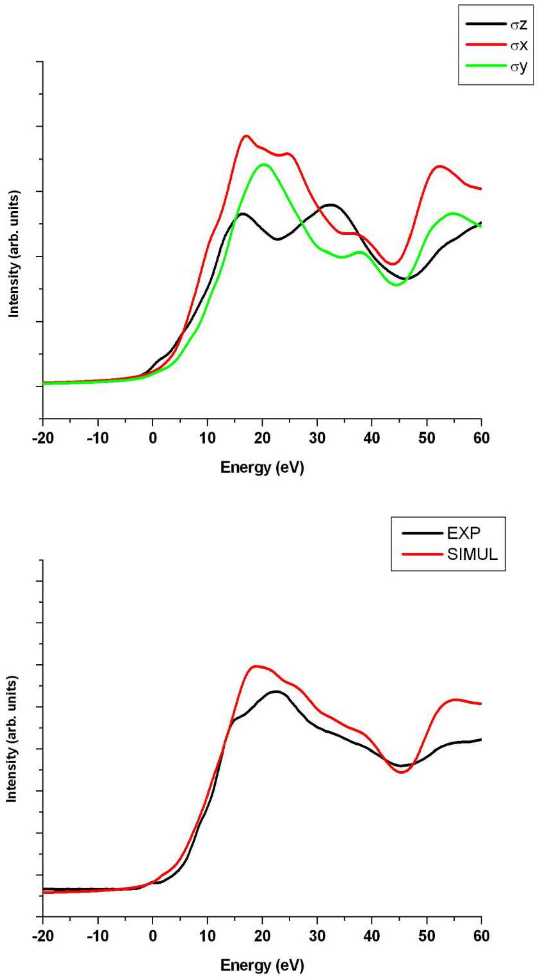

Figure 4.32: Upper figure reports three different XANES cross sections for cytochrome c determinated using Ultrasoft approach as explained in the text. The cross sections $\sigma_a(0,0,1)$, $\sigma_a(1,0,0)$ and $\sigma_a(0,1,0)$ are labeled in figure as σ_z,σ_x and σ_y respectively. In bottom the isotropic cross section is compared with experimental data. Core-hole linewidth is set costant at 2 eV

Next application is on Myoglobin, where we propose an anologue scheme of calculation for XANES spectra, already showed for cytochrome c. In particular, we consider the structure of carbonmonoxy-Myoglibin (MbCO) where the CO group is bound with Fe in heme group (Fig 4.33). In axial poistion we found the carbonmonoxy group from one side and the aminoacid residue Hys64 on the other side. In whole protein, the experimental geometrical position of the CO group is determinated by His64 and Val68, which are not considerer in this study. The reference [AIP] contains a valid approach scheme to simulate XANES spectra of the MbCO system. As reported in [27], the XANES spectra is strongly dependent by CO position. The complete ions optimization of the cluster in figure 4.33 leads the direction of the chemical bond C-O to be perpendicular respect to the heme plane ($\alpha = 0°$). Moreover, we indicate the angle β as the angle between the Fe-CO and the C-O directions. From XRD diffraction, the α and β angle are detected at 4.8° and 7.4°. To generate XANES spectra, we considered to use the cluster geometry more similar to the experimental one. Then we set the angle α at 9.0° leaving the β angle fixed at 0°. As reported in [28], the dipolar transition depends weakly by angle β and just in the pre-edge region. In table 4.8 optimized geometrical parameters are reported. The geometrical parameters in MbCO do not suffer a geometrical distorsion due to the core-hole effect, then we can introduce it completely, optimzing geometrical structure of the cluster in figure (4.33) by using USPP* and NCPP* pseudopotential. The most important parameters introduced in the Quantum Espresso *PWscf* and *XSpectra* modules are showed in tables (4.9) and (4.10). In figure 4.34 the XANES spectra are reported for different cross section contribution (upper figure) and final isotropic value, calculating by using the equation (4.6).

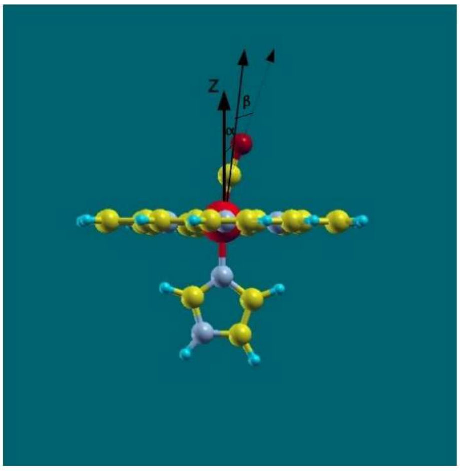

Figure 4.33: Cluster used to simulate the atomic region of the MbCO near heme group. The direction of the CO group make the angle β with Fe-CO direction.

As usual, we quoted the spectra showing three components of absorption cross section, and subsequently the isotropic cross section. Regarding the main experimental peak (around 20 eV), his position is reproduced with good accuracy,but it is characterized by too much pronounced broadening. The simulated curve seems to have a similar trend respect experimental profile. On the contrary by aligning the main theoretical peaks with experimental one, the experimental

Approach	Distance Fe-CO	Distance Fe-Nist	Distance Fe-Np
NCPP	1.72	2.09	2.01
NCPP*	1.72	2.02	2.00
USPP*	1.77	2.10	2.04
XRD PDB	1.73	2.12	2.00
RELAX (CP dynamics)	1.77	2.15	2.04
XRD	1.73	2.06	1.98
XRD	1.82	2.06	1.98
EXAFS	1.93	2.20	2.01
XANES	1.83(2)	2.06(3)	2.00(2)

Table 4.8: In this table the most important parameters (in Å) for MbCO for different accuracy level are indicated. NCPP* and USPP* corresponds to the Norm-Conserving and Ultrasoft approach with core-hole. Fe-CO and Fe-Np are the distances between iron and CO group and nitrogen in pirrolic unit respectively. The relaxed data are from Car-Parrinello (CP) molecular dynamics [28]. EXAFS,XANES and XRD geometrical parameters are showed in [29]

k-points	Gamma point
Plane wave cutoff	100 Ry
Box dimension	20×20×15 (bohr)
number of atoms	48
Gaussian smearing	0.001 Ry

Table 4.9: Parameters used to perform the ions optimization for MbCO

k-points	Gamma point
Electronic integration grid	4×4×4
Thres. conv.	0.01 eV
Max numb. iter.	50.000
c-h linewidth	1.36 eV /0.1 (0.05) slope

Table 4.10: In this table the most important parameters for *XSpectra* module are reported.The core-hole line width is calculated as 1.36 eV and 0.05 eV in the first 5 eV of the spectrum, and linearly energy dependent above with slope 0.1

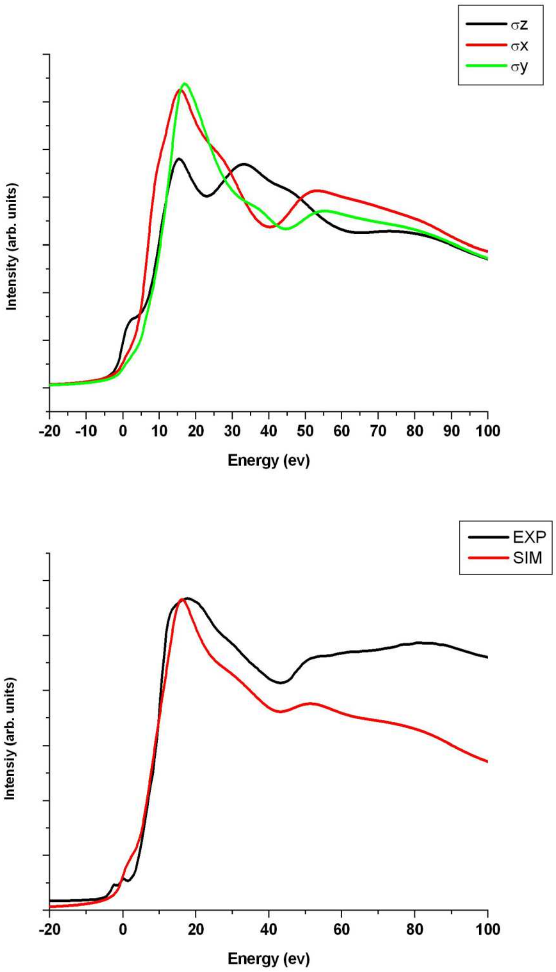

Figure 4.34: Upper figure reports three different XANES cross sections for carbonmonoxy-myoglobin determinated using Norm-Conserving approach. The cross sections $\sigma_a(0,0,1)$, $\sigma_a(1,0,0)$ and $\sigma_a(0,1,0)$ are labeled in figure as σ_z,σ_x and σ_y respectively. In bottom the isotropic cross section is compared with experimental data. Core-hole linewidth is variable with slope 0.1 above 5 eV and costant up to 5 eV (1.36 eV)

curve is not well reproduced in terms of intensity and it is found always below the theoretical one.

Regarding the MbCO system, the contribution axial to the isotropic cross section seems to be reduced with respect to the signal from heme group as well found for cytochrome c.

Moreover the simulated curve above 20 eV reproduces the trend of the experimental curve up to 50 eV, generally with lower intensity. In the pre-edge region a single large peak has been found but reasonably it can not be ascribed to the typical pre-edge signal detectable in the experimental XANES curve. Furthermore in figure (4.34) the XANES spectra from single cross section have a good agreement with spectra reported in [28]. In this paper theoretical and experimental spectra for two different polarizations of the X-rays are showed. By comparing our spectra in (4.34), we note that the contribution from heme group ($\sigma_a(1,0,0)$ and $\sigma_a(0,1,0)$) is characterized by large peak around 20 eV also for the spectra $\sigma_{//}$ in [28] (figure 2). Similarly the spectra in figure (4.34) calculated with polarization normal to the heme plane (black line) suffers more oscillations and at least two important peaks are detected around 15-18 eV and 35-38 eV as in [28]. Differently to the reference [28], where the intensity of the peak at 15 eV is higher respect to the peak at 35 eV, we obtained the same values of intensity for these two peaks.

Finally the biological applications of the GIPAW methods to generate the XANES cross section shows actrattive prospects and potential applications regarding more complex biophysical effects could be considered. However, it would be useful performing more investigations on this biomolecular model, cytochrome c and myoglobin to reduce the differences between calculated and experimental spectra; in particular in terms of intensity on entire spectrum and in the pre-edge region, where no peaks have been reproduced.

Conclusion

The multiscattering approach used in the muffin tin approximation is the most common scheme for analyzing of the XANES spectra, widely applied by many authors. In this framework the spectral simulation is based on a hypotetical reference structure and the accordance with experimental results is achieved through the best fitting of the free parameters. It is well known that in the XANES experiment, the X-ray photon is absorbed by sample and the photolelectron is expelled for photoelectric effect. The photoelectron is scattered by atoms nearest to the absorbing atom, producing the traditional oscillations of the XANES profile; the X-ray beam transmitted through the sample is recorded in function of the photon energy, generally up to 40-50 eV above the absorbtion edge.
In this thesis, we perfomed several simulations of the XANES spectra for some reference systems like iron, silicon, myoglobin and cytochrome c, by using an alternative approach with respect to the multiscattering scheme, where a full ab-initio XANES spectra is generated. Shortly this methodology consists in two step calculations. First a complete full ab-initio optimization of the wavefunction (eventually also for geometrical structure) for the system of interest is carried out; subsequently, the effective calculation of the absorption cross section to obtain XANES spectra is performed, in our case through a Lanczos numerical procedure. More specifically, the wavefunctions which describe the intial and final states of the system involved in the photoelectric process, appear in the expression of the absorption cross section; the wavefunction of the initial state is the orbital occupied by electron before the interaction with X-ray photon (in our case the 1s orbital belonging to the k-shell of the absorbing atom), while the final state is described by all-electron wavefunction in presence of core-hole. This last term is calculated from a plane wave pseudopotential approach in density functional theory scheme. The pseudo wavefunction is transformed in an all electron wavefunction by means of transform operator which is derived in the projector augmented wave (PAW) scheme. By introducing the wavefunctions previously determinated, the cross section is obtained applying a Lanczos numerical procedure.
In addition it is useful to remember that the plane wave pseudopotential approach is among most popular methods to resolve the Kohn-Sham equations. The modern pseudopotential are build on the isolated atom; before to use for the system of interest, it is necessary to check its transferibility. In particular some structural, or eventually, electronic parameters should be reproduced with good accuracy.
In our case, the calculated XANES spectra for K-edge of the bcc-iron is found in good agreement with experimental data, in particular for 2×2×2 bcc-Fe cell. The position of the peaks is well reproduced and substantially also their

intensity. Different results have been obtained for silicon, where the intensity of the simulation curve drops after 10 eV, probabily due to the poor quality of the pseudopotential. In this case the low quality of the pseudopotential is probably due to the number of parameters (projector functions) used to transform the pseudo wavefunction in all electron wavefunction. An open interesting question that we are still investigating in test systems is how the tail at high energies modifies by the inclusion of a larger number of projectors.

Our calculations on iron and silicon XANES cross section regards cristalline structures with unit cell belonging to puntual group with high simmetry (O_h and T_d for iron and silicon respectively). Some examples of simulated XANES spectra on quartz and diamond are available in literature, in any case for cristalline structures. In the second part of this thesis, starting from general expression of the absorbing cross section for C_1 puntual group, it has been derived an expression of the cross section specific for sample in powder or in solution. In fact the simulation of the spectra for myoglobin and cytochrome c required the expression derived for powder samples. For myoglobin essentially we obtained an acceptable agreement to the experimental data, while for cytochrome c further analysis and tests are needed to improve the accordance between experimental and theoretical data.

The topic of this thesis has been awarded of 500000 core processor hours on the CINECA HCP resources, on the basis of a peer-review procedure. In our case these core processor hours was allocated on an IBM BG/Q named FERMI (Project IsC09/AbIXS).

Finally the PAW-DFT (or GIPAW-DFT) approach to calculate a full ab-initio XANES spectra for cristalline or amorphous materials could play a crucial role as alternative method for analyzing the experimental XANES spectra. By using a full ab-initio approach, further powerfull tools ara available (as DOS,PDOS and Bands calculations) to characterize the material. Then further informations on the structure of the material could be available in order to generate and interpret the XANES spectra.

Bibliography

[1] F. Boscherini, Dispense di Fisica della Materia e della Radiazione-Università degli studi di Bologna 2009

[2] J.A. Nielsen, Elements of Modern X-Ray Physics Wiley

[3] A. Messiah, Quantum Mechanics Dover Publication New York

[4] Giorgio Margaritondo, Characteristics and Properties of Synchrotron Radiation- X Scuola Nazionale di Luce diSincrotrone Luino 2009

[5] A. Mihelic Notes on XANES spectroscopy

[6] J. Zabloudil et al.,Electron scattering in solid matter, Springer (2005)

[7] C. Brouder, J. Phys.:Condens. Matter 2, 701 (1990)

[8] S. I. Zabinsky et al., Physical Review B 52, 2995 (1995)

[9] I.N. Levine, Quantum Chemistry, Prentice Hall 2000

[10] J.C. Slater, Phys. Rev. 51, 846 (1937)

[11] P.E. Blochl, Phys. Rev. B 50, 17953 (1994)

[12] D. Vanderbilt, Phys. Rev. B 41, 7892 (1990)

[13] G. Kresse, D. Joubert, Phys. Rev. B 59, 1758 (1999)

[14] C. Gougoussis, M. Calandra, A.P. Seitsonen, and F. Mauri, Phys Rev B 80, 075102 (2009)

[15] M. Taillefumier,D. Cabaret,A.M. Flank and F. Mauri, Phys. Rev. B 66, 195107 (2002)

[16] N.W. Aschcroft,D. Mermin - Solid State Physics, Holt Rinehart and Wintson (1976)

[17] B. Meyer, The pseudopotential Plane Wave approach, Computational Nanosciences:Do it Yourself, NIC series

[18] N. Troullier, J.L. Martins, Solid State Comm. 74, 613 (1990)

[19] L. Kleinman, D.M. Bylander, Phys. Rev. Lett. 48, 1425 (1982)

[20] C. J. Pickard, F. Mauri Phys. Rev B 63, 245101 (2001)

[21] W. Zhong, G. Overney, and D. Tomanek Phys. Rev. B 47, 95 (1993)

[22] M. Cazzaniga,L. Caramella,N. Manini and G. Onida, Phys. Rev. B 82, 035104 (2010)

[23] Quantum-ESPRESSO is a community project for high-qualityquantum-simulation software, based on density-functional theory, andcoordinated by Paolo Giannozzi. See http://www.quantum-espresso.organd http://www.pwscf.org.

[24] M. Calandra, Private comunication

[25] F.Boffi,A. Bonincontro,S. Cinelli,A. Congiu Castellano,A. De Francesco,S. Della Longa, M. Girasole Biophys.Journal 80, 1473 (2001)

[26] L. Giachini, F. Francia, L. Cordone, F. Boscherini and G. Venturoli, Biophys. Journal 92, 1350 (2007)

[27] G. Veronesi, C. Degli Esposti, L. Ferrari, G. Venturoli, F. Boscherini,F.D. Vila, and J.J. Rehr Phys. Rev. B 82, 1 (2010)

[28] M. Arfaoui, D. Cabaret, S. Della Longa, A. Seitsonen, and F. Mauri AIP conference proceedings 882,331 (2007) doi:10.1063/1.2644516

[29] S. Della Longa, A. Arcovito, M. Girasole, J.L. Hazemann and M. Benfatto Phys Rev. Lett. 87, 155501-1 (2001)